Isotopic Insights into the Origin of Dissolved Sulfate and the Sulfate-supported Microbial Processes in Deep Subsurface Fracture Waters in the Witwatersrand Basin, South Africa

by

Siwen Wei

A thesis submitted in partial fulfillment of the requirements for the degree of

Master of Science

Department of Earth and Atmospheric Sciences

University of Alberta

Abstract

Subsurface groundwater has been discovered from rock fractures in Precambrian cratons worldwide. In the Witwatersrand Basin (South Africa), the fracture waters show residence times in the order of 1 to 100 million years. Interestingly, sulfate-reducing bacteria are widespread in these fracture waters. In particular, a unique, single-species microbial ecosystem coupling sulfate reduction and H_2 oxidation has been discovered in one of the oldest fracture waters. While H_2 can be produced by water radiolysis induced by radioactive decay of U, Th and K in the host rocks, the origin of dissolved sulfate, the other essential energy source supporting the sulfate reducers, is poorly constrained. Here, we employ multiple sulfur isotopes ($^{32, 33, 34, 36}S$) and oxygen isotopes ($^{16, 18}O$) to assess potential sulfate sources as well as secondary processes that could affect the sulfur and oxygen isotope compositions of dissolved sulfate in the fracture waters.

Twenty fracture water samples were collected from the Kloof, Tau Tona, Driefontein, Beatrix, Joel and Masimong gold mines intersecting three major sedimentary sequences, i.e., the Transvaal, Ventersdorp and Witwatersrand Supergroups, in the Witwatersrand Basin. Dissolved sulfate shows isotopic ranges from -5.3‰ to 19.4‰ for $\delta^{34}S$, -0.17‰ to 0.50‰ for $\Delta^{33}S$, and -1.1‰ to 10.9‰ for $\delta^{18}O$. The non-zero $\Delta^{33}S$ values clearly indicate a sulfur source older than 2.0 Ga. Because sulfate minerals are lacking in the study area, and carbonate associated sulfate in the Transvaal dolomite overlying some of the water-bearing layers displays distinct $\delta^{34}S$ (31.4-39.2‰) and $\Delta^{33}S$ values (-0.01 to 0.16‰), dissolved sulfate could not have originated from dissolution of sulfate minerals in the host rocks. Instead, sulfide minerals in the Archean host rocks are more likely the source of dissolved sulfate.

Two possible mechanisms can transform sulfide to sulfate: oxidative weathering of sulfide, which usually occurs in aerobic conditions, and/or radiolytic oxidation of sulfide, which can occur in both aerobic and anaerobic conditions. Comparison of the $\delta^{18}O$ values between dissolved sulfate and their hosting fracture waters indicates that dissolved sulfate in relatively shallow samples (e.g., <1.9 km) fall into the expected $\delta^{18}O$ range of the initial sulfate product derived from oxidative sulfide weathering but have not reached oxygen isotope equilibrium with hosting water. Because the periods required for oxygen isotope exchange to reach equilibrium are modeled to be less than 342,400 years, orders of magnitude shorter than the estimated residence times, the oxygen isotope disequilibrium implies that the sulfate production is fairly recent and probably still ongoing while the fracture waters have been isolated from the surface for millions of years. In contrast, the dissolved sulfate and their hosting waters from deep boreholes (>3 km) show apparent oxygen isotope equilibrium. This might be attributed to (1) accelerated oxygen isotope exchange rates at relatively high temperatures, (2) less efficient sulfate production mechanism (e.g., radiolytic oxidation), (3) larger extent of sulfate reduction, and/or (4) oxygen isotope shift by fluid-rock interaction. Overall, our results suggest that sulfate can be produced by *in-situ* oxidation of sulfide in the host rocks through oxidative sulfide weathering or radiolytic sulfide oxidation during water-rock interaction. Therefore, geological processes can provide a stable long-term sulfate source to sustain the terrestrial subsurface microbial systems isolated for geological time scales.

In all sites except Beatrix, the large offset in $\delta^{34}S$ values (up to 26.4‰) and compatible $\Delta^{33}S$ values between dissolved sulfate and sulfide are consistent with the existence of sulfate-reducing bacteria in these waters. In Beatrix, however, sulfur isotopic signatures are more complicated. A series of samples collected from one borehole (depth of 1.3 km) in Beatrix between 2011 and 2013 show that dissolved sulfate and sulfide initially (in 2011) have very distinct $\Delta^{33}S$

values, suggesting different sources for dissolved sulfate and sulfide. The $\Delta^{33}S$ discrepancy between sulfate and sulfide diminished from 2011 to 2012 associated with an increase in $\delta^{34}S$ value of sulfide and a decrease in $\delta^{34}S$ value of sulfate, indicating bacterial sulfide oxidation was dominant over this time. In 2013, the $\delta^{34}S$ and $\Delta^{33}S$ signatures of sulfate and sulfide appear to be controlled by bacterial sulfate reduction. This 3-year sampling revealed a surprisingly quick ecological shift from one dominated by sulfide-oxidizing bacteria to one dominated by sulfate-reducing bacteria in the subsurface fracture waters, which has never been observed before.

Preface

This thesis is a collaborating project with several international teams, including Dr. Tullis C. Onstott's team at Princeton University, Dr. Barbara Sherwood Lollar's team at the University of Toronto, and Dr. Esta van Heerden's team at the University of the Free State, Bloemfontein, South Africa), Dr. Boswell Wing's team at McGill University, and Dr. Shuhei Ono's team at Massachusetts Institute of Technology. The water samples in this study were collected by Dr. Long Li and a large number of colleagues from the collaborative teams. The aqueous chemistry (anions and cations) and stable isotope compositions ($\delta^{18}O$ and $\delta^{2}H$) of the water samples cited in the thesis were analyzed by the Princeton and the Toronto teams, respectively. I was responsible for the chemical extraction of sulfide and sulfate in the fracture water samples, SEM examination of the extracted sulfate (precipitated as $BaSO_4$), XRD/EPMA examination and chemical extraction of carbonate associated sulfate from the Transvaal dolomite samples (all at the University of Alberta), multiple sulfur isotope measurements of the sulfide and sulfate in Ono's laboratory at MIT, and data analysis and modeling presented in this thesis.

Acknowledgement

Foremost, I would like to express my sincere gratitude to my supervisor Dr. Long Li for the continuous support of my MSc study and research, for his patience, motivation, enthusiasm, and immense knowledge. His guidance helped me in all the time of research and writing of this thesis.

I would like to thank Dr. Shuhei Ono, Dr. Genming Luo in the Stable Isotope Geobiology Laboratory at Massachusetts Institute of Technology and Dr. Boswell Wing, Dr. Thi Hao Bui at McGill University for their instruction in multiple sulfur isotope measurement. I also thank Dr. Andrew Locock in the Electron Microprobe Laboratory, Dr. Gerein Nathan in the Scanning Electron Microscope Laboratory and technician Diane Caird in the X-ray Diffraction Laboratory at University of Alberta for providing analytical results used in my thesis.

Moreover, I would like to thank my other two examining committee members Dr. Tom Chacko, Dr. Daniel Alessi for their constructive reviews, which greatly improved quality of my thesis.

My thanks also go to Dr. Kurt Konhauser, Dr. Karlis Muehlenbachs, Dr. Daniel Alessi, Dr. Gram Pearson and Dr. Jingao Liu for their inspiring instruction in the courses I have taken. I also would like to thank my colleagues Morgan Snyder, Jianghanyang Li and Zhe Zhang at University of Alberta for providing their help in my research.

Finally, I would like to thank my family for giving me their strongest support throughout the past two years.

This research is funded by the Alfred P. Sloan Foundation Deep Carbon Observatory and NSERC Discovery grant to Dr. Long Li.

Table of Content

List of Figures

List of Tables

1. Introduction

The Witwatersrand Basin in South Africa contains abundant gold and uranium reefs formed in a period between 3074 and 2714 Ma (*Robb and Meyer, 1995*). Mining operations in the Witwatersrand Basin have encountered abundant water reservoirs at various drilling levels as deep as >3.5 kilometers below the surface (kmbs) (*Duane et al., 1997; Takai et al., 2001; Lippmann et al., 2003; Moser et al., 2005; Lin et al., 2006; Onstott et al., 2006*). Noble gas and ^{36}Cl measurements on the fracture waters from 0.7 to 3.3 kmbs in the Carletonville (e.g., Beatrix, Kloof, Driefontein and Mponeng) and the Evander Goldfield, Lippmann et al. (*2003*) revealed old residence times of those fracture waters from 1 to 168 million years. Investigations of water geochemistry indicate that the shallow (roughly <1.9 kmbs) fracture waters mostly show relatively low temperature and low salinity, and contain dissolved gases dominated by CH_4 and N_2 with generally small but variable amounts of higher hydrocarbons and O_2. The fracture waters from greater depth (>1.9 kmbs, particularly those >3 kmbs) have much higher temperature (up to >60 ºC) and salinity, and contain dissolved gases dominated by CH_4, N_2 and H_2 with small but variable amounts of higher hydrocarbons, noble gases, but very little O_2 (*Silver et al., 2012; Lippmann et al., 2003; Ward et al., 2004; Lin et al., 2005a; Sherwood Lollar et al., 2006*).

Most interestingly, a variety of microbial ecosystems have been discovered in these fracture waters that have apparently experienced long-term hydrological isolation from surface water (*Takai et al., 2001; Ward et al., 2004; Kieft et al., 2005; Moser et al., 2005; Lin et al., 2006*). The microbial biomass abundance and diversity also vary significantly in fracture waters at different locations and depths. In shallow fracture waters, more abundant and diverse microbial populations have been found, such as methanogens, sulfate reducers, and various other bacteria (*Takai et al., 2001; Moser et al., 2005; Gihring et al., 2006*). At greater depths, with limited energy

from photosynthesis available for the microbes, the fracture waters host very low biomass abundance and low biodiversity (*Kieft et al., 2005; Lin et al., 2006; Pfiffner et al., 2006; Chivian et al., 2008*). For example, molecular and genomic studies reveal a unique chemoautotrophic ecosystem consisting of single-species sulfate-reducing bacteria, *Desulforudis audaxviator*, in a high-temperature (~60 ºC), alkaline (pH=9.3), anaerobic fracture water reservoir at 2.8 kmbs in the Mponeng mine in the Witwatersrand Basin (*Lin et al., 2006; Chivian et al., 2008*). This ecological difference may be related to the geochemistry of the fracture waters such that the shallow fresh waters contain more nutrients and energy sources whereas the deep saline waters contain much less nutrients and energy sources to support the ecosystem (*Onstott et al., 2006*). Despite the large variations in microbial biomass and biodiversity, the DNA investigations have unambiguously shown that the sulfate-reducing bacteria are widespread in subsurface fracture waters and even become the dominant species in the deeper, more isolated saline fracture waters in the Witwatersrand Basin (*Baker et al., 2003; Kieft et al., 2005; Moser et al., 2005; Line tal., 2006; Chivian et al., 2008*).

This ecological difference also explains the geochemical features of dissolved gases. For example, compound-specific carbon and hydrogen isotopic analyses of hydrocarbons (*Ward et al., 2004; Sherwood Lollar et al., 2006; Sherwood Lollar et al., 2007*) suggest that CH_4 and other alkanes in shallow fracture waters is mainly of biogenic origin (e.g, microbial reduction of dissolved CO_2 to form CH_4), whereas a significant amount of CH_4 in deep saline fracture waters is from abiotic reduction of dissolved CO_2 by H_2. H_2 is often present at relatively high levels in the fracture waters in Precambrian Canada Shield due to fluid-rock interaction between water and mafic minerals (*Sherwood Lollar et al., 2014*), which is also commonly seen in modern seafloor hydrothermal vents. Similar high H_2 levels in the Witwatersrand Basin fracture waters are

surprising because the fracture waters in the Witwatersrand Basin are mostly located in felsic rock units (see the geological background below). Based on laboratory experiments (*Lin et al., 2005a*) and field data (*Lin et al., 2005b*), Lin and co-authors proposed a mechanism of radiolysis of water (see Fig. 1) to explain the abundant H_2 observed in the fracture waters in the Witwatersrand Basin. The radiolysis of water can be caused by the energy released from the decay of radioactive elements, such as $^{235,238}U$, ^{232}Th and ^{40}K, which are generally in high abundance in felsic rocks. However, the origin of the other essential energy source, sulfate, which is the major electron acceptor for the metabolism of the terrestrial deep subsurface microbial systems dominated by sulfate-reducing bacteria, is still poorly understood.

There are several possible processes that could supply sulfate to the subsurface fracture waters: (1) sulfate was formed on Earth's surface and then delivered to the subsurface fractures by regional surface water recharge before the fracture system was isolated; (2) sulfate was leached from existing sulfate minerals or carbonate associated sulfate (CAS) in the overlying sedimentary layers along the water migration paths to the fractures; (3) sulfate was produced inside the fracture system by oxidation of sulfide minerals in the host rocks. In the third case, oxidation is likely mainly driven by geological (i.e., abiotic) processes because sulfide-oxidizing bacteria are generally not the dominant species in the subsurface fracture waters, particularly in the anaerobic waters (*e.g., Lin et al., 2006*), although microbial sulfide oxidation cannot be completely ruled out. Abiotic oxidation of the sulfide minerals in the host rocks may occur inside the fracture system by dissolved O_2 in the water, which is equivalent to an *in-situ* oxidative sulfide weathering process. But this scenario cannot be applied to the deep, anaerobic fracture waters due to the lack of free O_2 in these fracture systems. In a recent study on the billion-year-old fracture waters from 2.4 kmbs at the Kidd Creek mine in the Precambrian Canadian Shield, Li et al. (*2016*) proposed a

mechanism of indirect radiolytic oxidation of sulfide (IROS) to account for the dissolved sulfate in these deep, saline, anaerobic fracture waters. The IROS is also driven by the radioactive decay of $^{235,238}U$, ^{232}Th and ^{40}K in the host rocks. The radiogenic energy can induce radiolysis of H_2O, which produces primary reactive species namely hydrogen (H•) atom, hydroxide (OH•) radical (in which • denotes the single and unpaired electron), aqueous electron (e_{aq}-), hydronium (H_3O^+) and hydroxide ion (OH^-), hydrogen peroxide (H_2O_2) and hydrogen gas (H_2) (*Garrett et al. 2005*). The highly active radiolytic species (e.g., OH• and H_2O_2) may further react with sulfide minerals at the water-rock interface to produce dissolved sulfate (*Lin et al., 2005a; Li et al., 2016*). The radiolytic oxidation process is described in Fig.1. As the Witwatersrand Basin has similar fracture water environments to the Precambrian Canadian Shield and hosts uranium reefs, radionuclide decay-induced IROS could be one of the candidates for the origin of fracture water sulfate.

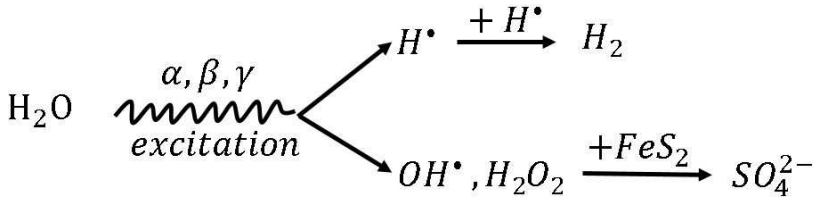

Figure 1. Sketch shows simplified processes of indirect radiolytic oxidation of pyrite (modified after Garrett et al. 2005).

Sulfur and oxygen isotope compositions have been demonstrated to be robust tools to distinguish different sulfate origins (*e.g., van Everdingen and Krouse, 1985; Toran and Harris, 1989; Lefticariu et al., 2010; Li et al., 2016*). This is mainly attributed to different isotope fractionations associated with various reactions in the sulfur cycle. For example, in the oxidative sulfide weathering process, the isotope fractionation between sulfide source and sulfate product is small (less than 5‰) (*Taylor et al., 1984; Seal, 2006*), so the $\delta^{34}S$ value (defined as

$[(^{34}S/^{32}S)_{sample}/(^{34}S/^{32}S)_{standard}-1]\times1000‰$, in which the standard is the Vienna-Canyon Diablo Troilite or VCDT) of sulfate would be not shifted much from the $\delta^{34}S$ value of sulfide. On the other hand, the $\delta^{18}O$ value (defined as $[(^{18}O/^{16}O)_{sample}/(^{18}O/^{16}O)_{standard}-1]\times1000‰$, in which the standard is the Vienna Standard Mean Ocean Water or VSMOW) of sulfate is strongly dependent on the $\delta^{18}O$ values of H_2O and O_2, and the relative proportion between H_2O and O_2 incorporated into the sulfate product (*Llyod, 1967*). In the indirect radiolytic oxidation of pyrite (IROP) reactions, Lefticariu et al. (*2010*) used laboratory experiments to yield ^{34}S enrichment by 1.5‰ to 3.4‰ and ^{18}O enrichment by 1.5‰ in the sulfate product.

Although oxidative sulfide weathering processes produce little fractionation of sulfur isotopes, in some cases, such as in the Archean settings that are the focus of this study, combined multiple sulfur isotope indices (S-32, 33, 34, 36) are a unique tool to distinguish between sulfur source rocks formed before and after 2.0 Ga (*Li et al., 2016*). This is because the geological and biological processes on Earth generally obey a mass-dependent fractionation (MDF) rule on multiple sulfur isotopes, which is shown as a relationship between the $\delta^{33}S$ and $\delta^{34}S$ values as:

$$1 + \delta^{33}S/1000 = (1 + \delta^{34}S/1000)^{0.515} \quad (1)$$

However, exceptions (i.e., sulfur mass-independent fractionation or S-MIF) have been observed in the geological records, mainly in sulfide minerals as well as a few sulfate minerals, in the Archean period (*Farquhar et al., 2000a; Farquhar and Wing, 2003; Ono et al., 2003*). The S-MIF is generally expressed by non-zero $\Delta^{33}S$ and $\Delta^{36}S$ values, which are defined as Equations (2) and (3).

$$\Delta^{33}S = \delta^{33}S - 1000\times[(1 + \delta^{34}S/1000)^{0.515} - 1] \quad (2)$$

$$\Delta^{36}S = \delta^{36}S - 1000\times[(1 + \delta^{34}S/1000)^{1.89} - 1] \quad (3)$$

To date, the Archean S-MIF signal has been generally accepted as a result of UV induced photochemical reaction of volcanic SO_2 in the Archean anoxic atmosphere with $P_{O2} < 10^{-5}$ of present atmospheric level (PAL) (*Pavlov and Kasting, 2002*). This photolysis of volcanic SO_2 resulted in two major aerosol particles — elemental sulfur with positive $\Delta^{33}S$ values and sulfate with negative $\Delta^{33}S$ values (*Farquhar et al., 2001*). Both elemental sulfur and sulfate aerosols were washed down into the Archean ocean by precipitation and further processed by marine organisms to form sulfur-bearing minerals (mainly pyrite) which would inherit the S-MIF signal from their parent sulfur species. The formation of Archean pyrite could involve reduction and mixing (with various mixing ratios) of both elemental sulfur and sulfate sources and thus result in variable (from negative to positive) $\Delta^{33}S$ values (Fig. 2), in contrast with the universally negative $\Delta^{33}S$ value of sulfate minerals in Archean evaporites (*Farquhar et al., 2000b; Ono et al., 2003; Johnston, 2011*). Although the Great Oxidation Event (GOE) occurred in ~2.45 Ga (*Holland, 1994*), which brought the P_{O2} up to about 1% PAL (*Kump, 2008*) and presumably blocked the S-MIF signal in the air aerosols (*Pavlov and Kasting, 2002*), S-MIF signal (although diminished) still extends to ~ 2.0 Ga in the geological records (Fig. 2), possibly due to the recycling of S-MIF in older sedimentary rocks (*Farquhar and Wing, 2003; Reinhard et al., 2013*). Based on this observation, S-MIF signal can be used as a unique index to distinguish sulfur sources before and after at least 2.0 Ga, possibly 2.45 Ga, depending on the magnitude of S-MIF signal.

Furthermore, examination of combined $\delta^{34}S$ and $\Delta^{33}S$ indices can also put a tighter constraint on sulfur-related microbial processes, such as sulfide oxidation or sulfate reduction. Microbial processes are generally associated with a kinetic isotope fractionation in which light sulfur isotope (^{32}S) being most preferentially used by the microbe. The magnitudes of isotope fractionation, however, vary significantly, with no sulfur isotope fractionation or a small

magnitude of fractionation (within 5‰) for microbial sulfide oxidation (*Taylor and Wheeler, 1994; Toran and Harris, 1989; Poser et al., 2014*), and a huge range from <5‰ (*Harrison and Thode, 1958*) to >70‰ (*Wortmann et al., 2001; Sim et al., 2011*) for bacteria mediated sulfate reduction. In a complicated system, such as the fracture waters that could contain mixed sulfur from more than one source and involve multiple microbial processes, it is difficult to distinguish the source effect from the process effect by solely the $\delta^{34}S$ index. Although both ^{33}S and ^{34}S are discriminated in microbial processes, their magnitudes follow the mass-dependent rule, which results in a $\Delta^{33}S$ value around 0‰. Thus, the addition of the $\Delta^{33}S$ index can help better understand whether the dissolved sulfide and sulfate coexisting in subsurface fracture waters are cognate or unrelated, particularly in the case of Archean sulfur sources with S-MIF signature.

The goals of this study are two folds. The first is to constrain the potential sulfate sources in the subsurface fracture waters of the Witwatersrand Basin. For this goal, I analyzed twenty water samples from two gold fields distributed in the northern and western parts of the basin, respectively. I compared the multiple sulfur isotope compositions of the fracture water sulfate, carbonate associated sulfate (CAS) from the Transvaal dolomites (both measured in this study), and sulfide minerals in the Witwatersrand Basin (published in the literature) to identify the source of dissolved sulfate in the fracture waters. Oxygen isotope compositions of the dissolved sulfate (measured in this study) and hosting water (provided by collaborators) are also integrated to further probe the detailed mechanisms responsible for the formation of dissolved sulfate in the fracture waters. Secondly, I compared the multiple isotope compositions between coexisting sulfate and sulfide dissolved in the fracture waters to differentiate biogenic sulfide produced by microbial sulfate reduction from sulfide supplied from independent sources and further probe any microbial activities in the subsurface fracture waters.

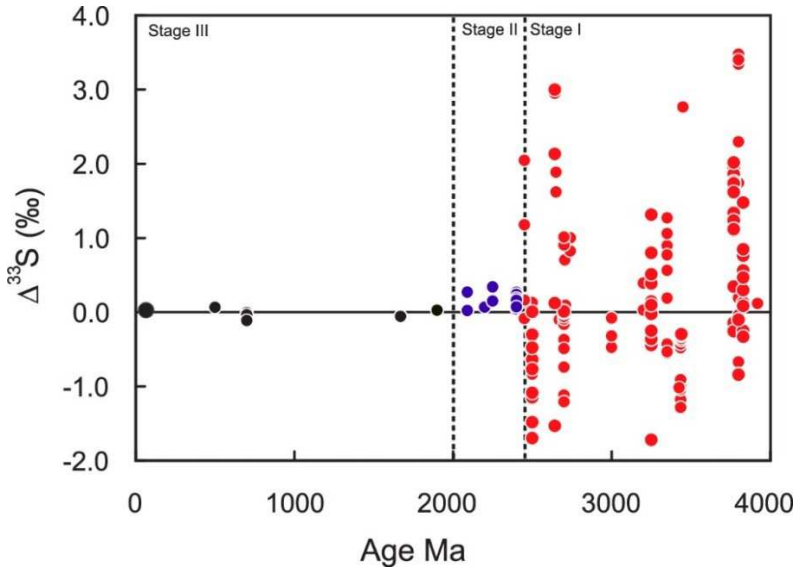

Figure 2. $\Delta^{33}S$ variation along geological time. Stage I, II and III correspond to the age of >3.8 to 2.45 Ga, 2.45 to 2.0 Ga and < 2.0 Ga, respectively (modified from Farquhar and Wing ,2003).

2. Geological background and study sites

2.1. Regional geology

The Witwatersrand Basin in South Africa is one of the world's largest gold reservoirs located in the central part of the Kaapvaal craton (*Robb and Meyer, 1995*). The rock sequences in the Witwatersrand Basin from the bottom to the top are the Dominion Group, Witwatersrand Supergroup, Ventersdorp Supergroup, Transvaal Supergroup and Karoo Supergroup (Fig. 3). These sedimentary sequences unconformably overlie the Archean granite-greenstone basement with ages older than 3086 Ma (*Robb and Meyer, 1995*).

The Dominion Group, Witwatersrand Supergroup and Ventersdorp Supergroup were defined as the "Witwatersrand Triad". The Dominion Group, a volcanic succession consisting of

mafic lavas and volcanic-clastic sediments with minor quartzite, was deposited between 3,086±3 Ma and 3,074±6 Ma in an extensional continental rift environment (*Robb and Meyer, 1995; Omar et al., 2003*).

The Witwatersrand Supergroup was formed after 3,074 Ma but before the onset of the Ventersdorp Supergroup at 2,714 Ma. Following the extrusion of Crown lava, which occurred at 2,914 Ma, the Witwatersrand Supergroup was further divided into two subdivisions – the lower West Rand Group (WRG) and the upper Central Rand group (CRG). The deposition of the WRG was considered as the result of subsidence from the collision of the Kaapvaal and Zimbabwe cratons, and the deposition of the CRG was associated with pulses of regional uplift and SE-directed thrust during the development of foreland basin (*Coward et al., 1995; Robb and Meyer, 1995; Omar et al., 2003*). The WRG was formed in shallow marine or intertidal environment, and mainly composed of shales, sandstones, argillites, greywacke, and minor quartzite (*Duane et al., 1997*), whereas the CRG represents braided stream deposits dominated by conglomerates and fluvial sands with minor shales (*Coward et al., 1995; Robb and Meyer, 1995; Duane et al., 1997*).

Between the Witwatersrand Supergroup and the Ventersdorp Supergroup is the Ventersdorp Contact Reef (VCR), which comprises gold-bearing conglomerate formed after 2,780 Ma (*Robb and Meyer, 1995*). The other two gold reefs, the Carbon Leader Reef (CLR) and the Black Reef (BLR), are located geographically between surface exposures of the WRG and CRG, and between the Ventersdorp and Transvaal Supergroups, respectively (Fig. 3) (*Liebenberg, 1955; Spangenberg and Frimmel, 2001*).

The Ventersdorp Supergroup overlying the Witwatersrand Supergroup comprises the Klipriviersberg Group with an age of 2,714 Ma at the lower part (Fig. 3), the Platberg Group, and the Pniel Group which was further subdivided into the sedimentary Bothaville Formation and the

volcanic Allanridge Formation (*Wronkiewicz and Condie, 1990; Armstrong et al., 1991*). The Klipriversberg Group is essentially a flood basalt sequence that erupted after volcanism in the CRG, and may have undergone the last phase of thrust tectonics (*Coward et al., 1995*). The Platberg Group and the Pniel Group were deposited on the Klipriversberg Group after the uplift of the basin (*Coward et al., 1995*). The Platberg Group largely comprises volcanics (*Wronkiewicz and Condie, 1990*). The volcanic Allanridge Formation forms the upper unit of the Ventersdorp Supergroup, and is considered to have evolved independently from other groups and to represent a separate magmatic episode (*Coward et al., 1995*). Zircon U-Pb dating yielded the age of the Ventersdorp Supergroup around 2,700 Ma, which is much older than the result of 2,370 Ma derived from whole-rock Pb-Pb method (*Van der Westhuizen et al., 2006; Litthauer, 2009*). As younger ages have been also given by Rb-Sr dating, it is suggested that the Ventersdorp Supergroup has undergone metamorphism which could reset the isotopic clock (*Van der Westhuizen et al., 2006*).

The Transvaal Supergroup, which had begun to be deposited on the Ventersdorp Supergroup by 2,557±49 Ma (*Walraven and Martini, 1995; Martin et al., 1998*), can be subdivided into the Chuniespoort Group and the Pretoria Group. The Chuniespoort Group is dominated by dolomites, and currently is a thick aquifer. The Pretoria Group mainly contains quartzites with subordinate carbonate and volcanics (*Wronkiewicz and Condie, 1990*). The Transvaal sediments are considered to have been deposited in a shallow marine environment (*Cameron, 1982*). At around 2,050 Ma, the mafic Bushveld Igneous Complex intruded the Transvaal Supergroup (*Armstrong et al., 1991*).

The Witwatersrand Basin experienced a significant meteoric impact - the Vredefort event, at ~2,025 Ma (*Coward et al., 1995*). Since then, there is no geological record preserved except a young (254 to 190 Ma) sedimentary rocks, the Karoo Supergroup, which appears on the south and

east part of the Witwatersrand Basin (*Duncan and Marsh, 2006*). The vast majority of the Karoo rocks are shales and sandstones (*Duncan, 1987*).

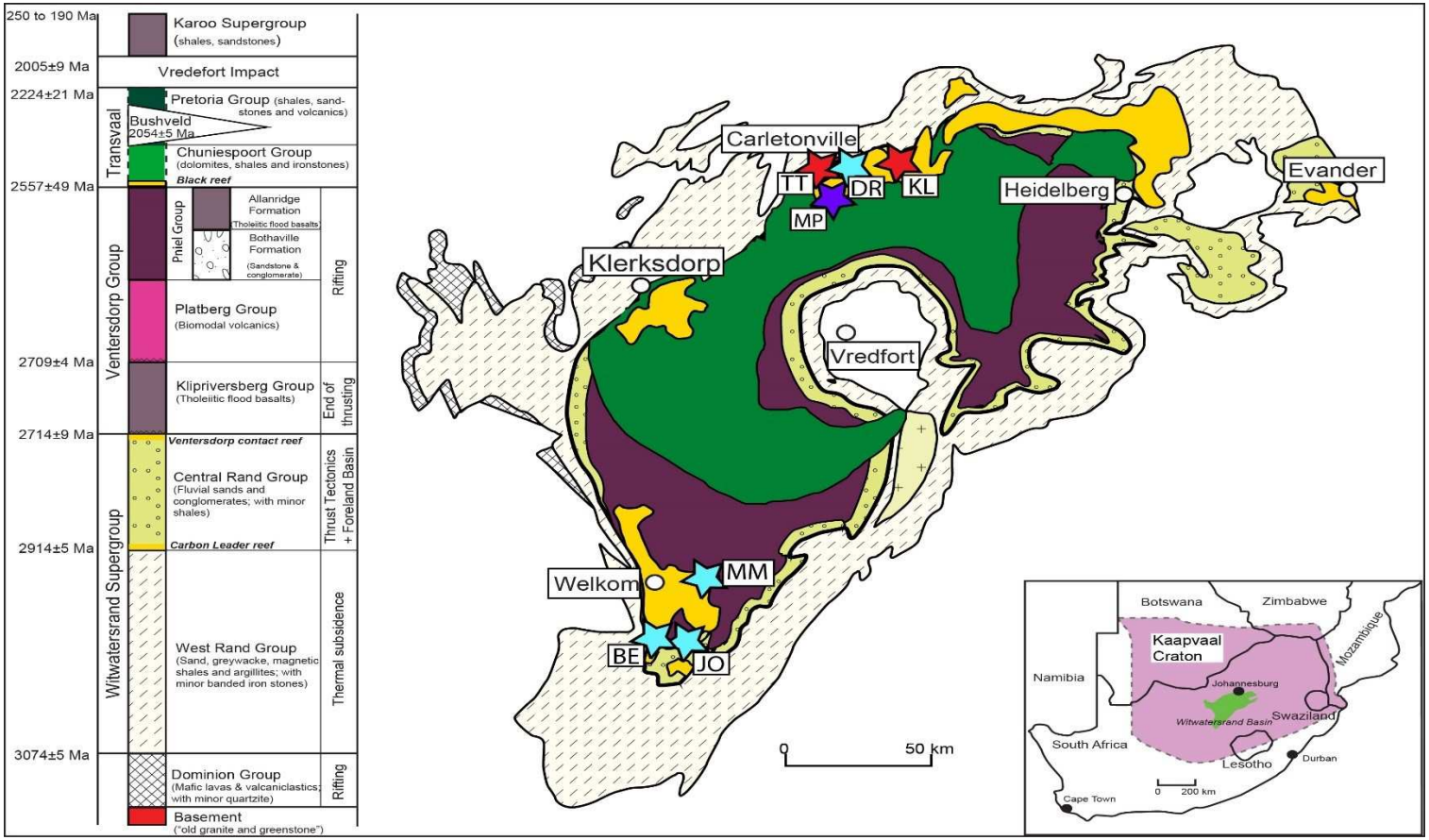

Figure 3. Stratigraphic sequence of the Witwatersrand Basin (left; modified from *Beach and Smith, 2007*) and geological map of the studied area (right; modified from *Jones 1988* and *Dankert and Hein, 2010*). Note that the Karoo Supergroup does not appear in this map. Yellow areas represent five major gold fields (Evander, Heidelberg, Carletonville, Klerksdorp and Welkom). Our subsurface fracture water samples were mainly collected from the Carletonville and Welkom regions, including deep fracture waters from Kloof and Tau Tona gold mines (red stars), and shallow fracture waters from Beatrix, Joel and Masimong gold mines (light blue stars). Another deep fracture water location (Mponeng) studied by *Lin et al., 2006* and *Chivian et al., 2008* is also shown for reference. KL = Kloof, TT = Tau Tona, Mp=Mponeng, BE = Beatrix, DR = Driefontein, JO = Joel, MM = Masimong.

2.2. Study sites

In this study, fracture water samples were collected from two gold mining areas, the Carletonville region and the Welkom region (see Fig. 3). The Carletonville region is located in the northwestern part of the Witwatersrand Basin. Mining-relating drilling has reached 3.5 kmbs in this area. The Kloof, Tau Tona, Driefontein and Mponeng mines are in the central part of the Carletonville area (Figs. 3 and 4). Ten fracture water samples were collected from Kloof, Tau Tona and Driefontein mines with depths from 0.9 to 3.3 kmbs and temperature from 24 to 54.5 °C (see Appendix Tables A1 and A2). No samples were investigated from Mponeng in this study, but a few previous fracture waters samples from 2.8 kmbs in Mponeng have been well studied and a unique single-species (sulfate reducer) ecosystem has been discovered based on 16S rDNA sequences and genomic analyses (*Lin et al., 2006; Chivian et al., 2008*). The Beatrix, Joel and Masimong mines are located in the Welkom region in the southwestern part of the Witwatersrand Basin. Ten fracture water samples collected from these mines with depths ranging from 1.3 to 1.9 kmbs and temperature varying from 31.6 to 40.7 °C (see Appendix Table A1, A2). In Fig. 3, fracture water depths greater than 3 kmbs are labeled in red to set them apart from the shallower water samples from depth less than 1.9 kmbs. It is noted that in the northern part of the Carletonville region, the Witwatersrand Supergroup is overlain directly by the Transvaal Supergroup rather than the Ventersdorp Supergroup (see in Fig. 5 and 6). The Karoo sequence had been removed and left with only around 1 km^2 outcrop in the Carletonville region (*Johnson et al., 1996*). In the north part of Welkom, the Transvaal Supergroup is absent, resulting in the Karoo Supergroup lying directly on the Ventersdorp Supergroup (see in Fig. 7). Detailed stratigraphic successions are only available for the Kloof, Driefontein and Beatrix gold mines and are briefly described below.

In the Carletonville region, the basin is hydraulically compartmentalized by the sub-vertical to vertical, 1.4 Ga Pilansberg dykes cross-cutting all strata from south to north (Ferguson, 1973; Manzi et al., 2013). In Fig. 4, the Oberholzer dyke, Bank fault and Venterspast dyke separate the shafts of Kloof, Driefontein and Tau Tona sites in this study into three compartments (*Swart et al., 2003*). In the northern part of the region, the boundary of exposure limit of the Pretoria Group of the Transvaal Supergroup delineated the unconfined dolomite aquifer in the north and confined dolomite aquifer in the south (Fig. 4). The dykes and faults cross-cutting the strata have been considered to act as conduits for surface meteoric water moving downward to the underlying Ventersdorp and Witwatersrand strata (*Kieft et al., 2005*).

Similar hydraulically compartmentalization also occurs in the Beatrix, Joel and Masimong gold mines in the Welkom region, which has been cut by some Ventersdorp-age dykes and 0.2 Ga Karoo dykes (*Van Niekerk, 1962; Ferguson, 1973*). However, in some compartments, the tectonic stress changes caused re-orientation of dykes and faults, which resulted in decreased connectivity of dykes and faults and consequently declined infiltration of meteoric water (*Omar et al., 2003*).

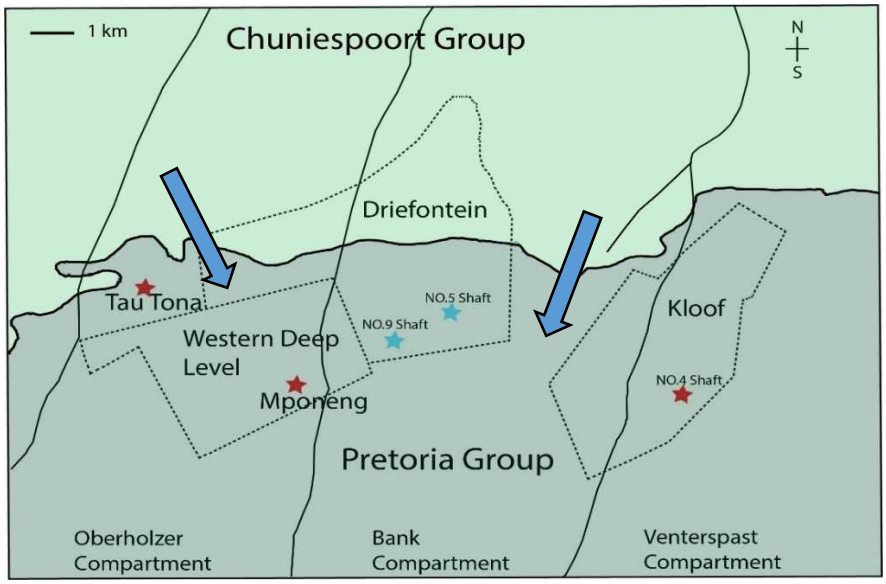

Figure 4. Plan-view map of the Carletonville mining district. The sub-vertical solid lines from left to right are Oberholzer dyke, Bank fault and Venterspast dyke, respectively. The near horizontal solid curve is the boundary between the Chuniespoort Group and the Pretoria Group. The boundary of Kloof, Driefontein and Western Deep Level mines are confined by the dotted line. The stars denote the shafts from where the fracture waters were collected. The blue arrows denote the water flow direction (modified from *Boice, 2004*).

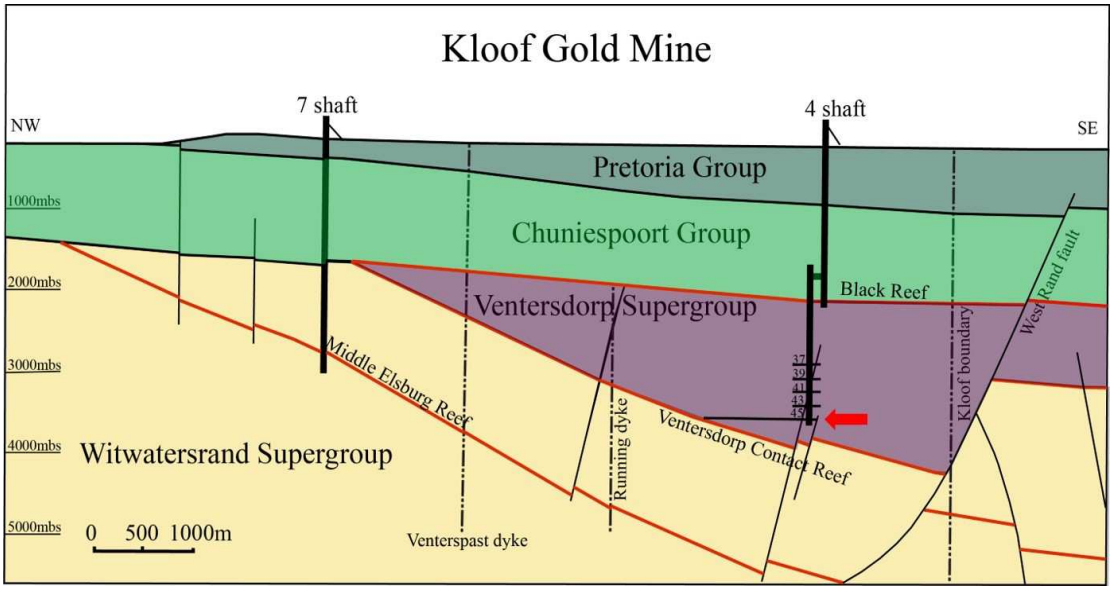

Figure 5. Geological cross section of Kloof gold mine (modified from http://nvp-pgf.org/en/international/characteristics/description). Samples were collected from NO.4 shaft, level 45 (red arrow) at 3276 meters below the surface located in the Ventersdorp Supergroup.

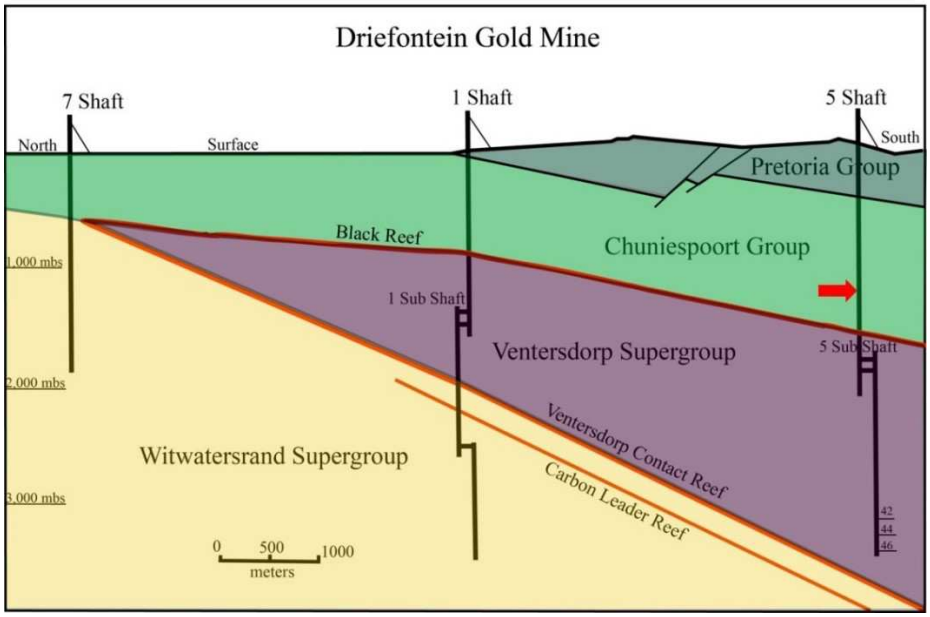

Figure 6. Geological cross section of Driefontein gold mine (modified from https://www.goldfields.co.za/reports/rr_2009/tech_drie.php). Samples from this location were collected from NO.5 shaft (red arrow) at 1046 meters below the surface located in the Chuniespoort dolomite Group.

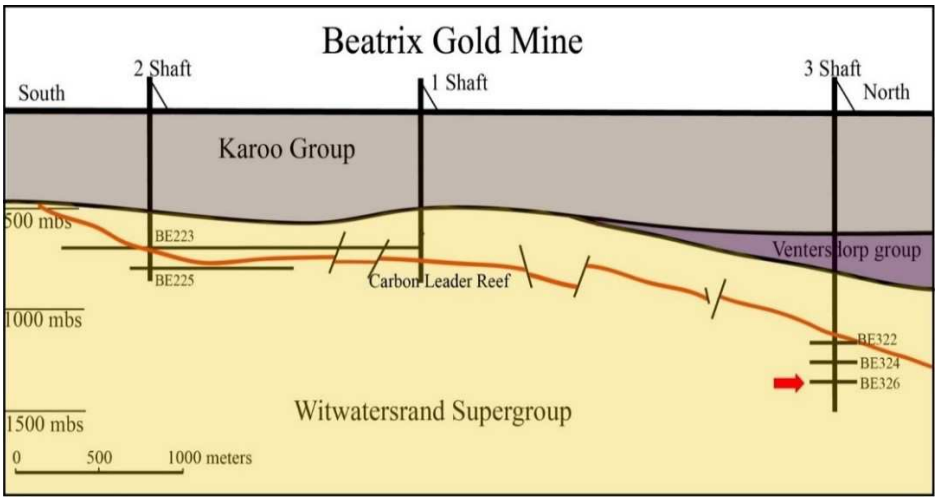

Figure 7. Geological cross section of Beatrix gold mine (Modified from https://www.goldfields.co.za/reports/rr_2008/sa_beatrix.php). Samples from this location were collected from NO.3 shaft, 26 level (red arrow) at 1046 meters below the surface in the Witwatersrand Supergroup.

3. Sample description

3.1. Sample collection

When water-bearing fractures are penetrated by drilling, the water can belch out at a flow rate up to 7.5×10^5 ml/min (e.g., Beatrix gold mine). For sampling purposes, a customized packer with an expandable rubber ring was used to seal the borehole. The ring was connected to a plastic sampling manifold with six quick-connect release valves (*Moser et al., 2003; Boice, 2004*). Pre-cleaned tygon tubing was then connected to the valves to transfer the water from borehole to sample bottles. Before sample collection, the water was allowed to flow through the packer and associated manifold for a long time to eliminate any potential contamination within the apparatus (*Ward et al., 2004*). All the sampling equipment were cleaned and sterilized prior to use.

The general water characteristics, including temperature, pH, Eh, conductivity and salinity, were measured onsite by respective field kits. Depending on needs, samples used for analysis of aqueous chemistry were either filtered or unfiltered into serum bottles or Falcon centrifuge tubes (the volume depends on the analytical needs). The filtered samples include waters for dissolved anion, cation and Fe analysis. Cation and Fe samples were stored in acid washed Falcon tubes that were preloaded with 2.5 ml concentrated nitric acid and 2.0 ml concentrated hydrochloric acid, respectively. Water samples for δ^2H and $\delta^{18}O$ analyses were not filtered and were stored in crimp-sealed glass vials without headspace. For sulfur samples, ~ 1g $CdCl_2$ powder was preloaded into a pre-cleaned 1L high density polyethylene bottle to fix dissolved reduced sulfur species (H_2S, HS^- and S^{2-}) to prevent secondary oxidation of these reduced sulfur species to sulfite and sulfate by atmospheric O_2 during the sample storage.

A total of twenty water samples were collected between 2011 to 2013 at the outlets of exploration boreholes from six mines - Kloof, Tau Tona, Driefontein, Beatrix, Joel, Masimong

(see Fig. 3) for sulfur isotope study. In Kloof, two sets of samples were collected from one borehole (No. 4 shaft, 45 level) intersecting the Ventersdorp Supergroup at 3276 mbs in an 8-day interval (Fig. 5). In Tau Tona, five sets of samples were taken in 2011 and 2012 from three different boreholes intersecting the Witwatersrand sequence. Two sets of dolomitic aquifer water samples were collected in 2011 to 2012 in Driefontein gold mine from two boreholes (No. 5 and No. 9 shafts; see Fig. 6) at 900 and 1046 mbs, respectively. Five pieces of Transvaal dolomite rock samples (the host rock of the Driefontein waters) were also collected close to the drill hole at 1046 mbs in the No. 5 shaft for sulfur source (i.e., CAS) constraints. During 2011 to 2013, eight sets of fracture water samples have been taken from two different boreholes (No. 3 shaft, 26 level) in Beatrix, which intersected the Witwatersrand Supergroup at 1339 mbs (Fig. 7). Each set of samples were collected from Joel and Masimong in the Witwatersrand sequence with depths at 1300 and 1900 mbs, respectively.

3.2. Water sample characterization

As a collaborating project with several international teams (including Dr. Tullis C. Onstott's team at Princeton University, Dr. Barbara Sherwood Lollar's team at the University of Toronto, and Dr. Esta van Heerden's team at the University of the Free State, Bloemfontein, South Africa), the aqueous chemistry (anions and cations) and stable isotope composition ($\delta^{18}O$ and $\delta^{2}H$) of the fracture waters have been analyzed by the Princeton team and the Toronto team, respectively. Summarized below are the geochemical features of the fracture waters samples used in this study based on the data (see Appendix Tables A1-2) provided by the Princeton and Toronto teams.

The temperature of fracture water varies between 24 °C and 54 °C and shows a trend with higher temperatures at greater depth (Fig. 8a). The water samples display near neutral to alkaline

conditions, but their pH values show no depth dependence (Fig. 8b). The Eh values of the water samples range from -132.8 to +373.6 mV. The fracture waters from Joel, Masimong and Driefontein display positive Eh values, implying relatively oxidizing environments, whereas the water sample from Kloof show negative values, implying relatively reduced environment. In contrast, Eh values in Beatrix and Tau Tona vary significantly between negative and positive values at different levels (for Tau Tona) and in different time of the same borehole (for Beatrix). It is still unclear that these large Eh changes in Tau Tona and Beatrix reflect the true environmental variation in the fracture water or simply artificial effects during sampling. The redox conditions do not show clear relationship with depths (Fig. 8c). Based on TDS values, the fracture waters are saline (> 10,000 mg/L) in Kloof, brackish (>1000 to <10,000 mg/L) in Beatrix, Joel and Masimong, and fresh waters (<1000 mg/L) in Driefontein and Tau Tona (Fig. 8d). Compared with the saline subsurface fracture waters from Kidd Creek, Thompson, Sudbury and Yellowknife mines in the Canadian Shield (*Frape et al., 1984*), the fracture waters from the Witwatersrand Basin show much lower Cl^- and TDS concentrations, except for the Kloof samples, whose TDS reaches 10,000 mg/L, parallel to the saline fracture waters in the Canadian Shield. The major element data (Appendix Tables A1 and A2) show that the fracture waters from the Witwatersrand Basin, despite their salinity, are the Na-Cl type (Fig. 9), similar to those from the Canadian Shield (*Li et al., 2016*).

The $\delta^{18}O$ and $\delta^{2}H$ values of most of the water samples lie on the Global Meteoric Water Line (GMWL) or the Local Meteoric Water Line (LMWL) (Fig. 10), yet are smaller than the average value of modern annual precipitation from the closest station in Pretoria, South Africa (*IAEA/WMO, 2002*). The Kloof samples are the only ones deviating away to the left side of GMWL.

Dissolved sulfate was detected universally in all samples. Sulfate concentrations are mostly in the range of 100-600 μM except the sample from Masimong, which is only 7 μM. Despite the

large concentration variations for the shallow waters, deep fracture waters (from Kloof and Tau Tona gold mines) show low sulfate concentrations around 100 μM (Appendix Table A1; Fig. 11), similar to the values of the deep saline fracture waters from Kidd Creek in the Canadian Shield (*Li et al., 2016*). On the other hand, TDS dos not seem to have any control on the sulfate concentrations (Fig. 12). Sulfite has also been detected in a few samples (Table A1 and A2), but the amount is generally less than 8% of that of sulfate (except three samples from Beatrix, which are up to 27%). Sulfide concentrations in the water samples vary significantly, from below detection limit (2 μM) to nearly 200 μM. Compared with sulfate concentrations, sulfide concentrations are much lower in most of the samples, but can be higher (e.g., in the samples from Tau Tona 118 shaft and Masimong 546 shaft).

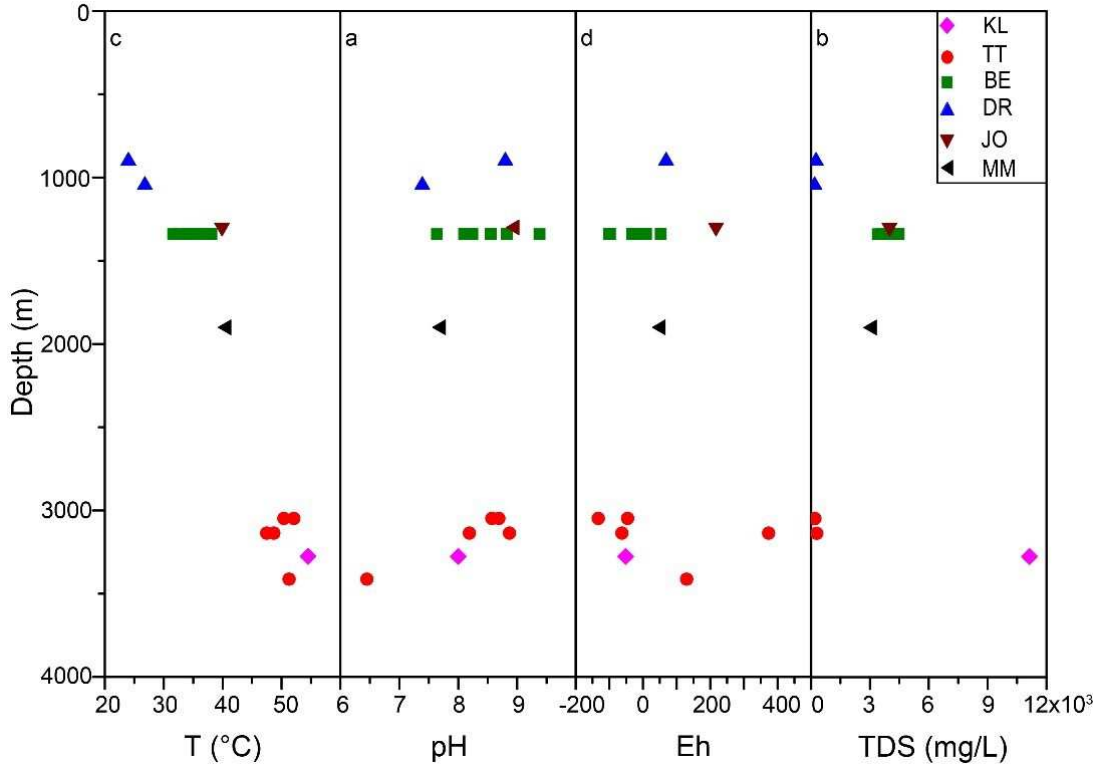

Figure 8. Along-depth variation of (a) temperature, (b) pH, (c) Eh, (d) total dissolved solid (TDS) of fracture waters from different locations. KL = Kloof, TT = Tau Tona, BE = Beatrix, DR = Driefontein, JO = Joel, MM = Masimong.

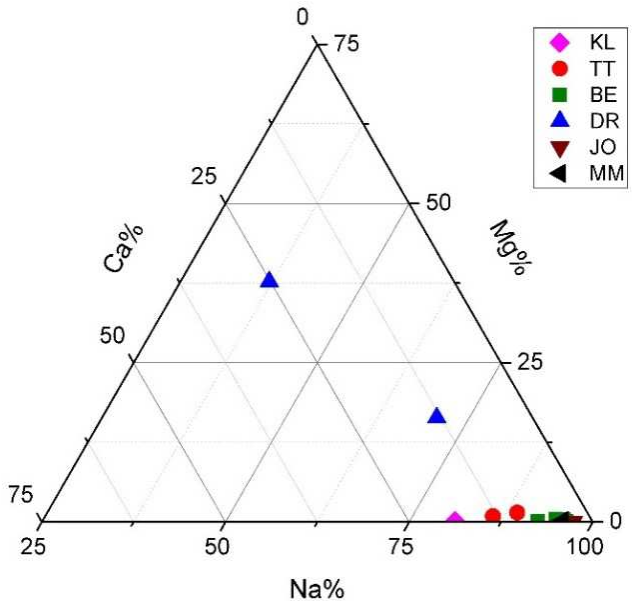

Figure 9. Ternary plot of relative proportions of major cation in the fracture waters. Abbreviations are the same as Fig. 8.

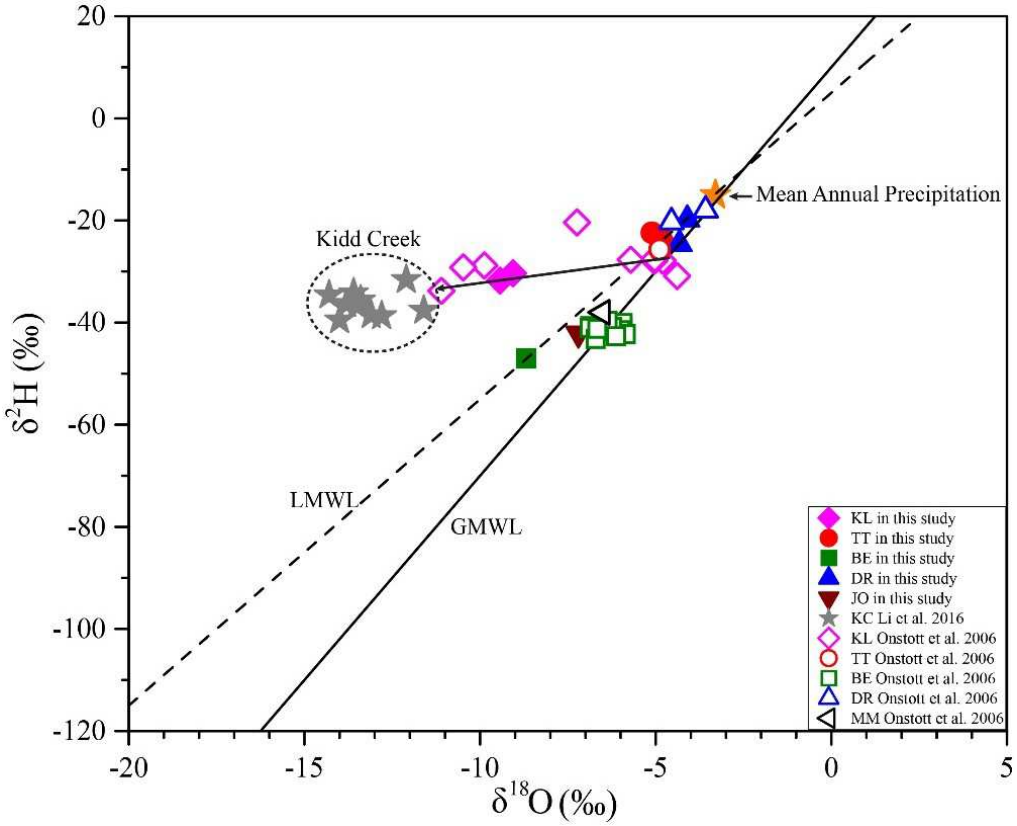

Figure 10. $\delta^{18}O$ versus $\delta^{2}H$ diagram of fracture water samples. The error bars are smaller than the symbols. For comparison, Global Meteoric Water Line (GMWL; *Craig, 1961*), Local Meteoric Water Line (LMWL; *Mazor and Verhagen, 1983*), previous fracture water samples from Kloof, Tau Tona, Beatrix and Masimong gold mines (*Onstott et al. 2006*), modern mean annual precipitation from Pretoria, SA (filled circle; *IAEA/WMO, 2002*) and saline water from Kidd Creek in Canadian Shield (*Li et al., 2016*) were also plotted. Abbreviations are the same as Fig. 8.

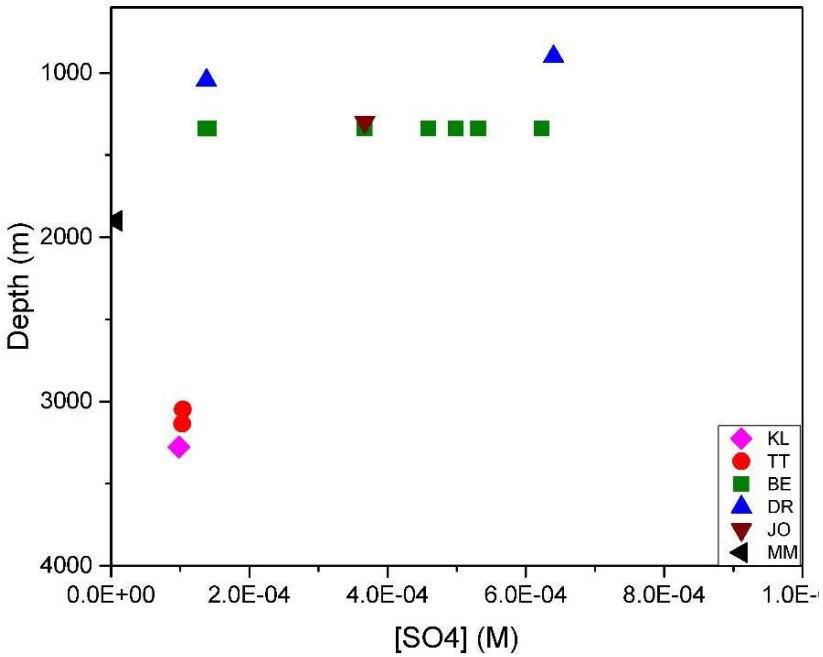

Figure 11. Sulfate concentration of fracture water from various depths. The error bars are smaller than the symbols. Abbreviations are the same as Figure 8.

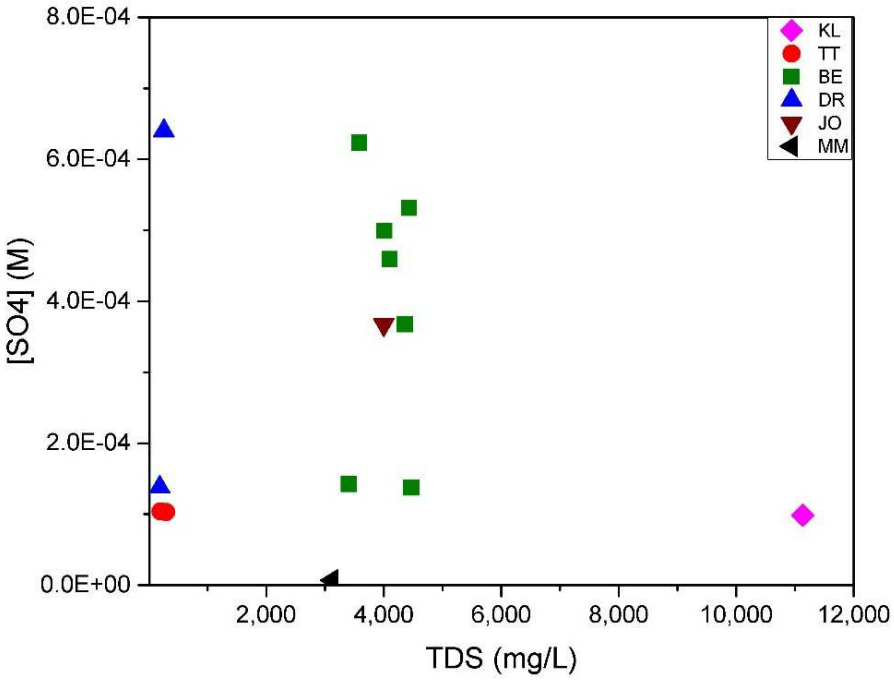

Figure 12. Plot of dissolved sulfate concentration vs. TDS. The error bars are smaller than the symbols. Abbreviations are the same as Figure 8.

4. Analytical methods

4.1. Sample preparation

This study is focused on the sulfur isotope samples, targeting on dissolved sulfide and sulfate in the fracture waters and CAS in a few Transvaal dolomite rock samples. Drill core samples have not been available from the other mines so far, so direct comparisons of the sulfur isotope compositions of the fracture waters and their host rocks have not been achieved for those mines.

4.1.1. Dissolved sulfide and sulfate in fracture water

Sulfur samples were extracted and prepared in Professor Long Li's stable isotope geochemistry laboratory at the University of Alberta. The first step was to separate sulfide from sulfate in the water samples. Because dissolved sulfide had already been fixed onsite during sample collection by $CdCl_2$ as yellow CdS precipitation in the waters, it was easy to be separated by filtration in the laboratory. The filtered CdS was rinsed three times with ultrapure MQ water. The yellow powder together with the filter paper were then put into an oven to dry at 60 °C overnight. Finally, the dry CdS was weighed and wrapped in clean aluminum foil.

The residual water after filtration was concentrated on a hot plate at around 80 °C until the volume reduced to less than 150 ml for easy operation in the next steps. After the water cooled down to room temperature, 2N HCl was slowly added to the water until pH reached around 3. The water sample was then heated on a hot plate to 80 °C to remove carbonate species, which would otherwise induce precipitation of $BaCO_3$ and affect the oxygen isotope compositions of sulfate. After the water cooled down, saturated $BaCl_2$ solution was added to precipitate sulfate ion as barite, which was then filtered, rinsed and dried overnight in an over at 60 ºC. The dried $BaSO_4$ was then weighed and wrapped in clean aluminum foil for storage.

4.1.2. CAS extraction

To effectively extract CAS from the dolomite samples, five rock samples were pulverized into fine powders after removal of the weathered/stained surface material. The powders were investigated for their mineral composition by X-ray Diffraction (XRD) using a Rigaku Geigerflex powder diffractometer. Approximately 1g powder of No.1 sample (DR-IPC5-01) was mounted on a slide and irradiated with X-rays emitted from a cobalt X-ray tube operated at 38 kV and 38 mA. The X-rays generated from the powdered sample were detected with diffractometer that recorded between 5 and 90° 2θ with a scanning speed of 2° per minute. The diffraction pattern of the sample powder confirms that the wall rocks in the Transvaal sequence hosting the water reservoir from Driefontein gold mine are dominated by dolomite along with subordinate quartz (Fig. 13). As sulfate ion can replace carbonate ion in the lattice of calcite and dolomite (*Staudt et al., 1994; Pingitore et al.,1995*), trace amounts of sulfate may be found in carbonate rocks. A well-established protocol (*Burdett et al., 1989; Kampschulte et al., 2001*) was adopted for CAS extraction in Professor Long Li's stable isotope geochemistry laboratory at the University of Alberta as described below.

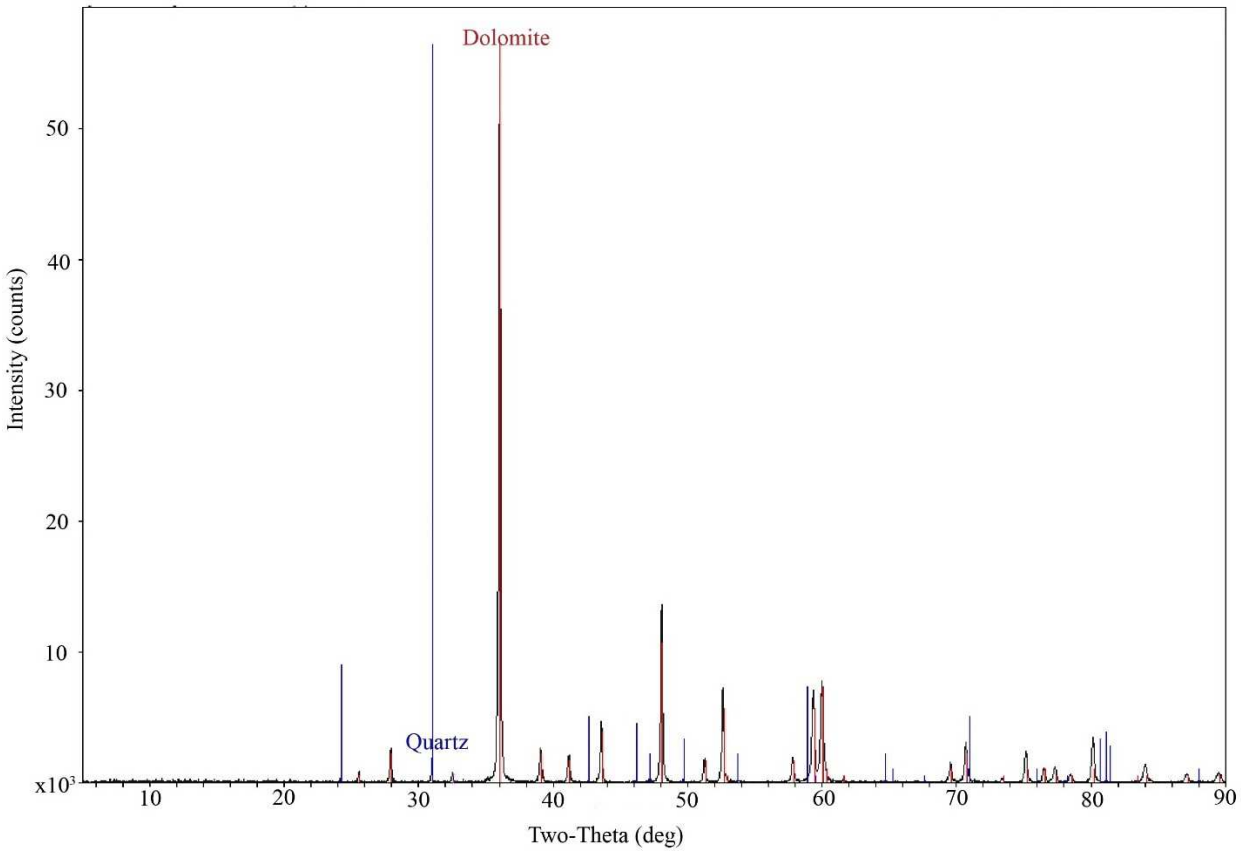

Figure 13. XRD spectrum of the Transvaal dolomite from Driefontein gold mine (DR-IPC5-01).

The sample powders were immersed into 10% NaCl solution for at least 12 hours to dissolve and remove all the secondary sulfate contaminations (*Madgin and Swales, 1956; Blount and Dickson, 1973*) that is not in the carbonate structure. After settling, the solution was decanted. The residue was rinsed with MQ water for at least 3 times, and then immersed in MQ water for another 24 hours. During the latter steps, there was a thin black film (likely light organic matter) floating on top of the solution. Kimwipe paper was used to gently remove the film. The clear solution was decanted and excess 30% H_2O_2 was slowly added to the beaker and allowed to interact with the solution and powder for 48 hours to remove pyrite (if there are any) and organic matter by oxidation. When the reaction finished, the solution was decanted. The residue was washed by

MQ water for 3 times. Finally, 6N HCl was slowly added to the beaker to dissolve carbonate and release structurally bound sulfate into the solution. After 6 hours when the reaction finished completely, saturated $BaCl_2$ was added to the filtered solution to precipitate the trace sulfate as barite. At the end, the barite product was filtered, dried, quantified and wrapped in clean aluminum foil for storage.

4.1.3. EMPA examination of sulfate distribution in the Transvaal dolomite

Moreover, in order to identify the distribution patterns of sulfate in the Transvaal dolomite samples, polished thin sections were prepared for Electron probe microanalysis (EPMA) at University of Alberta. Thin sections of No.3 and No.4 sample (DR-IPC5-03/04) were chosen and coated with 25 nm carbon. The standards used for element concentration calibrations were rhyolite glass for sodium (Na), dolomite for calcium (Ca) and magnesium (Mg), siderite for iron (Fe), strontianite for strontium (Sr), willemite for manganese (Mn), and anhydrite for carbonate associated sulfate. The analysis was performed using wavelength dispersive spectrometry (WDS) on a Cameca SX 100 electron microprobe at 15 kV accelerating voltage, 20 nA beam current and a 5 μm focused beam. On-peak counting time for Na, Ca, Mg, Fe, Sr, Mn was 30s, whereas for sulfur was 60s. Counting times on the high and low (off-peak) background positions were 15s each. The X-ray counts for Sr were aggregated from counts obtained on two spectrometers, which resulted in lower detection limits. Net counts for each element at the peak position were calculated by subtracting linearly interpolated background counts at that spectrometer position from measured peak counts. Net X-ray counts for each element were then converted to concentrations using the Armstrong/Love-Scott matrix corrections (*Armstrong, 1995*) as implemented on the Probe for EPMA software (*Donovan et al., 2015*).

Two paralleled traverses with 3 mm interval were selected in the bottom left quadrant and bottom of the No.3 thin section (see Fig. 21). Ninety spots were selected in the first traverse and 180 spots in the second traverse at ~200 μm spacing in the No.3 thin section. In the No.4 thin section, a traverse containing 90 spots with ~200 μm spacing interval in the middle of bottom left quadrant were analyzed. All the results are reported in oxide weight percent with CO_2 calculated by stoichiometry. The detection limit for Na, Ca, Mg, Fe, Sr, Mn and sulfate is 0.015%, 0.015%, 0.010%, 0.017%, 0.017%, 0.015% and 0.0130% respectively.

4.2. Isotope measurement

4.2.1. Sulfur isotope compositions of sulfate and sulfide

The sulfur isotope compositions of sulfide and sulfate dissolved in the fracture waters and CAS in the Transvaal dolomite were measured at Massachusetts Institute of Technology and McGill University. To measure the multiple sulfur isotopic ratios (34/32, 33/32 and 36/32), both CdS and $BaSO_4$ extracts first need to be converted to Ag_2S. The protocols for sulfide (CdS) and sulfate ($BaSO_4$) are slightly different. For sulfide, all CdS extract was loaded into a 250 mL round-bottomed flask, which was put in a heating mantle at room temperature to connect to an extraction line. A N_2 stream was then introduced to the flask and bubbled for 15 min to drive away any dissolved O_2. Subsequently, 40 mL 6N HCl was slowly injected into the flask and reacted with CdS for about 1.5 hours at 130 °C. The produced H_2S was carried by the N_2 stream to a sample tube filled with 30 mL 0.2 M Zinc Acetate (ZnAc) solution to form ZnS. After the sulfide sample was completely converted to H_2S (generally within the first hour of the 1.5-hour reaction) which was fixed by ZnAc, around 2 ml 0.1M $AgNO_3$ solution was added to the sample tube to convert white ZnS to black Ag_2S. In order to accelerate the conversion and precipitation of Ag_2S, the

sample tube was put into ultrasonic bath for a few seconds, and then placed in an 80 °C oven overnight. The next day, the sample tube was centrifuged, the solution decanted, and the Ag_2S precipitate rinsed with MQ water 3 times. This step was repeated 3 times before the sample tube could be put in an oven to dry Ag_2S.

For sulfate samples, to reduce $BaSO_4$ into Ag_2S, all the steps are the same as above except for applying 40 ml Thode Solution (38% HCl + 48% HI + 50% H_3PO_2) instead of 6N HCl in order to reduce $BaSO_4$ into H_2S (*Thode et al., 1961*).

Finally, around 4 mg Ag_2S was wrapped and loaded in a nickel bomb to react overnight at 300 °C with excess fluorine gas, which can convert Ag_2S to SF_6 gas. The SF_6 gas was released from the nickel bomb and further purified by liquid N_2 cold traps and gas chromatography (GC) before sent to a gas-source isotope ratio mass spectrometer (Thermo-Fisher MAT 253) for isotope measurements on four ion beams of SF_5^+ ($^{32}SF_5^+$, $^{33}SF_5^+$, $^{34}SF_5^+$, and $^{36}SF_5^+$). All sulfur isotope data are reported relative to the Vienna Canon Diablo Troilite (VCDT) standard. The analytical reproducibility (1σ) is ±0.1‰, ±0.01‰ and ±0.1‰ for $\delta^{34}S$, $\Delta^{33}S$, and $\Delta^{36}S$, respectively.

4.2.2. Oxygen isotope compositions of sulfate

The oxygen isotopic analysis of barite was analyzed by a TC/EA-CF-IRMS technique (*Kornexl et al., 1999*) at the Isotope Science Laboratory, Geoscience Department, University of Calgary. Before oxygen isotope analysis, all $BaSO_4$ precipitate from the fracture water were examined by Scanning Electron Microscope (SEM) at University of Alberta, to ensure the samples contain no carbonate or hydrosilicic precipitates which would otherwise affect the oxygen isotope results of sulfate. For a total of 20 $BaSO_4$ precipitations, ~1 mg of each sample powder was flattened and stuck with double sided tape on an aluminum stub, carbon coated and then imaged on a Zeiss EVO LS 15 EP-SEM operated at 25 kV accelerating voltage. In Fig. 14, the vast tabular

crystal habit of virtually all the mineral grains indicates that the precipitate essentially pure $BaSO_4$. More details are listed in Table 4.

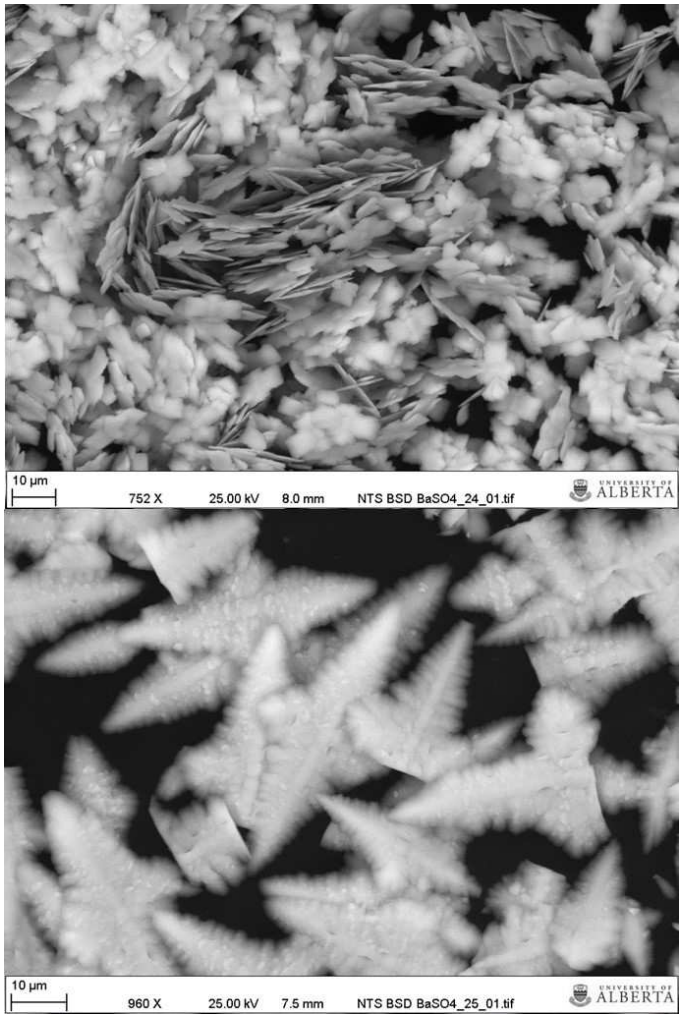

Figure 14. SEM image of sulfate precipitation extracted from fracture water after adding $BaCl_2$ solution.

For oxygen isotopic analysis, 100 to 300 µg barite extract was weighed, wrapped into a high purity silver capsule, and loaded to an auto-sampler on a high-temperature elemental analyzer. $BaSO_4$ was reacted with graphite reactor in the elemental analyzer at 1450 ˚C to produce CO gas,

which was then carried by a helium stream through a GC column to separate CO from N_2. Pure CO was further introduced into an isotope ratio mass spectrometer (Thermo Delta V Plus) for isotope measurements. The $\delta^{18}O$ values were reported relative to the Vienna Standard Mean Ocean Water (VSMOW) standard with an analytical uncertainty of ±0.1‰ (1σ).

5. Results

5.1. Multiple sulfur and oxygen isotope composition of sulfate dissolved in fracture waters

The results of multiple sulfur isotopes and oxygen isotopes for sulfate and multiple sulfur isotopes for sulfide are listed in Table 1.

The overall $\delta^{34}S_{sulfate}$ values show a large range from -5.3‰ to 19.0‰, with the Kloof samples having the highest value and the Driefontein No. 9 shaft sample having the lowest value. All the other samples cluster in a smaller range from 1.2‰ to 11.3‰ (Table 1; Fig. 15). All the sulfate samples except the Kloof samples show non-zero $\Delta^{33}S_{sulfate}$ and $\Delta^{36}S_{sulfate}$ values with $\Delta^{33}S$ values spanning from -0.17‰ at Beatrix to 0.50‰ at Driefontein (Fig. 16), indicating mass independent fractionations up to 50 times greater than the analytical error. There is no obvious depth dependence on either $\delta^{34}S_{sulfate}$ or $\Delta^{33}S_{sulfate}$. The $\delta^{18}O_{sulfate}$ values vary from -1.1‰ to 10.9‰ (Fig. 15). Interestingly, the deeper, higher-temperature samples from Kloof and Tau Tona show similar and much higher $\delta^{18}O_{sulfate}$ range (9.1‰ to 10.9‰) than the shallower samples from the other sites (-1.1‰ to 6.9‰), although the $\delta^{18}O_{H2O}$ values of the Kloof and Tau Tona samples are different (also see Table 1).

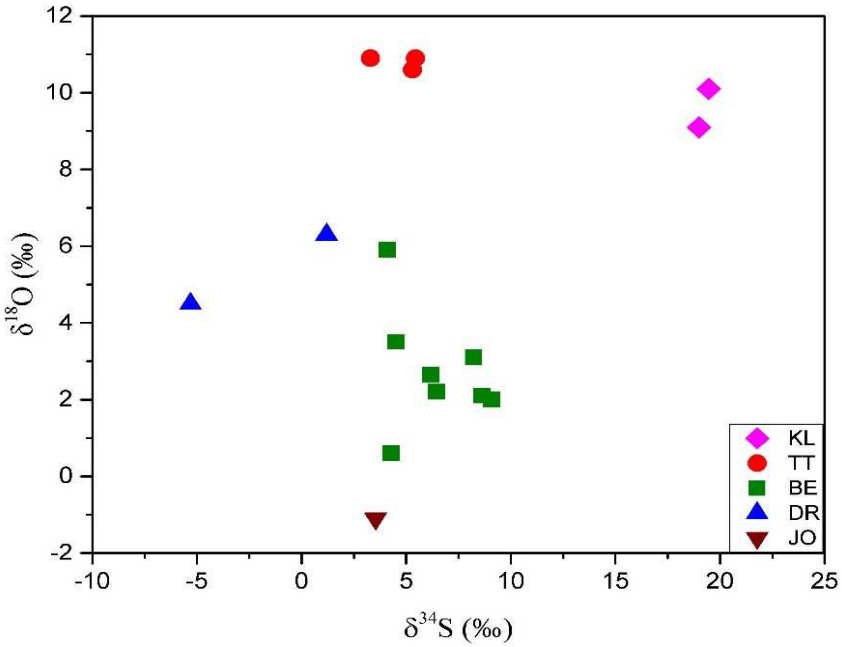

Figure 15. Plot of $\delta^{34}S$ versus $\delta^{18}O$ values of dissolved sulfate in fracture waters. Abbreviations are the same as Fig. 8. The error bars are much smaller than the symbol size.

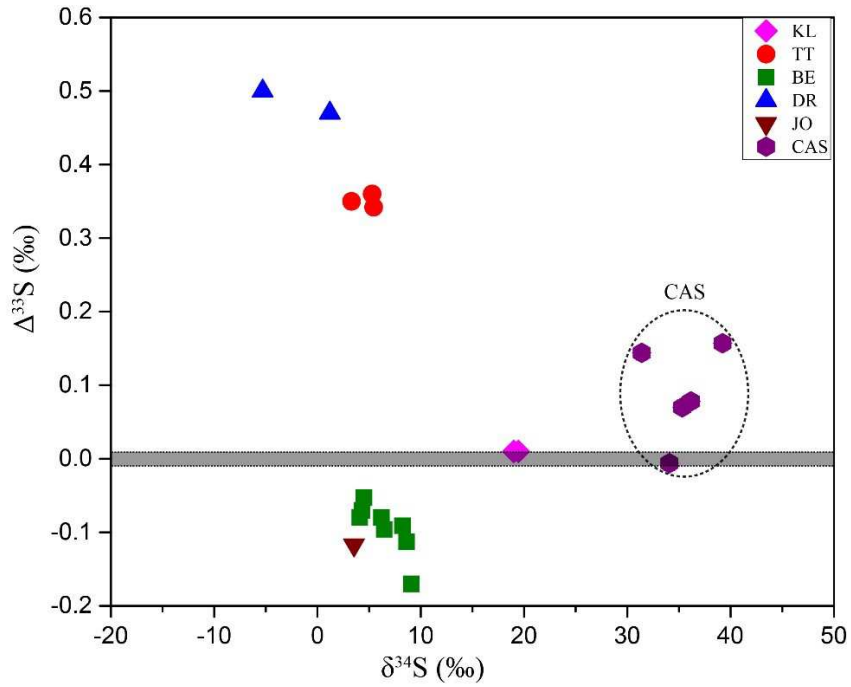

Figure 16. Plot of $\delta^{34}S$ versus $\Delta^{33}S$ to compare dissolved sulfate in the fracture water and CAS in the Transvaal dolomite. The grey band is the analytical uncertainty range. The error bars are smaller than the symbol size. Abbreviations are the same as Fig. 8.

5.2. Multiple sulfur isotope compositions of dissolved sulfide in fracture waters

The $\delta^{34}S_{sulfide}$ values show a large range from -31.7‰ to 13.7‰, with no obvious depth dependence. Most of the $\Delta^{33}S_{sulfide}$ values also display non-zero, but mostly positive values up to 0.68‰ (Table 1).

The $\delta^{34}S$ difference between sulfate and sulfide ($\Delta^{34}S_{sulfate\text{-}sulfide} = \delta^{34}S_{sulfate} - \delta^{34}S_{sulfide}$) in individual samples are between -9.4‰ and 26.4‰. The negative $\Delta^{34}S_{sulfate\text{-}sulfide}$ values all come from the Beatrix samples. When comparing the $\Delta^{33}S$ values between sulfate and sulfide in individual samples, sulfate and sulfide show similar values for samples from Kloof, Tau Tona, and Driefontein (Fig. 17 to Fig. 19), whereas sulfate and sulfide have very different $\Delta^{33}S$ values of the Beatrix samples (Fig. 20). The Masimong sample contains sulfide below detection limit, thus its sulfur isotope composition can not be compared with other samples.

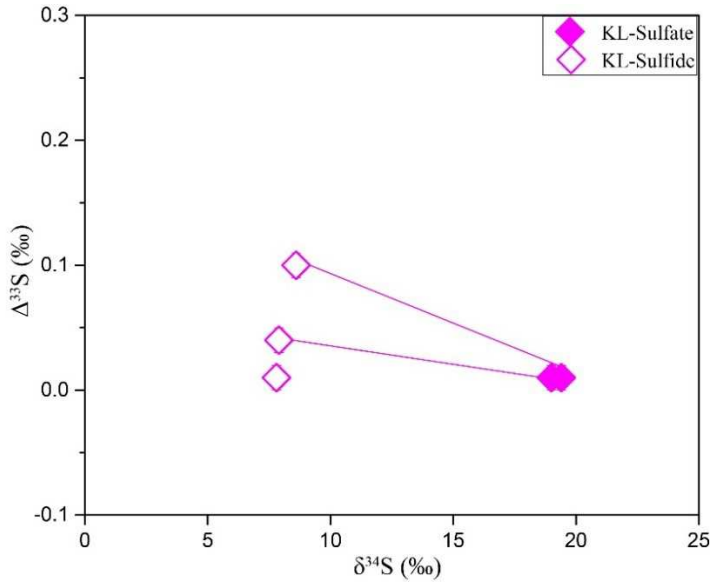

Figure 17. Plot of $\delta^{34}S$ versus $\Delta^{33}S$ to compare dissolved sulfate and sulfide in the fracture waters from Kloof gold mine. Solid line connects the sulfate-sulfide pair in individual water sample. The errors are smaller than the symbol size. Abbreviations are the same as Fig. 8.

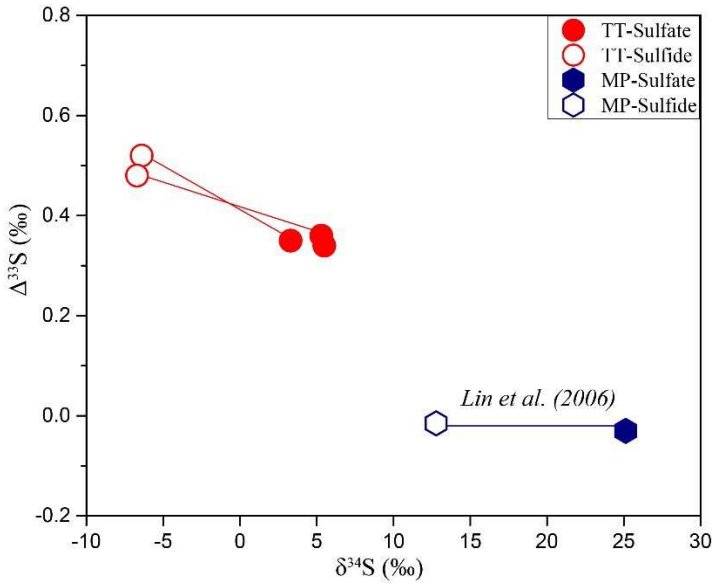

Figure 18. Plot of $\delta^{33}S$ versus $\Delta^{34}S$ to compare dissolved sulfate and sulfide in the fracture waters from Tau Tona and one fracture water sulfate from Mponeng gold mine (*Lin et al., 2006*). Solid line connects the sulfate-sulfide pair in individual water sample. The errors are smaller than the symbol size. Abbreviations are the same as Fig. 8.

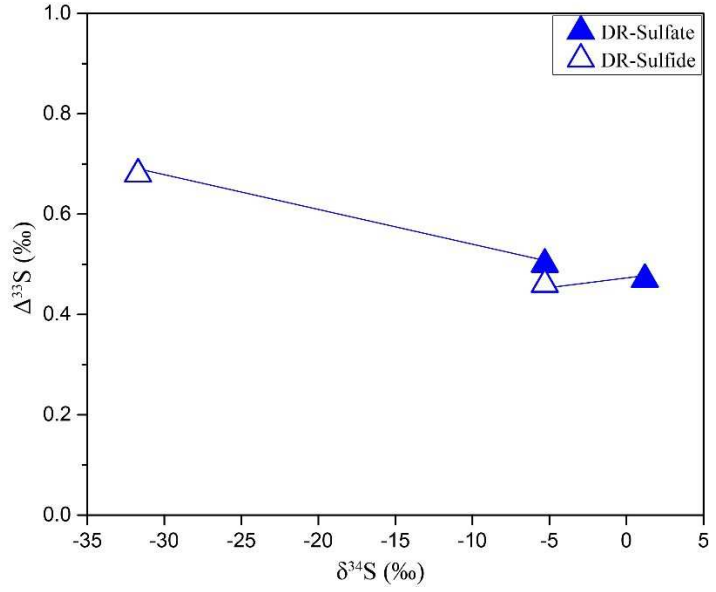

Figure 19. Plot of $\delta^{34}S$ versus $\Delta^{33}S$ to compare dissolved sulfate and sulfide in the fracture waters from Driefontein gold mine. Solid line connects the sulfate-sulfide pair in individual water sample. The errors are smaller than the symbol size. Abbreviations are the same as Fig. 8.

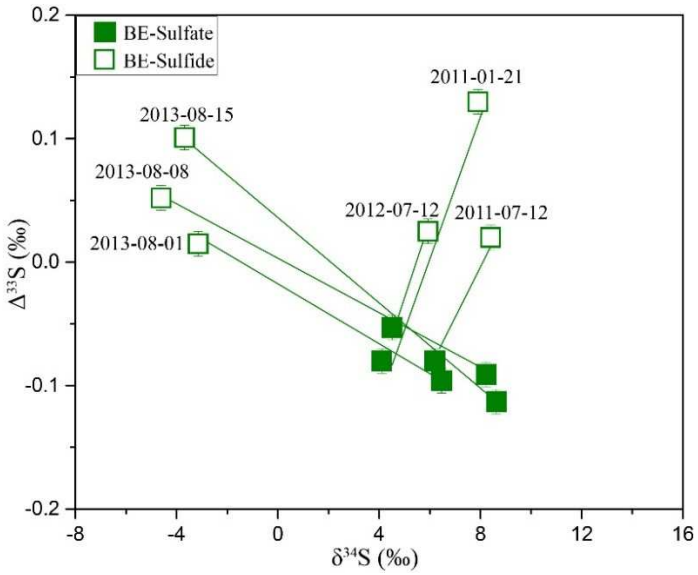

Figure 20. Plot of $\delta^{33}S$ versus $\Delta^{34}S$ to compare dissolved sulfate and sulfide in the fracture waters from Beatrix gold mine at 326 level, borehole 2. Solid line connects the sulfate-sulfide pair in individual water sample. Numbers along the line denote the sample collection date. Abbreviations are the same as Fig. 8.

5.3. Multiple sulfur isotope compositions of CAS

50 to 95 g bulk rock powder of 5 Transvaal dolomite samples was used to extract CAS, which yielded sulfate contents from 0.0049% to 0.0087% (Table 2). EPMA analysis shows the average sulfate content (shown as SO_3%) of No.3 and No.4 Transvaal dolomites (DR-IPC5-03/04) varying from 0.0047% to 0.0168% (Table 3). The details of selected spots analyzed by electron probe in both traverses of No.3 sample is displayed in Fig. 21, where the majority of the spots show values below the detection limit (0.0130%) and the maximum sulfate content is 0.1385% (more data are showed in Appendix Table A3). The CAS show very high $\delta^{34}S$ values (from 31.4‰ to 39.2‰) and small $\Delta^{33}S$ values from -0.01 to 0.16‰ (Table 2), which are very different to those of the fracture water sulfate (Fig. 16). The insoluble material after the CAS extraction protocol from one

of the samples was also analyzed for multiple sulfur isotope compositions, and yielded $\delta^{34}S$ value of 2.3‰, $\Delta^{33}S$ value of 2.66‰ and $\Delta^{36}S$ value of -2.1‰ (Table 2).

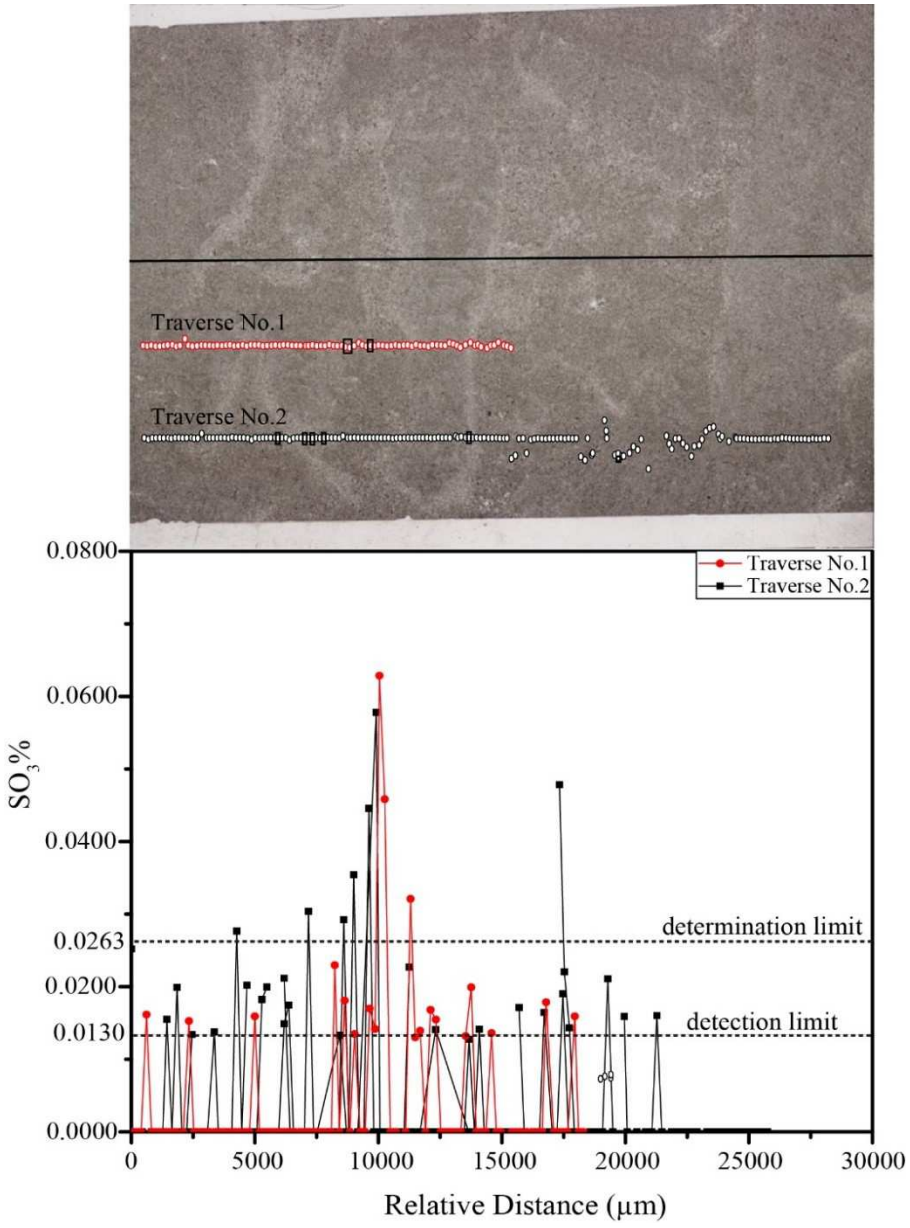

Figure 21. Cross-section variation of sulfate concentration (shown as SO_3%) in Transvaal dolomite thin section from Driefontein gold mine (DR-IPC5-03). The interval of each selected point is 200 μm. The red dots represent traverse No.1 line, and the black dots are traverse No.2. The square denotes the spot displaying the SO_3% concentration that larger than determination limit along the traverse.

6. Discussion

6.1. Origin of the subsurface fracture waters

The fracture waters collected from different depths in the Witwatersrand Basin show a general trend from fresh to brackish waters in relatively shallow depths to more saline waters at greater depths (Fig. 8d), except samples from the Tau Tona mine which show similar geochemical characteristics with the Driefontein dolomite aquifer. Oxygen isotope compositions of these waters indicate a water source of meteoric water. These geochemical features are consistent with previous observations on the fracture waters in the Witwatersrand Basin (*Lippmann et al., 2003; Onstott et al., 2006*) and the Canadian Shield (*Frape et al., 1984; Li et al., 2016*), in which the $\delta^{18}O$ and $\delta^{2}H$ values of the fracture waters from each location spread well along a mixing line between local meteoric water and a saline endmember (Fig. 10). The saline endmember is characterized by $\delta^{18}O$ and $\delta^{2}H$ values far on the left of the GMWL (*Li et al., 2016*). This unique isotopic signature has only been discovered in the fracture waters in the Precambrian cratons, such as the Canadian Shield and Witwatersrand Basin in South Africa (*Frape et al., 1984; Ward et al., 2004; Onstott et al., 2006; Sherwood Lollar et al., 2007; Li et al., 2016*). The saline endmember does not match either seawater or sedimentary basin waters, which should both lie on the right side of the GMWL (*Bowers and Taylor,1985*), but rather has been interpreted as surface waters that have undergone intensive water-rock interaction, through which the anions and cations can be enriched by leaching from ancient marine sediments or weathering of igneous rocks (*Stober and Bucher, 1999; Onstott et al., 2006*) and the $\delta^{18}O$ and $\delta^{2}H$ values can be shifted by the deposition of secondary minerals (*Kloppmann et al., 2002*).

Consistent with previous studies (*Lippmann et al., 2003; Ward et al., 2004; Onstott et al., 2006; Sherwood Lollar et al., 2007; Lippmann et al., 2011*), both major element and isotope data

of the samples examined here indicate that, in the Witwatersrand Basin, meteoric water components are dominant in the relatively shallow fractures (<1.9 kmbs), whereas the waters with more saline components may be intersected at deeper fractures. While the deep saline endmember has been demonstrated to be very old (*Lippmann et al., 2003; Holland et al., 2013*), geochronological data suggest that the meteoric water dominating the shallow fracture waters may also be old (*Lippmann et al., 2003*). Lippmann et al. (*2003*) investigated the noble gases and ^{36}Cl dissolved in the fracture waters from several mines at depths of 0.7 – 3.3 kmbs in the Evander, Carletonville and Welkom areas, and obtained residence times of at least 1 Ma and maybe up to 168 Ma for the collected fracture waters. These results clearly show that the meteoric water-dominated fracture waters in the Witwatersrand Basin contain little modern meteoric component but paleo-meteoric water.

Among all the waters that lie on the GMWL, Beatrix and Joel (in the Welkom area) are more ^{18}O-depleted than Driefontein and Tau Tona (in the Carletonville area; Fig. 10). As Beatrix and Joel locate in the southwestern part of the Witwatersrand Basin with higher latitudes, this isotopic difference is likely attributed to the latitude effect on meteoric water.

The Kloof samples are the only saline fracture water available for this study. Two samples collected from Shaft 4 Level 45 show obvious isotopic deviations from the GMWL and LMWL lines, but not as far as some other saline fracture waters collected from different shafts and levels in the Kloof mine (*Lippmann et al., 2003; Onstott et al., 2006*) and the Kidd Creek mine (*Li et al. 2016*), indicating less extent of water-rock interaction or a mixture of paleo-meteoric water and saline end member.

6.2. Origin of dissolved sulfate in the fracture waters

Firstly, the fracture waters show non-zero $\Delta^{33}S$ values from -0.17‰ to 0.50‰ (Table 1; Fig. 16). Although Johnston et al. (*2007*) proposed a theoretical model whereby bacterial sulfate reduction (BSR) on sulfate with zero $\Delta^{33}S$ value could produce some small non-zero $\Delta^{33}S$ values for both sulfide product and the remaining sulfate, the $\Delta^{33}S$ value for the remaining sulfate after BSR is limited to a range from -0.20‰ to 0.07‰, and to produce a magnitude of -0.20‰, it requires significant enrichment in $\delta^{34}S$ from 35‰ to 60‰ (*Johnston et al., 2011*). In the laboratory experiments of thermochemical sulfate reduction (TSR), Watanabe et al. (*2009*) also observed small $\Delta^{33}S$ values for the remaining sulfate (-0.01‰ to -0.06‰). Therefore, the large range of $\Delta^{33}S$ values observed on the fracture water sulfate in the Witwatersrand Basin cannot be fully explained by BSR or TSR. Neither can the data be explained by mixing, which also can only produce a small non-zero $\Delta^{33}S$ value less than 0.1‰ (*Ono et al., 2006*). Therefore, the observed non-zero $\Delta^{33}S$ values from -0.17‰ to 0.50‰ represents a true Archean S-MIF signature.

In the context of the origin of the water that was discussed above, the sulfate could originate from (1) the source of the saline endmember water, (2) paleo-meteoric water, (3) water-rock interaction. Based on the geochemical and isotopic data, the mechanism of water-rock interaction is preferred in this study. The evidence for this preference is given below.

So far, the source of the saline endmember is not yet well understood. The saline endmember could be very old, up to billion years as seen in the Canadian Shield (*Holland et al., 2013*). Based on modeling of cation and anion contents, Katz et al. (*2011*) proposed that the deep saline fracture waters found in the Carletonville and Evander areas were derived from the Carboniferous-Permian seawater. If true, this water source could carry down a significant amount of sulfate to the deep subsurface fractures as the Carboniferous-Permian seawater already

contained sulfate similar to modern seawater level of 28 mM (*Canfield and Farquhar, 2009*). However, there are several inconsistencies between our data and Katz's assumption. Firstly, on the Cl^- vs. sulfate concentration diagram (Fig. 22), the fracture water data do not plot close to seawater or show any mixing trend between seawater and other endmembers. Secondly, if the sulfate originated from the Carboniferous-Permian seawater, the measured sulfate concentration of 0.1 mM (Table 1) in the saline Kloof sample represents only 0.3% of the initial seawater sulfate remaining in the fracture waters. Even considering a dilution effect by mixing of paleo-meteoric water in this sample (based on comparison with other saline waters in the area in previous studies), it can only account for no more than 0.7% of the sulfate in the initial seawater. Such a huge sulfate removal could possibly be attributed to BSR. However, such as high extent (99.7%) of sulfate reduction would have resulted in significant ^{34}S enrichment in the remaining sulfate, e.g., producing a $\delta^{34}S$ value for residue sulfate of 125‰ if we use a normal $^{34}S/^{32}S$ fractionation factor between sulfate and sulfide of 25‰, or a $\delta^{34}S$ value for residue sulfate of about 25‰ if use an unrealistically small $^{34}S/^{32}S$ fractionation factor of 5‰ in these environment. Assuming a $\delta^{34}S$ value of 12‰ for the Carboniferous-Permian seawater sulfate (*Wu et al., 2014*), the expected $\delta^{34}S$ value of the remaining sulfate in the fracture water would be at least +37‰, which is much higher than the measured values of ~+19‰. Thirdly, in Fig. 23, seawater sulfate since the Cambrian has $\Delta^{33}S$ values limited within -0.04‰ to 0.04‰ (*Wu et al., 2014*), which in any case cannot produce the large S-MIF signal with $\Delta^{33}S$ values up to 0.50‰ observed in the fracture water samples (Table 1). Thus the inconsistency in $\delta^{34}S$ and $\Delta^{33}S$ values indicates that it is less likely that the dissolved sulfate in fracture water derived from Carboniferous-Permian seawater or any post-2.0 Ga surface water recharge. In this case, water-rock interaction with Archean rocks is the most possible option accounting for the sulfate in the subsurface fracture waters in the Witwatersrand Basin.

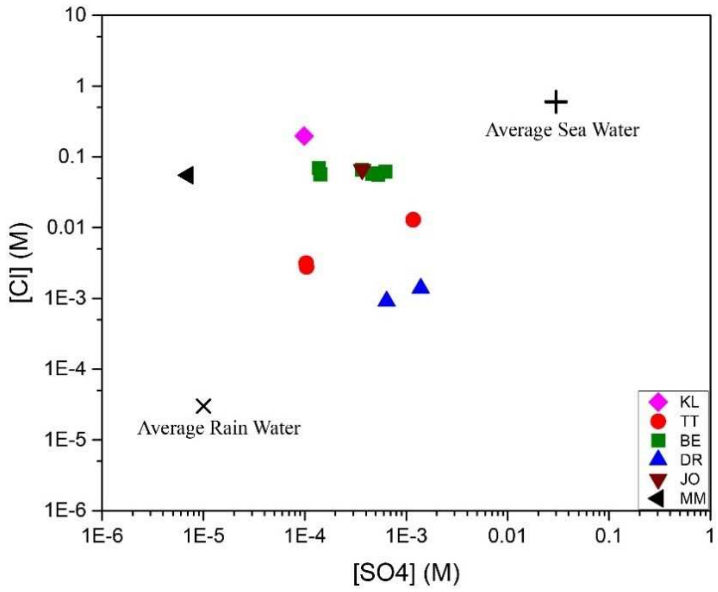

Figure 22. Plot of chloride concentration versus sulfate concentration. The error bars are smaller than the symbols. Abbreviations are the same with Figure 8.

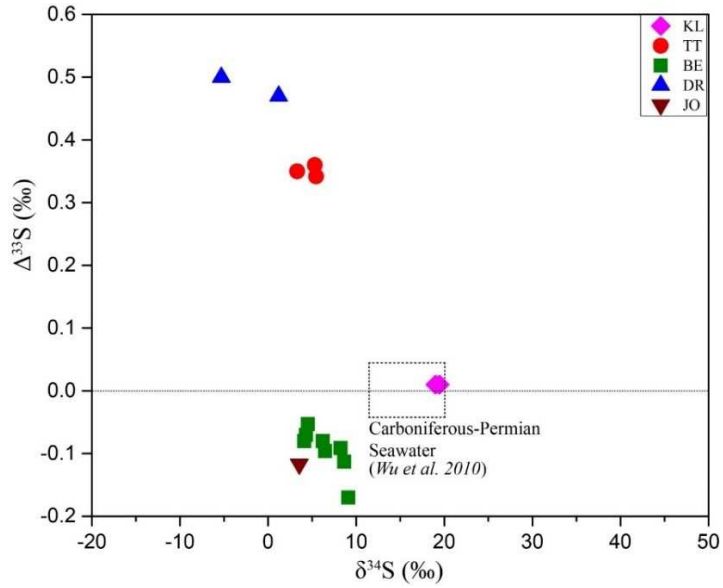

Figure 23. Plot of $\delta^{34}S$ vs. $\Delta^{33}S$ for fracture water samples and Carboniferous-Permian seawater sulfate. The square denotes the range of Carboniferous-Permian seawater sulfate. The error bars are smaller than the symbols. Abbreviations are the same with Figure 8.

During water-rock interaction, sulfate can be transferred to the water by two possible mechanisms: (1) leaching of sulfate from wall rocks (if there is any) or (2) oxidation of sulfide minerals, which are common in the wall rocks.

Due to extremely low sulfate concentrations in the Archean oceans (*Habicht et al., 2002; Jamieson et al., 2013; Crowe et al., 2014*) and lack of free molecular oxygen in the Archean atmosphere (*Pavlov and Kasting, 2002*), sulfate-bearing evaporites were relatively rare in the Archean sediments (*Ohmoto and Felder, 1987*). Although barite beds have been reported in Paleoarchean settings (e.g., the Onverwacht Group and Fig Tree Group, *Wilson and Versfeld, 1994; Nelson et al., 1999*) in the Kaapvaal Craton, to my knowledge, there is no record of barite/gypsum beddings in the Witwatersrand Basin (*Huston and Logan, 2004*). On the other hand, during the formation of carbonate in seawater, sulfate in seawater could replace carbonate ion in the mineral lattice and form so called "carbonate associated sulfate" or CAS. Therefore, trace amounts of CAS are possible in the Transvaal dolomite. Meanwhile, attributed to its high porosity and permeability, the Transvaal dolomite sequence represents a major groundwater reservoir in the area and could be part of the recharge water for the fractures in the underlain Archean sequences (Fig. 3). The CAS is thus a possible leachate that has contributed to the sulfate detected in the fracture waters from Driefontein, Kloof and Tau Tona. However, the sulfur isotopic signature of CAS in the Transvaal dolomite are very different to those of the fracture water sulfate by having much higher $\delta^{34}S$ values and small $\Delta^{33}S$ values of -0.01‰ to 0.16‰ (Fig. 20), which are too small to account for the large $\Delta^{33}S$ variation of -0.17‰ to 0.50‰ observed in the fracture water sulfate and thus exclude the Transvaal dolomite CAS as a major source for the sulfate in the fracture waters.

A more likely process for sulfate production during water-rock interaction is oxidation of sulfide in the host rocks. Archean supracrustal rocks contain abundant sulfide minerals as a result

of the anoxic environments in that period. These Archean sulfide minerals in the sedimentary rocks may have S-MIF signatures at various magnitude from -2‰ to >12‰ (*Farquhar et al., 2000a; Johnston, 2011*), whereas the sulfide minerals in the igneous settings are characterized by S-MDF close to the mantle endmember, due to the lack of exposure to atmospheric photochemical reactions. The most of pyrite minerals from the Witwatersrand Basin show a large $\delta^{34}S$ range from -6.8‰ to 16.5‰ (*England et al., 2002; Watanabe et al., 1997; Hofmann et al., 2009; Guy et al., 2012*) but a small $\Delta^{33}S$ range from -2‰ to +2‰ (*Hofmann et al., 2009; Guy et al., 2012*). The S-MIF values from -0.17‰ to 0.50‰ observed in the fracture waters are well bracketed by the pyrite $\Delta^{33}S$ range of the Witwatersrand Basin (Fig. 24). The diminished $\Delta^{33}S$ range in the fracture waters may reflect a mixing-dilution effect by the sulfate from oxidation of the MDF-bearing sulfide in the Archean igneous rocks, and/or partly the sulfate from the Phanerozoic surface water recharge. The variation of the fracture water sulfate $\Delta^{33}S$ values from place to place can be attributed to the $\Delta^{33}S$ heterogeneity in host rocks and/or the complexity in the conduit network of the fracture water system.

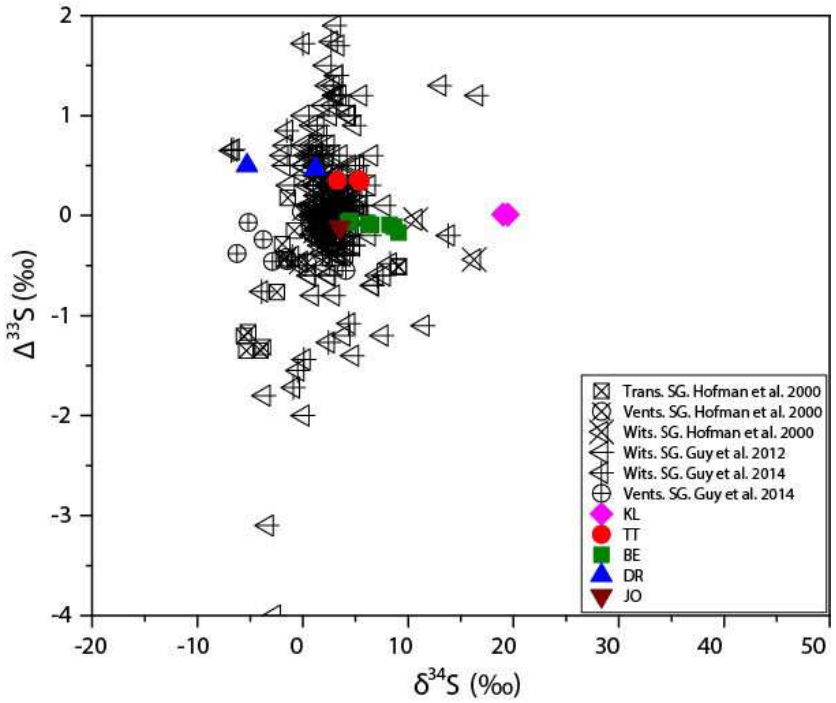

Figure 24. Plot of $\delta^{34}S$ vs. $\Delta^{33}S$ for fracture water samples and sulfide minerals of different sequences in Witwatersrand Basin (grey area). The error bars are smaller than the symbols. Abbreviations are the same with Figure 8.

The timing of sulfide oxidation is an important parameter to constrain in order to understand the energy sustainability for the terrestrial subsurface microbial ecosystems. Unfortunately, sulfate contains no commonly used radioactive elements for direct dating. An indirect method by modeling oxygen isotope exchange between sulfate and water is used here for a ballpark estimate of the time of the sulfate production. The basic assumption for the modeling is that the sulfide oxidation occurred before or as the water infilled the fracture system, but no more sulfide oxidation or sulfate reduction occurred once the water was isolated so that the oxygen isotope compositions of sulfate was solely controlled by the isotope exchange with the water.

According to Lloyd (*1968*), the oxygen exchange rate was calculated as following equation:

$$\ln(1-f) = -kt \qquad (4)$$

in which *f* is the fraction of oxygen isotope exchange, k is the exchange rate constant dependent on temperature, and t is the exchange time. It is suggested that the exchange rates between sulfate and water in low-temperature and neutral conditions are very slow. For example, it takes 250,000 years for 97% exchange of sulfate with seawater at 4°C and a pH of 8.2 (*Lloyd, 1968*). Based on equation (4) and k values measured in laboratory experiments by Lloyd (*1968*), the estimated times for 99% oxygen isotope exchange between dissolved sulfate and fracture water in the Witwatersrand Basin vary from 57,100 to 342,400 years when pH is 9 and from 2,850 to 17,800 years within pH of 7 at the measured borehole temperatures (see in Table 5).

To understand the implication of these modeling results, I further estimated the residence times for the fracture water samples in this study. Based on noble gas isotope (^{3,4}He, ^{36,40}Ar, ^{132,134,136}Xe) and ^{36}Cl analyses, the residence times of a number of fracture waters covering depths from 0.7 to 3.3 kmbs from the Kloof, Driefontein, Beatrix and Evander mines have been determined in the range of 1-168 Ma (*Lippmann et al., 2003*). Boice (*2004*) found that the bromide concentrations in these fracture waters show a positive correlation with their residence times (see Fig. 25). This is explained by the inert chemical properties of bromide, which can accumulate with time by water-rock interaction but is not influenced by participation of secondary minerals and/or diagenetic reactions (*Carpenter, 1978*). Since our samples are from the same mines (or areas) as their samples, this empirical relationship can be applied to our samples to estimate their residence times. The results show a range of 27.6 Ma to 109.2 Ma (Table 5), orders of magnitude higher than the estimated time for sulfate reaching oxygen isotope equilibrium with water. Therefore, oxygen isotope equilibration is expected between dissolved sulfate and fracture water under the presumed scenario.

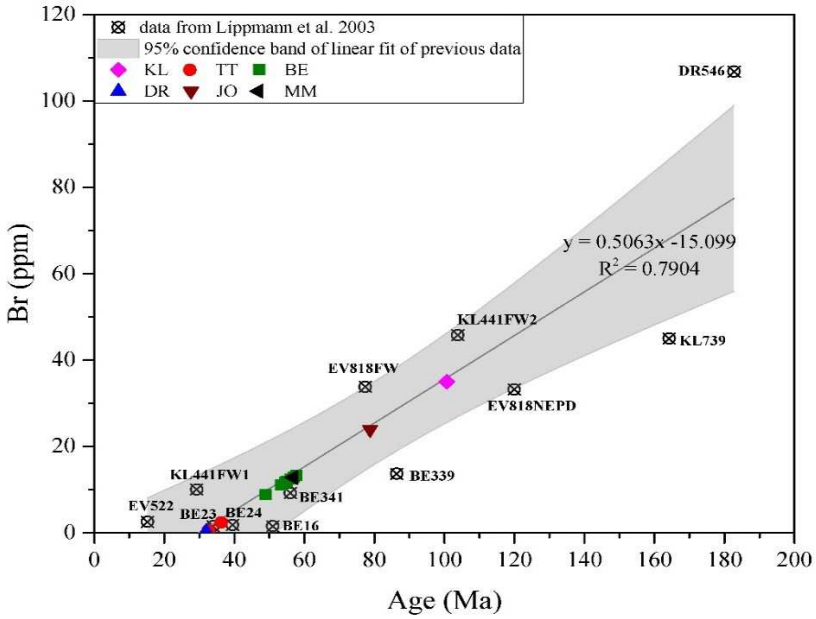

Figure 25. Correlation between Witwatersrand Basin fracture water residence time and bromine concentration. Solid line is the linear fitting of the data from Lippmann et al. 2003 (*Boice, 2004*). The samples in this study from Kloof, Tau Tona, Driefontein, Beatrix, Joel and Masimong mines are plotted for estimation of their residence times.

Halas and Pluta (*2000*) studied the oxygen isotope exchange between sulfate and water under low temperatures (T < 50°C) based on analyses of salty waters from field sites and found an empirical temperature-dependent relationship for oxygen isotope fractionation between sulfate and water, which is written as:

$$10^3 \ln\alpha_{\text{sulfate-H2O}} = 2.41\times10^6/T^2 - 5.77 \quad (5)$$

Zeebe (*2010*) applied quantum-chemistry method to yield a theoretical temperature-dependent oxygen isotope fractionation relationship between sulfate and water from 0 to 150°C, which is given as:

$$10^3 \ln\alpha_{\text{sulfate-H2O}} = 2.68\times10^6/T^2 - 7.45 \quad (6)$$

When we compare our samples with these two relationships, the samples from high-temperature boreholes in Kloof and Tau Tona lie closely to the empirical and theoretical oxygen isotope equilibrium fractionation lines, whereas samples from the other low-temperature boreholes are far below the equilibrium isotope fractionation lines (Fig. 26).

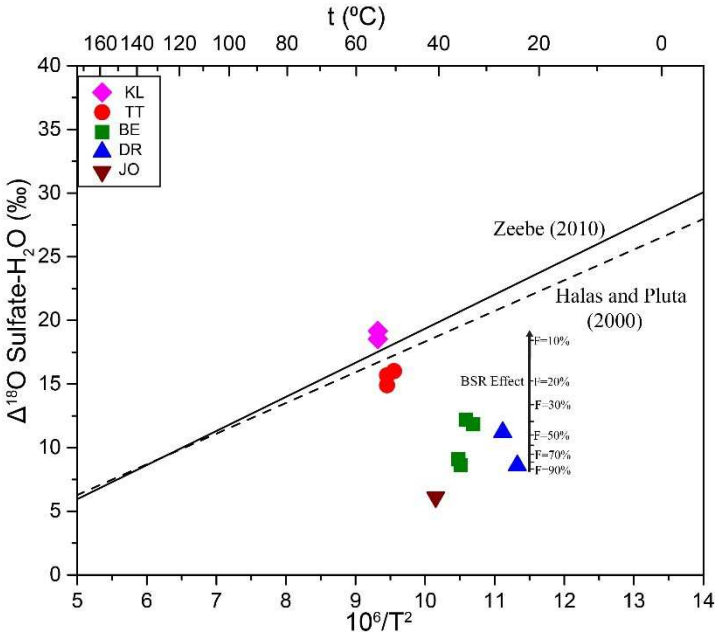

Figure 26. Oxygen isotope fractionation versus temperature for SO_4-H_2O system. Solid line refers to the equilibrium fractionation line by Zeebe (*2010*); dashed line refers to the equilibrium fractionation line by Halas and Pluta (*2000*); filled square represents data from different gold mines in this study. The error bars are much smaller than the symbol size. Abbreviations are the same with Fig. 8.

Due to the long residence time of the fracture waters from previous calculation, besides oxygen isotope exchange with water, other factors, such as water-rock interaction and BSR process, can also affect the oxygen isotopic composition of sulfate (*Wortmann et al., 2007*). BSR involves complicated intermediate species and reaction network. A common pathway is simplified below

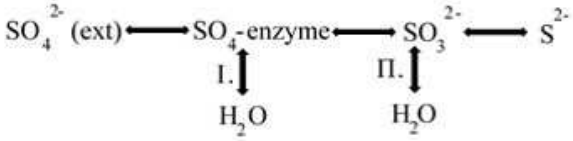

(7)

in which the oxygen exchange could occur between sulfate enzyme complex and water (I) or between sulfite and water (Π) (*Harrison and Thode, 1958; Fritz et al., 1989*). In this reaction network, step I was suggested as the dominant oxygen exchange pathway during sulfate reduction (*Lloyd, 1968; Mizutani and Rafter, 1969; Fritz et al., 1989*).

Within the progress of BSR, the shift of $\delta^{18}O_{SO4}$ can be estimated by a batch model (*Lloyd, 1968*)):

$$\delta - \delta_o = 1000\times(\alpha-1)\times\ln F \quad (8)$$

in which δ_o is the isotope composition of original sulfate, δ is the isotope composition of the remaining sulfate, α is the fractionation factor between sulfate and water, and F is the fraction of the remaining sulfate. If a value of $1000\times(\alpha-1) = -4.6‰$ (*Lloyd, 1967*) is used, the $\delta^{18}O_{sulfate}$ will significantly increase during the BSR process, leading to an increase of $\delta^{18}O$ value between water and sulfate under the assumption that the $\delta^{18}O_{H2O}$ value is a constant during this process since the volumes of the fracture water are much greater than that of sulfate (Fig. 26). Moreover, according to Fig. 10, water-rock interaction can diminish the $\delta^{18}O_{H2O}$ value of Kloof samples, which also greaten the difference of water and sulfate in $\delta^{18}O$ values.

Given that all our samples could have experienced BSR (see discussion in §6.3), it is uncertain whether the apparent oxygen isotope equilibration between the dissolved sulfate and their hosting water in Kloof and Tau Tona was caused by oxygen isotope exchange, BSR or water-rock interaction. In any case, the isotope equilibrium in the Kloff and Tau Tona samples implies that, if there is any sulfate production after the isolation of water, the sulfate productivity is very

slow so that the newly produced sulfate does not impact the overall sulfate at the corresponding oxygen isotope exchange rate. However, the increasing $\delta^{18}O_{sulfate}$ trend from BSR cannot explain the data of the low-temperature samples that lie below the equilibrium isotope fractionation lines (Fig. 26). Therefore, the sulfate production in the low-temperature boreholes should be more recent and have occurred after the isolation or may be still ongoing in the isolated fracture water systems.

The detailed mechanism for sulfide oxidation to produce sulfate, however, is very intriguing. In an environment with free O_2, oxidative weathering, in which microbial process may or may not be involved, is a very common mechanism. The oxygen isotope composition of sulfate product from oxidative weathering of sulfide minerals is complex due to the fact that sulfate may incorporate oxygen from both water molecule and atmospheric oxygen. Associated formation of intermediate sulfur species, which depend on the biological/abiotic reaction conditions, can also have effect on oxygen isotope fractionation.

Oxygen isotope behavior during oxidation of pyrite, the most common sulfide mineral, is by far the most extensively studied. Pyrite oxidation can be generally described by following reactions:

$$FeS_2 + 7/2O_{2\,(aq)} + H_2O \rightarrow Fe^{2+} + 2SO_4^{2-} + 2H^+ \quad (9)$$

$$Fe^{2+} + 1/4O_{2\,(aq)} + H^+ \rightarrow Fe^{3+} + 1/2H_2O \quad (10)$$

$$FeS_2 + 14Fe^{3+} + 8H_2O \rightarrow 15Fe^{2+} + 2SO_4^{2-} + 16H^+ \quad (11)$$

In reaction (9), sulfate oxygen derives from both atmospheric oxygen and water (*Smith et al., 1968*). In reaction (11), sulfate oxygen solely comes from water. Reaction (11) would be significantly promoted in an Fe(III)-preferred environment (*Garrels and Thompson, 1960*), particularly with the existence of bacteria *T. Ferrooxidans* under acidic condition (*Temple and Delchamps, 1953*).

The $\delta^{18}O_{sulfate}$ value of sulfate product from the above reactions depends on the relative contribution from the atmospheric oxygen and water oxygen as well as the associated oxygen isotope fractionation, which can be expressed by the mass-balance equation below:

$$\delta^{18}O_{sulfate}=X\times(\delta^{18}O_{H2O}+\varepsilon^{18}O_w) + (1-X)\times(\delta^{18}O_{O2}+\varepsilon^{18}O_a) \quad (12)$$

in which X and (1-X) represent the fraction of oxygen derived from water and atmospheric oxygen, respectively; $\varepsilon^{18}O_w$ is the oxygen isotope enrichment factor between SO_4 and H_2O, and $\varepsilon^{18}O_a$ is the oxygen isotope enrichment factor between SO_4 and atmospheric oxygen (*Lloyd, 1967; Taylor et al., 1984*). The value of ε may be affected by pH, P_{O2} and/or temperature conditions (*Llyod, 1967*). For example, stoichiometrically, sulfate in Reaction (9) should contain 12.5% water oxygen and 87.5% atmospheric oxygen. However, Lloyd (*1967; 1968*) suggested that the oxygen incorporation ratio between water and atmospheric O_2 was 68% vs. 32% with $\varepsilon^{18}O_w$ = 0‰ and $\varepsilon^{18}O_a$ = -8.7‰. Through pyrite oxidation experiments at pH = 2.0, Taylor and Wheeler (*1984*) obtained $\varepsilon^{18}O_w$ = +4.1‰ and $\varepsilon^{18}O_a$ = -4.3‰ under sterile condition, and with *T. Ferrooxidan*, $\varepsilon^{18}O_w$ = +18‰ and $\varepsilon^{18}O_a$ = -11.4‰ associated with 23% to 100% sulfate oxygen deriving from water. Van Everdingen and Krouse (*1985*) proposed a value of $\varepsilon^{18}O_w$ = -6‰, extending the variation of $\varepsilon^{18}O_w$. The calculation by Toran and Harris (*1989*) suggested water contributed 45-75% of sulfate oxygen in biological experiments and 60-90% in abiotic experiments, whereas Balci et al. (*2007*) suggested that SO_4 contains 85-92% water-derived oxygen in both biological and abiotic pyrite oxidation experiments. Balci et al. (*2007*) also suggested the enrichment factors of $\varepsilon^{18}O_w$ = +3.6‰ and $\varepsilon^{18}O_a$ = -10.0‰ to -10.8‰ in biological pathways, and $\varepsilon^{18}O_w$ = +2.9‰ and $\varepsilon^{18}O_a$ = -9.8‰ in abiotic pathways. In the abiotic oxidation of pyrite by Fe^{3+}, Mazumda et al. (*2008*) reached an average $\varepsilon^{18}O_w$ of +2.6‰ based on an $\varepsilon^{18}O_a$ value of -8.7‰ from Lloyd (*1967*), and the percentage of oxygen derived from water in the range of 83-99.8%. Similar pyrite oxidation experiments were

conducted by Heidel and Tichomirowa (*2010, 2011*), who gave $\varepsilon^{18}O_w = +2.3‰$ and $\varepsilon^{18}O_a = -8.4‰$ with 91±3% incorporation of water molecule for sulfate. So far, it is still difficult to distinguish unambiguously between biological and abiotic sulfide oxidation process based on sulfur and oxygen isotope signatures (*Toran and Harris, 1989; Balci et al., 2007*).

In summary, there exist a significant number experimental constraints and theoretical predictions on the oxygen isotope fractionation factors during oxidative sulfide weathering, which show a huge variation. Since there is no specific study that can be directly applied to the data in this thesis, I plot the previously published data from sulfide oxidation (biotic and abiotic) on the $\delta^{18}O_{sulfate}$ vs. $\delta^{18}O_{H2O}$ diagram in Fig. 27. The three lines in the diagram represent the empirical percentage (100%, 50%, and 0%, respectively) of water-derived oxygen in sulfate with the assumption of no isotope fractionations between sulfate and water or between sulfate and atmospheric oxygen (*Kroopnick and Craig, 1972*). In Fig. 27, previous experimental data fall well within the grey area confined by the 50:50 line and 100% H_2O line. Therefore, this empirical area can be used to represent the possible initial isotope compositions of sulfate product from oxidative sulfide weathering, even though the biotic and abiotic oxidation are not distinguishable. Compared with this empirical area (Fig. 27), the $\delta^{18}O_{sulfate}$ and $\delta^{18}O_{H2O}$ values of our fracture water samples from Driefontein, Beatrix and Joel fall into this area (Fig. 28). Despite the fact that BSR in these samples should have more or less shifted the $\delta^{18}O_{sulfate}$ upwards toward the 50:50 line, the good fit of the isotopic data of these low-temperature fracture waters into the expected area implies that the dissolved sulfate in these fracture waters are likely derived from oxidative sulfide weathering. Again, the data of Kloof and Tau Tona deviate from the expected range, which may be attributed to oxygen isotope exchange with water, and/or sulfate reduction due to much higher temperatures and much more isolated and oxygen deficient environment (especially Kloof).

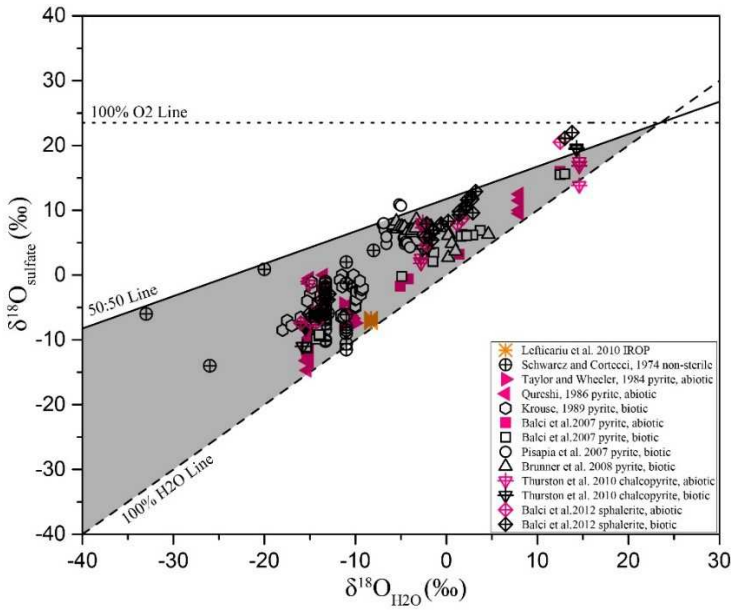

Figure 27. $\delta^{18}O_{SO4}$ vs. $\delta^{18}O_{H2O}$ diagram of theoretical and experimental results of sulfide oxidation. Data from Balci et al. (2007, 2012), Pisapia et al. (2007), Brunner et al. (2008), Lefticariu et al. (2010), Thurston et al. (2010), Qureshi et al. (1986), Taylor and Wheeler (1984), Krouse et al. (1989), Schwarcz and Cortecci (1974). The lines are predicted relationships as sulfate oxygen is derived from 100% H_2O (dashed line), 50% H_2O and 50% O_2 (solid), and 100% atmospheric O_2 (dotted), respectively.

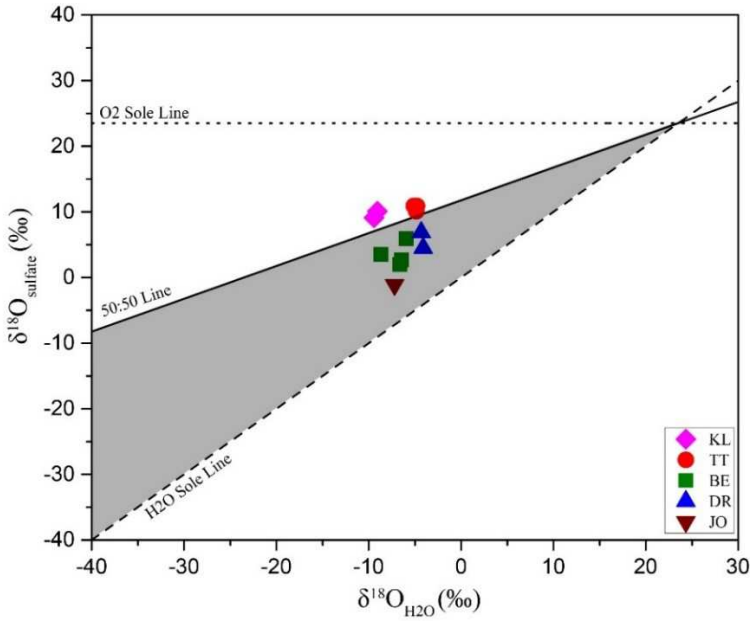

Figure 28. Diagram of $\delta^{18}O_{SO4}$ vs. $\delta^{18}O_{H2O}$ for fracture waters and the empirical *area of initial sulfate* from oxidative pyrite weathering. See text discussion. The error bars are much smaller than the symbol size. Abbreviations are the same with Figure 8.

For the case of the deep fracture waters, particularly for those long isolated, saline and anoxic waters, such as Kloof, sulfide oxidation should be minimal. Therefore, another oxidation mechanism, namely "indirect radiolytic oxidation of sulfide" (IROS), or "indirect radiolytic oxidation of pyrite" (IROP) with pyrite as the dominant sulfide, may become important in contributing sulfate to the fracture waters (*Li et al., 2016*). The IROP can be described by following reaction (*Lefticariu et al., 2010*):

$$FeS_2 + 4HO^{\bullet} \rightarrow Fe^{2+} + S^0 + SO_4^{2-} + 2H_2 \quad (13)$$

In the reaction, the sulfur intermediates species would be oxidized immediately by the free radical to form sulfate. Experiment investigations by Lefticariu et al. (*2010*) gave sulfur isotope fractionations between sulfate product and initial pyrite as +1.5 to +3.4‰. If this reaction occurs in sulfide minerals of host rocks in Witwatersrand Basin, the $\delta^{34}S$ value of sulfate product should vary from -5.5 to 20‰ if the initial $\delta^{34}S$ values of sulfide minerals in the range of -6.8 to 16.5‰, which still bracket the fracture water samples except Kloof (Fig. 29). In addition, the empirical oxygen isotope fractionations between sulfate product and initial water as 1.5‰ (*Lefticariu et al.*, *2010*). In Fig. 27, the oxygen isotope data are close to the 100% H_2O line but away from the Kloof samples, indicating significant oxygen isotope shift of Kloof samples. The much higher H_2 and He contents (e.g., 29 vol% He in the dissolved gas phase) found in the Kloof fracture water (T.C. Onstott, personal communication) confirm this fracture water system has been experiencing significant water radiolysis, which may potentially promote the IROS/IROP reactions as well. However, due to the overlap in both sulfur and oxygen isotope composition of oxidative weathering and IROS, it is difficult to assess the contribution of these two mechanisms independently.

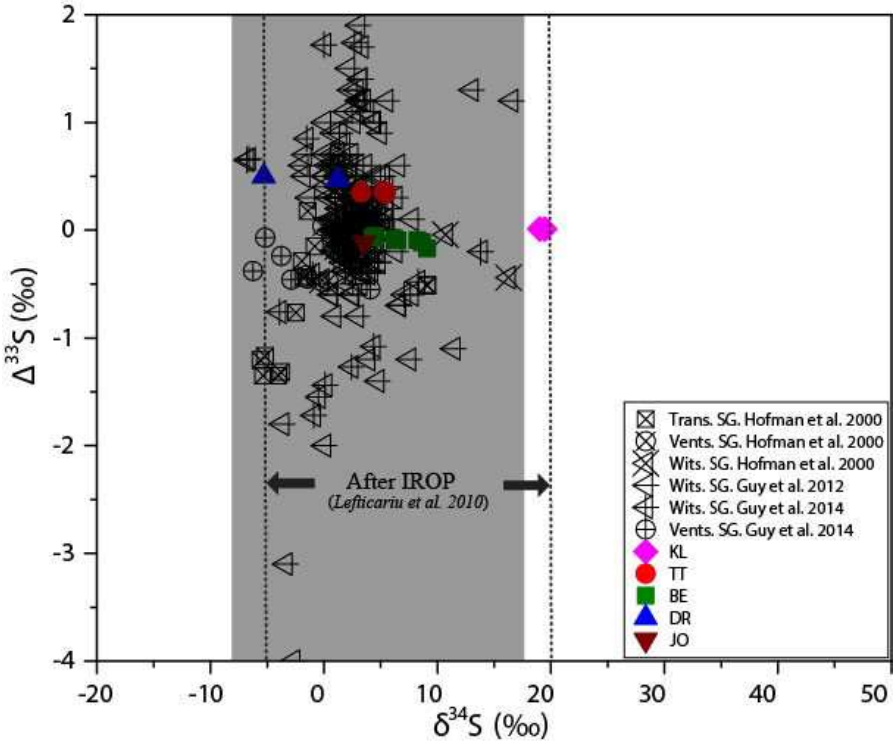

Figure 29. Diagram of $\delta^{34}S$ vs. $\Delta^{33}S$ for fracture water samples and sulfide minerals of different sequences in Witwatersrand Basin. Grey area and dashed line area: initial range of sulfide minerals and after indirect radiolytic oxidation. See text discussion. The error bars are much smaller than the symbol size. Abbreviations are the same with Figure 8.

6.3. Microbial activities in the subsurface fracture waters

Dissolved sulfide has been observed in many fracture water samples co-existing with dissolved sulfate. Because both sulfide and sulfate can be produced by biological processes, the investigation of the genetic relationship between the sulfide and sulfate can shed light on the microbial activities in the deep subsurface and can be used to probe the lower limit of terrestrial habitat.

Johnston et al. (*2007*) found that sulfate-reducing bacteria can also produce small non-zero S-MIF values. The magnitude of fractionation was highly dependent on the temperature and the metabolic pathways (*Johnston et al., 2005*). Based on the biological pathway proposed by Harrison

and Thode (*1958*), Rees (*1973*) proposed a steady-state model for the sulfur isotope fractionation during the BSR process as:

$$SO_{4(out)}^{2-} \underset{2}{\overset{1}{\rightleftarrows}} \left(SO_{4(in)}^{2-} \underset{5a}{\overset{4a}{\rightleftarrows}} APS \underset{5b}{\overset{4b}{\rightleftarrows}} SO_3^{2-} \underset{7}{\overset{6}{\rightleftarrows}} S_{int} \underset{9}{\overset{8}{\rightleftarrows}} H_2S_{(in)} \right) \overset{3}{\rightarrow} H_2S_{(out)} \qquad (13)$$

Johnston et al. (*2007*) optimized this model and summarized the sulfur fractionation for each step. Those fractionations are (1) +3‰ when sulfate moves across the cellular membrane ($^{34}\alpha_1$), (2) 0‰ when sulfate is incorporated into adenosine 5′ phosphosulfate (APS) ($^{34}\alpha_{4a}$), (3) -25‰ when APS is reduced to sulfite ($^{34}\alpha_{4b}$), (4) -53‰ when sulfite is reduced to intermediate sulfur species (S_2O_3, S_3O_6) ($^{34}\alpha_6$), and $^{34}\alpha_7 = 1.005$ in the reserved process, (5) -25‰ when sulfite is reduced to hydrogen sulfide ($^{34}\alpha_3$). This sulfur flow network can produce an ^{34}S fractionation up to ~75‰ between the original sulfate and the final sulfide product, much higher than the previously estimated value of ~47‰ (*Rees, 1973*). Here, f_3 is used to expressed the ratio of the amount of cellular outputs (sulfate and sulfide) relative to that of sulfate entering the cell of sulfate-reducing bacteria, and f_5 is the ratio of the amount of back reacting sulfate from the cell relative to the total amount of sulfate entering the cell, both of which vary from 0 to 1. In the network model that adopts the structure of equation (13) modified by Johnston et al. (*2007*), it appears that lower temperature (0°C) produces much higher sulfur fractionation values and $\Delta^{33}S$ values.

As the *in-situ* borehole water temperature measurements are all higher than 25°C in this study, we choose 20°C as the model temperature limit of BSR effect on $\Delta^{33}S_{sulfate}$, as plotted on Fig. 30, where f_3 and f_5 vary from 0 to 1 with the interval of 0.1. Compared with the predicted BSR effect, two features appear in our samples. Firstly, the samples from Driefontein, Tau Tona and Kloof plot relatively close to but not exactly on the predicted values. This suggests that, although the dissolved sulfide in these samples can be genetically linked to the dissolved sulfate in general,

BSR cannot fully explain all the data, implying there are some other factors need to be discovered. Some possibilities include, but are not limited to, TSR and addition of small amounts of external sulfide or sulfate sources with different $\Delta^{33}S$ values. The latter can be inferred from the Beatrix samples (see below). Secondly, the Beatrix samples spread from far way to close to the BSR range, and finally deviate again (Fig. 30). The sulfur isotopic signatures of most of the Beatrix samples cannot be explained by BSR only.

A closer look at the $\delta^{34}S$ and $\Delta^{33}S$ values of the sulfate-sulfide couple in individual water samples also clearly show the difference between Beatrix and the other mines (Fig. 17-20). Sulfide in the water samples from Driefontein, Kloof and Tau Tona all have $\Delta^{33}S$ values similar to (with sulfide $\Delta^{33}S$ values slightly higher) but $\delta^{34}S$ values smaller than their coexisting dissolved sulfate, which is consistent with the directions of BSR-induced sulfur isotope fractionations. Fracture-water ecosystems dominated by sulfate reducing bacteria are also supported by DNA investigations (*Takai et al., 2001; Moser et al., 2005; Pfiffner et al., 2006; Gihring et al., 2006*).

Beatrix samples show a large range in both $\delta^{34}S$ and $\Delta^{33}S$ values between coexisting sulfate and sulfide, and the values have shifted with time (Fig. 20). A series of fracture water samples have been collected from Beatrix Shaft 3 Level 26 borehole No. 2 since Jan. 2011. The results show that sulfide had higher $\delta^{34}S$ and $\Delta^{33}S$ values than sulfate from Jan. 2011 to Jul. 2012. With time, the dissolved sulfate shows a general trend of increasing $\delta^{34}S$ and decreasing in $\Delta^{33}S$ values from 2012 to 2013. These isotopic variations of dissolved sulfate are coupled with a general trend of decreasing $\delta^{34}S$ and increase in $\Delta^{33}S$ values in coexisting dissolved sulfide. These features indicate that: (1) the sulfide in the Beatrix fracture waters are from two difference sources, and (2) microbial processes, including both sulfide oxidation and sulfate reduction, controlled the sulfur cycle in the Beatrix fracture waters with bacterial sulfur oxidation (BSO) exceeding BSR. Indeed,

DNA investigations on one microbial sample collected in 2012 from the same borehole revealed a unique microbial ecosystem in which the sulfur cycle was controlled by sulfide-oxidizing bacteria (Lau et al., submitted). A major shift occurred between Jul. 2012 and Aug. 2013, a time interval over which time the fracture water became characterized by lower $\delta^{34}S$ and higher $\Delta^{33}S$ values in dissolved sulfide. On Johnston et al.'s (2007) diagram (Fig. 30), the 2013 Beatrix samples have moved very close to the predicted BSR range, indicating that the sulfate-reducing bacteria overwhelmed the sulfide-oxidizing bacteria in the Beatrix subsurface ecosystem. The driving force for the ecological shift in the subsurface is not yet understood. The ongoing molecular and genomic investigations undertaken by the Princeton group and the analysis of total organic carbon in the fracture waters are expected to provide more insights in the future work. Nevertheless, it is fascinating and enlightening to see how fast an ecosystem can be shifted and consequently impact the sulfur cycle in the subsurface fracture systems.

The results in this study also show that combined $\delta^{34}S$ and $\Delta^{33}S$ indices are very sensitive to BSR and other potential processes that could occur in the deep subsurface fracture water systems. Given that molecular and genomic techniques are difficult to apply for microbial detection due to the decreased biomass with depth in the crust and that employing $\delta^{34}S$ values by themselves to infer BSR becomes problematic at depth because of the greater efficiency of TSR at elevated temperature, we propose that an integrated $\delta^{34}S$ and $\Delta^{33}S$ examination has the potential to distinguish between different processes and can be used for detecting the lower limit of the habitat for deep subsurface microbial ecosystems in the continental crust.

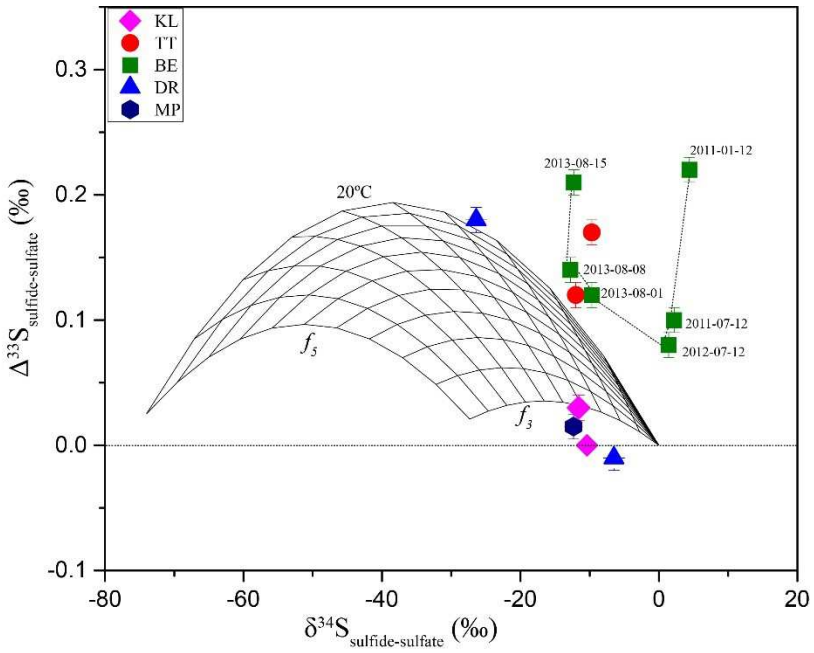

Figure 30. Comparison of δ34S and Δ33S values between coexisting dissolved sulfate and sulfide. Solid squares represent the fracture water samples (error bars are much smaller than the symbol size). The solid lines represent the predicted range by bacterial sulfate reduction at a variety of temperatures based on the Johnston's model (Johnston et al. 2007). See text for discussion.

7. Conclusion

Combined multiple sulfur isotopes and oxygen isotope analyses of 20 fracture water samples from 6 gold mines in the Witwatersrand Basin suggest that the dissolved sulfate supporting the terrestrial subsurface ecosystem is mostly derived from *in-situ* oxidation of sulfide minerals in the wall rocks rather than inherited from ancient water sources. In shallow, aerobic fracture systems, the sulfide oxidation is likely controlled by oxidative weathering of sulfide minerals, either biotically or abiotically, whereas the sulfide oxidation in deep anaerobic fracture water may contain a significant contribution from radiolytic oxidation of sulfide. This geologically driven *in-situ* sulfate production process provides an important mechanism for supplying a steady energy source to support the microbial ecosystems in long-term isolated subsurface water systems.

The comparison of multiple sulfur isotope compositions between co-existing dissolved sulfide and sulfate suggests that, although an independent sulfide source could supply dissolved sulfide to the fracture waters, the majority of sulfide in most of the fracture waters comes from bacterial sulfate reduction, which is consistent with previous observations that sulfate-reducing bacteria are widespread in the subsurface fracture waters in the Witwatersrand Basin. The multiple sulfur isotope data also illustrate a particularly interesting ecological shift from a sulfide-oxidizing bacteria to a sulfate-reducing bacteria dominated system in Beatrix fracture water, which occurred over a very short time period of less than one year.

In summary, as the oxidation mechanism for the deep high temperature fracture waters are not well constrained so far due to the limited sample availability and the ambiguity of the data. In the future, more efforts should be put to reach more deep samples to better understand these higher temperature, older fracture water systems. The data in this study also show that the microbial

processes in the subsurface fracture waters are dominated by sulfate reduction, consistent with the geomicrobiological studies. However, the data also reveal some complicated processes (e.g., in the Beatrix samples) with abrupt ecological changes. While genomic investigations will be definitely needed to confirm these geochemical observations, some detailed geochemical studies in the future can also improve our understanding of the sulfur cycle in such complicated systems. These include: (1) a continuous monitoring of multiple sulfur isotope compositions on dissolved sulfate and sulfide in the Beatrix borehole to detect the ecological shift or stabilization along time; (2) multiple sulfur isotope analysis of proteins in the sulfate reducers or sulfide oxidizers to constrain their nutrient sources and microbial interaction in the system; (3) multiple sulfur study on sulfite — the Beatrix water samples contain a significant amount of sulfite (0.05mM), which could be an intermediate product of sulfide oxidation or sulfate reduction or a mixing of both. If a reliable extraction technique can be developed in the future, the analysis of multiple sulfur isotope compositions of sulfite can give very useful information adding to sulfate and sulfide to understand the microbial processes in the system.

Table 1. Isotopic information of fracture water from each mine

	H_2O*		Sulfate					Sulfide			
Sample Name	**$\delta^{18}O$***	**$\delta^{2}H$***	**$\delta^{34}S$**	**$\delta^{18}O$**	**$\Delta^{33}S$**	**$\Delta^{36}S$**	**$\Delta^{18}O_{Sulfate-H2O}$**	**$\delta^{34}S$**	**$\Delta^{33}S$**	**$\Delta^{36}S$**	**$\Delta^{34}S_{sulfate-sulfide}$**
KL445FW190711	-9.1	-30.3	19.5 [a]	10.1	-0.02 [a]	0.7 [a]	18.4	7.8	0.01	1.7	11.7
KL445FW190711[†]			19.4		0.01	-0.2		7.9	0.04	-0.2	11.5
KL445FW280711[†]	-9.4	-31.8	19.0	9.1	0.01	-0.1	18.5	8.6	0.10	-0.1	10.4
TT107FW110811[†]	-4.8	-24.4	3.3	10.9	0.35	-0.4	15.7	-6.4	0.52	0.0	9.7
TT107FW240811	-5.1	-22.4	5.5	10.9	0.34	0.1	16.0	-2.1 [a]	0.20 [a]	b.d.l	7.6
TT109FW190112	-4.9	-23.2	n.m.	10.1	n.m.	n.m.	15.0	n.m.	n.m.	n.m.	
TT109FW090212[†]	-5.0	-25.3	5.3	10.6	0.36	-0.5	15.6	-6.7	0.48	-0.1	12.0
TT118FW080212	-5.2	-31.3	n.m.	0.2	n.m.	n.m.		n.m.	n.m.	n.m.	
DR5IPC150711	-4.3	-24.6	n.m.	6.9	n.m.	n.m.	11.2	n.m.	n.m.	n.m.	
DR5IPC280711[†]	n.m.	n.m.	1.2	6.3	0.47	-0.4		-5.3	0.46	-0.3	6.5
DR9IPC200112[†]	-4.1	-19.8	-5.3	4.5	0.50	-0.5	8.6	-31.7	0.68	-0.4	26.4
BE326BH1FW210111[†]	-6.6	-41.7	9.1	2.0	-0.17	-0.2	8.6	7.9	0.13	-0.1	1.2
BE326BH2FW210111[†]	-5.9	-41.0	4.1	5.9	-0.08	-0.2	11.8	8.5	0.14	-0.2	-4.4
BE326BH2FW120711[†]	-6.4	-41.4	6.2	2.7	-0.08	-0.2	9.1	8.4	0.02	-0.1	-2.2
BE326BH2FW120712	-8.7	-47.0	4.5	3.5	-0.05	-0.1	12.2	5.9	0.03	0.0	-1.4
BE326BH1FW200912	n.m.	n.m.	4.3	0.6	-0.07	0.0		13.7	-0.03.	0.1	-9.4
BE326BH2FW010813	n.m.	n.m.	6.5	2.2	-0.10	0.1		-3.2	0.02	-3.0	9.7
BE326BH2FW080813	n.m.	n.m.	8.2	3.1	-0.09	0.2		-4.6	0.05	-0.7	12.8
BE326BH2FW150813	n.m.	n.m.	8.6	2.1	-0.11	0.4		-3.7	0.10	-0.8	12.3
JO129FW250412	-7.2	-42.2	3.5	-1.1	-0.12	0.0	6.1	b.d.l.	b.d.l.	b.d.l.	
MM546FW290612	n.m.	n.m.	11.3	b.d.l	-0.13	-1.6		8.3 [a]	b.d.l	b.d.l	3.0

Sample Name was express as "Gold Mine + Shaft NO. + Level NO. + Water Sample Type + Collection Date (DD.MM.YY.)".

£ Fracture water geochemistry information was measured in the Princeton University.

* Water isotope information was analyzed in the University of Waterloo.

† Multiple sulfur isotope information was analyzed in the McGill University.

[a] Multiple sulfur isotopes were measured at Micro-volume mode, not analyzed in the text.

n.m. = not measured.

b.d.l. = below detection limit.

Table 2. Isotopic composition and calculated contents of sulfate concentration of the Transvaal dolomites in Driefontein gold mine.

	Sulfate conc. (wt%)		**Sulfate**				**Indissoluble Remnant**		
Sample Name	**calculation**	**EPMA**	**$\delta^{18}O$**	**$\delta^{34}S$**	**$\Delta^{33}S$**	**$\Delta^{36}S$**	**$\delta^{34}S$**	**$\Delta^{33}S$**	**$\Delta^{36}S$**
DR-IPC5-01	0.0066%			39.2	0.16	1.9			
DR-IPC5-02	0.0057%			31.4	0.14	3.4	2.3[a]	2.66[a]	-2.1[a]
DR-IPC5-03	0.0087%	0.0050%		36.2	0.08	-2.1			
DR-IPC5-04	0.0063%	0.0168%		35.3	0.07	2.6			
DR-IPC5-05	0.0049%			34.1	-0.01	3.0			

Table 3. EPMA data of element and sulfate average concentration of the Transvaal dolomites in Driefontein gold mine.

		FeO (wt.%)	MnO (wt.%)	MgO (wt.%)	CaO (wt.%)	SrO (wt.%)	Na_2O (wt.%)	SO_3 (wt.%)	CO_2 (wt.%)	TOTAL (wt.%)
DR-IPC5-03	Traverse No.1	0.851	1.059	20.259	29.842	0.000	0.004	0.0047	46.720	98.740
	Traverse No.2	1.009	1.103	20.040	29.696	0.000	0.004	0.0052	46.490	98.347
DR-IPC5-04	Traverse No.1	0.447	0.879	20.317	29.980	0.000	0.006	0.0168	46.528	98.175

Table 4. SEM data of atomic composition of sulfate precipitation extracted from fracture waters.

Sample Name	O (at.%)	Na (at.%)	Al (at.%)	Si (at.%)	S (at.%)	Cl (at.%)	Ba (at.%)
KL445FW190711	63.49				16.55	1.11	18.85
KL445FW280711	72.79	0.82	0.64	0.07	11.53	0.76	13.40
TT107FW081111	71.93		0.43	0.05	12.37	0.80	14.41
TT107FW240811	67.27	0.66	0.22		14.56	0.59	16.70
TT109FW190112	73.32		0.98	0.12	11.31	0.41	13.87
TT109FW090212	72.90			0.11	12.03	0.36	14.59
TT118FW080212	73.20				12.45	0.40	13.96
DR5IPC150711	72.94			0.05	12.56	0.30	14.15
DR5IPC280711	72.49		0.21	0.08	12.07	0.38	14.77
DR9IPC200112	71.33			0.05	12.46	0.52	15.64
BE326BH2FW120712	67.47			0.13	14.81	1.07	16.52
BE326BH1FW200912	72.00			0.10	12.74	0.67	14.48
BE326BH2FW010813	65.38			0.09	15.59	1.03	17.91
BE326BH2FW080813	70.33			0.12	13.31	0.92	15.32
BE326BH2FW150813	66.85				15.23	0.94	16.97
JO129FW042512	64.64			0.09	15.70	0.78	18.78

Table 5. Calculated residence time and oxygen isotope exchange equilibrium time of fracture waters.

Sample Name	$Br^{£}$ (ppm)	Age (Ma)	Equilibrium at pH=7 (kyr)	Equilibrium at pH=9 (kyr)	Sample Name	$Br^{£}$ (ppm)	Age (Ma)	Equilibrium at pH=7 (kyr)	Equilibrium at pH=9 (kyr)
KL445FW190711	35	109.15	2.85	57.12	BE326BH1FW210111	11.03	53.15	10.90	211.62
KL445FW280711	n.m.		n.m.	n.m.	BE326BH2FW210111	13.26	58.37	7.84	153.42
TT107FW110811	0.45	28.44	3.23	64.65	BE326BH2FW120711	11.67	54.64	9.03	176.16
TT107FW240811	n.m.		3.56	70.92	BE326BH2FW120712	8.79	47.92	7.29	142.86
TT109FW190112	n.m.		4.19	83.25	BE326BH1FW200912	n.m.		10.17	197.77
TT109FW090212	0.55	28.68	3.92	77.88	BE326BH2FW010813	11.91	55.20	9.26	180.48
TT118FW080212	2.38	32.95	3.35	66.79	BE326BH2FW080813	12.39	56.32	8.39	163.86
DR5IPC150711	0.21	27.88	14.84	285.96	BE326BH2FW150813	12.86	57.44	8.65	168.86
DR5IPC280711	n.m.		n.m.	n.m.	JO129FW250412	23.89	83.20	6.54	128.50
DR9IPC200112	0.09	27.60	6.23	122.64	MM546FW290612	12.78	57.25	17.84	342.39

References

Armstrong, John T., 1995. Citzaf-a package of correction programs for the quantitative Electron Microbeam X-Ray-Analysis of thick polished materials, thin-films, and particles. Microbeam Analysis 4.3, 177-200.

Armstrong, R., Compston, W., Retief, E., Williams, I.t., Welke, H., 1991. Zircon ion microprobe studies bearing on the age and evolution of the Witwatersrand triad. Precambrian Research 53, 243-266.

Baker, B.J., Moser, D.P., MacGregor, B.J., Fishbain, S., Wagner, M., Fry, N.K., Jackson, B., Speolstra, N., Loos, S., Takai, K., 2003. Related assemblages of sulphate-reducing bacteria associated with ultradeep gold mines of South Africa and deep basalt aquifers of Washington State. Environmental Microbiology 5, 267-277.

Balci, N., Mayer, B., Shanks, W.C., Mandernack, K.W., 2012. Oxygen and sulfur isotope systematics of sulfate produced during abiotic and bacterial oxidation of sphalerite and elemental sulfur. Geochimica et Cosmochimica Acta 77, 335-351.

Balci, N., Shanks, W.C., Mayer, B., Mandernack, K.W., 2007. Oxygen and sulfur isotope systematics of sulfate produced by bacterial and abiotic oxidation of pyrite. Geochimica et Cosmochimica Acta 71, 3796-3811.

Beach, A., Smith, R., 2007. Structural geometry and development of the Witwatersrand Basin, South Africa. Geological Society, London, Special Publications 272, 533-542.

Blount, C.W., Dickson, F.W., 1973. Gypsum-anhydrite equilibria in systems $CaSO_4$-H_2O and $CaSO_4$-NaCl-H_2O. American Mineralogist 58, 323-331.

Boice, A.E., 2004. Sulfur Isotopic Evidence of Microbial Activity During Deposition of a Neoarchean Shale and in Modern Deep Groundwater. PhD thesis,Witwatersrand Basin, South Africa. Indiana University.

Boschetti, T., 2013. Oxygen isotope equilibrium in sulfate–water systems: A revision of geothermometric applications in low-enthalpy systems. Journal of Geochemical Exploration 124, 92-100.

Bowers, T. S. and H. P. Taylor, JR., 1985. An integrated chemical and stable-isotope model of the origin of midocean ridge hot spring system. Journal of Geophysical Research 90, 12,583-12,606.

Brunner, B., Yu, J.-Y., Mielke, R.E., MacAskill, J.A., Madzunkov, S., McGenity, T.J., Coleman, M., 2008. Different isotope and chemical patterns of pyrite oxidation related to lag and exponential growth phases of Acidithiobacillus ferrooxidans reveal a microbial growth strategy. Earth and Planetary Science Letters 270, 63-72.

Burdett, J.W., Arthur, M.A., Richardson, M., 1989. A Neogene seawater sulfur isotope age curve from calcareous pelagic microfossils. Earth and Planetary Science Letters 94, 189-198.

Cameron, E., 1982. Sulphate and sulphate reduction in early Precambrian oceans.

Canfield, D.E., Farquhar, J., 2009. Animal evolution, bioturbation, and the sulfate concentration of the oceans. Proceedings of the National Academy of Sciences 106, 8123-8127.

Carpenter, A.B., 1978. Origin and chemical evolution of brines in sedimentary basins, SPE Annual Fall Technical Conference and Exhibition. Society of Petroleum Engineers.

Chivian, D., Brodie, E.L., Alm, E.J., Culley, D.E., Dehal, P.S., DeSantis, T.Z., Gihring, T.M., Lapidus, A., Lin, L.-H., Lowry, S.R., 2008. Environmental genomics reveals a single-species ecosystem deep within Earth. Science 322, 275-278.

Coward, M.P., Spencer, R.M., Spencer, C.E., 1995. Development of the Witwatersrand Basin, South Africa. Geological Society, London, Special Publications 95, 243-269.

Craig, H., 1961. Isotopic variations in meteoric waters. Science 133, 1702-1703.

Crowe, S.A., Paris, G., Katsev, S., Jones, C., Kim, S.-T., Zerkle, A.L., Nomosatryo, S., Fowle, D.A., Adkins, J.F., Sessions, A.L., 2014. Sulfate was a trace constituent of Archean seawater. Science 346, 735-739.

Dankert, B.T., Hein, K.A., 2010. Evaluating the structural character and tectonic history of the Witwatersrand Basin. Precambrian Research 177, 1-22.

Donovan, J. J., D. Kremser, J. H. Fournelle, 2012. Probe for EPMA: acquisition, automation and analysis. Probe Software, Inc., Eugene, Oregon.

Duane, M., Pigozzi, G., Harris, C., 1997. Geochemistry of some deep gold mine waters from the western portion of the Witwatersrand Basin, South Africa. Journal of African Earth Sciences 24, 105-123.

Duncan, A., Marsh, J., 2006. The Karoo igneous province. The geology of South Africa, 501-520.

Duncan, A.R., 1987. The Karoo igneous province—a problem area for inferring tectonic setting from basalt geochemistry. Journal of Volcanology and Geothermal Research 32, 13-34.

England, G.L., Rasmussen, B., Krapez, B., Groves, D.I., 2002. Palaeoenvironmental significance of rounded pyrite in siliciclastic sequences of the Late Archaean Witwatersrand Basin: oxygen-deficient atmosphere or hydrothermal alteration? Sedimentology 49, 1133-1156.

Farquhar, J., Bao, H., Thiemens, M., 2000a. Atmospheric influence of Earth's earliest sulfur cycle. Science 289, 756-758.

Farquhar, J., Savarino, J., Airieau, S., Thiemens, M.H., 2001. Observation of wavelength-sensitive mass-independent sulfur isotope effects during SO_2 photolysis: Implications for the early atmosphere. Journal of Geophysical Research: Planets 106, 32829-32839.

Farquhar, J., Savarino, J., Jackson, T.L., Thiemens, M.H., 2000b. Evidence of atmospheric sulphur in the martian regolith from sulphur isotopes in meteorites. Nature 404, 50-52.

Farquhar, J., Wing, B.A., 2003. Multiple sulfur isotopes and the evolution of the atmosphere. Earth and Planetary Science Letters 213, 1-13.

Ferguson, J., 1973. The Pilanesberg alkaline province, southern Africa. Trans. Geol. Soc. S. Afr 76, 249-270.

Frape, S., Fritz, P., McNutt, R.t., 1984. Water-rock interaction and chemistry of groundwaters from the Canadian Shield. Geochimica et Cosmochimica Acta 48, 1617-1627.

Fritz, P., Basharmal, G., Drimmie, R., Ibsen, J., Qureshi, R., 1989. Oxygen isotope exchange between sulphate and water during bacterial reduction of sulphate. Chemical Geology: Isotope Geoscience Section 79, 99-105.

Garrels, R., Thompson, M., 1960. Oxidation of pyrite by iron sulfate solutions. American Journal of Science 258, 57-67.

Garrett, B.C., et al., 2005. Role of water in electron-initiated processes and radicalchemistry: issues and scientific advances. Chem. Rev. 105, 355–390.

Gihring, T., Moser, D., Lin, L.-H., Davidson, M., Onstott, T., Morgan, L., Milleson, M., Kieft, T., Trimarco, E., Balkwill, D., 2006. The distribution of microbial taxa in the subsurface water of the Kalahari Shield, South Africa. Geomicrobiology Journal 23, 415-430.

Guy, B., Ono, S., Gutzmer, J., Kaufman, A., Lin, Y., Fogel, M., Beukes, N., 2012. A multiple sulfur and organic carbon isotope record from non-conglomeratic sedimentary rocks of the Mesoarchean Witwatersrand Supergroup, South Africa. Precambrian Research 216, 208-231.

Habicht, K.S., Gade, M., Thamdrup, B., Berg, P., Canfield, D.E., 2002. Calibration of sulfate levels in the Archean ocean. Science 298, 2372-2374.

Halas, S., Pluta, I., 2000. Empirical calibration of isotope thermometer of $\delta^{18}O$ (SO_4^{2-})-$\delta^{18}O$ (H_2O) for low temperature brines.

Harrison, A., Thode, H., 1958. Mechanism of the bacterial reduction of sulphate from isotope fractionation studies. Transactions of the Faraday Society 54, 84-92.

Heidel, C., Tichomirowa, M., 2010. The role of dissolved molecular oxygen in abiotic pyrite oxidation under acid pH conditions–Experiments with ^{18}O-enriched molecular oxygen. Applied Geochemistry 25, 1664-1675.

Heidel, C., Tichomirowa, M., 2011. The isotopic composition of sulfate from anaerobic and low oxygen pyrite oxidation experiments with ferric iron—New insights into oxidation mechanisms. Chemical Geology 281, 305-316.

Hofmann, A., Bekker, A., Rouxel, O., Rumble, D., Master, S., 2009. Multiple sulphur and iron isotope composition of detrital pyrite in Archaean sedimentary rocks: a new tool for provenance analysis. Earth and Planetary Science Letters 286, 436-445.

Holland, G., Lollar, B.S., Li, L., Lacrampe-Couloume, G., Slater, G., Ballentine, C., 2013. Deep fracture fluids isolated in the crust since the Precambrian era. Nature 497, 357-360.

Holland, H., 1994. Early Proterozoic atmospheric change. Early life on Earth, 237-244.

Huston, D.L., Logan, G.A., 2004. Barite, BIFs and bugs: evidence for the evolution of the Earth's early hydrosphere. Earth and Planetary Science Letters 220, 41-55.

Jamieson, J., Wing, B., Farquhar, J., Hannington, M., 2013. Neoarchaean seawater sulphate concentrations from sulphur isotopes in massive sulphide ore. Nature Geoscience 6, 61-64.

Johnson, M., Van Vuuren, C., Hegenberger, W., Key, R., Show, U., 1996. Stratigraphy of the Karoo Supergroup in southern Africa: an overview. Journal of African Earth Sciences 23, 3-15.

Johnston, D.T., 2011. Multiple sulfur isotopes and the evolution of Earth's surface sulfur cycle. Earth-Science Reviews 106, 161-183.

Johnston, D.T., Farquhar, J., Canfield, D.E., 2007. Sulfur isotope insights into microbial sulfate reduction: when microbes meet models. Geochimica et Cosmochimica Acta 71, 3929-3947.

Johnston, D.T., Farquhar, J., Wing, B.A., Kaufman, A.J., Canfield, D.E., Habicht, K.S., 2005. Multiple sulfur isotope fractionations in biological systems: a case study with sulfate reducers and sulfur disproportionators. American Journal of Science 305, 645-660.

Jones, M., 1988. Heat flow in the Witwatersrand Basin and environs and its significance for the South African shield geotherm and lithosphere thickness. Journal of Geophysical Research: Solid Earth 93, 3243-3260.

Kampschulte, A., Bruckschen, P., Strauss, H., 2001. The sulphur isotopic composition of trace sulphates in Carboniferous brachiopods: implications for coeval seawater, correlation with other geochemical cycles and isotope stratigraphy. Chemical Geology 175, 149-173.

Katz, A., Starinsky, A., Marion, G.M., 2011. Saline waters in basement rocks of the Kaapvaal Craton, South Africa. Chemical Geology 289, 163-170.

Kieft, T.L., McCuddy, S.M., Onstott, T., Davidson, M., Lin, L.-H., Mislowack, B., Pratt, L., Boice, E., Lollar, B.S., Lippmann-Pipke, J., 2005. Geochemically generated, energy-rich substrates and indigenous microorganisms in deep, ancient groundwater. Geomicrobiology Journal 22, 325-335.

Kloppmann, W., Girard, J.-P., Négrel, P., 2002. Exotic stable isotope compositions of saline waters and brines from the crystalline basement. Chemical Geology 184, 49-70.

Kornexl, B.E., Gehre, M., Hofling, R., Werner, R.A., 1999. On-line $\delta^{18}O$ measurement of organic and inorganic substances. Rapid Communications in Mass Spectrometry 13, 1685-1693.

Kroopnick, P., Craig, H., 1972. Atmospheric oxygen: isotopic composition and solubility fractionation. Science 175, 54-55.

Krouse, H. R. Oxygen Isotope Composition Produced during Bacterial Oxidaton of MetalSulphides: Dependence upon O_2 Pressure and Oxygen Isotope Compositions of H_2O and O_2. Report, Energy, Mines and Resources Canada, Ottawa, Canada, Contract File 55SS.23440-8-9161, 1989.

Kump, L.R., 2008. The rise of atmospheric oxygen. Nature 451, 277-278.

Le Caer, S., 2011. Water Radiolysis: Influence of Oxide Surfaces on H2 Production under Ionizing Radiation. Water 3, 235-253.

Lefticariu, L., Pratt, L.A., LaVerne, J.A., Schimmelmann, A., 2010. Anoxic pyrite oxidation by water radiolysis products—A potential source of biosustaining energy. Earth and Planetary Science Letters 292, 57-67.

Li, L., Wing, B.A., Bui, T.H., McDermott, J.M., Slater, G.F., Wei, S.W., Lacrampe-Couloume, G., Sherwood Lollar, B., 2016. Mass-independent sulfur fractionation in subsurface fracture waters indicates a long-standing sulfur cycle in Precambrian rocks. Nature Communications, Accepted.

Liebenberg, W., 1955. The occurrence and origin of gold and radioactive minerals in the Witwatersrand System, the Dominion Reef, the Ventersdorp Contact Reef and the Black Reef. Hortors.

Lin, L.-H., Slater, G.F., Lollar, B.S., Lacrampe-Couloume, G., Onstott, T., 2005a. The yield and isotopic composition of radiolytic H_2, a potential energy source for the deep subsurface biosphere. Geochimica et Cosmochimica Acta 69, 893-903.

Lin, L.H., Hall, J., Lippmann-Pipke, J., Ward, J.A., Sherwood Lollar, B., DeFlaun, M., Rothmel, R., Moser, D., Gihring, T.M., Mislowack, B., 2005b. Radiolytic H_2 in continental crust: nuclear power for deep subsurface microbial communities. Geochemistry, Geophysics, Geosystems 6.

Lin, L.-H., Wang, P.-L., Lippmann-Pipke, J., Boice, E., Pratt, L.M., Sherwood Lollar, B., Brodie, E.L., Hazen, T.C., Andersen, G.L., DeSantis, T.Z., Moser, D., Kershaw, D., Onstott, T.C., 2006. Long-term sustainability of a high-energy, low-diversity crustal biome. Science 314, 479-482.

Lippmann, J., Lollar, B.S., Niedermann, S., Stroncik, N.A., Naumann, R., van Heerden, E., Onstott, T.C., 2011. Neon identifies two billion year old fluid component in Kaapvaal Craton. Chemical Geology 283, 287-296.

Lippmann, J., Stute, M., Torgersen, T., Moser, D., Hall, J., Lin, L., Borcsik, M., Bellamy, R., Onstott, T., 2003. Dating ultra-deep mine waters with noble gases and ^{36}Cl, Witwatersrand Basin, South Africa. Geochimica et Cosmochimica Acta 67, 4597-4619.

Litthauer, A., 2009. The geochemistry of the dykes in the Carletonville Goldfield. Free State.

Lloyd, R., 1968. Oxygen isotope behavior in the sulfate-water system. Journal of Geophysical Research 73, 6099-6110.

Llyod, R.M., 1967. Oxygen-18 composition of oceanic sulfate. Science 156, 1228-1231.

Madgin, W.M., Swales, D.A., 1956. Solubilities in the system $CaSO_4$-NaCl-H_2O at 25° and 35°. Journal of Applied Chemistry 6, 482-487.

Manzi, M.S., Hein, K.A., King, N., Durrheim, R.J., 2013. Neoarchaean tectonic history of the Witwatersrand Basin and Ventersdorp Supergroup: New constraints from high-resolution 3D seismic reflection data. Tectonophysics 590, 94-105.

Martin, D.M., Clendenin, C., Krapez, B., McNaughton, N., 1998. Tectonic and geochronological constraints on late Archaean and Palaeoproterozoic stratigraphic correlation within and between the Kaapvaal and Pilbara Cratons. Journal of the Geological Society 155, 311-322.

Mazor, E., Verhagen, B.T., 1983. Dissolved ions, stable and radioactive isotopes and noble gases in thermal waters of South Africa. Journal of Hydrology 63, 315-329.

Mizutani, Y., Rafter, T., 1969. Oxygen isotopic composition of sulfate. Part 3. Oxygen isotopic fractionation in the bisulfate ion--water system. Inst. of Nuclear Sciences, Lower Hutt, NZ.

Moser, D.P., Gihring, T.M., Brockman, F.J., Fredrickson, J.K., Balkwill, D.L., Dollhopf, M.E., Lollar, B.S., Pratt, L.M., Boice, E., Southam, G., 2005. Desulfotomaculum and Methanobacterium spp. dominate a 4-to 5-kilometer-deep fault. Applied and Environmental Microbiology 71, 8773-8783.

Moser, D.P., Onstott, T., Fredrickson, J.K., Brockman, F.J., Balkwill, D.L., Drake, G., Pfiffner, S., White, D., Takai, K., Pratt, L., 2003. Temporal shifts in the geochemistry and microbial community structure of an ultradeep mine borehole following isolation. Geomicrobiology Journal 20, 517-548.

Nelson, D., Trendall, A., Altermann, W., 1999. Chronological correlations between the Pilbara and Kaapvaal cratons. Precambrian Research 97, 165-189.

Ohmoto, H., Felder, R.P., 1987. Bacterial activity in the warmer, sulphate-bearing, Archaean oceans.

Omar, G., Onstott, T., Hoek, J., 2003. The origin of deep subsurface microbial communities in the Witwatersrand Basin, South Africa as deduced from apatite fission track analyses. Geofluids 3, 69-80.

Ono, S., Eigenbrode, J.L., Pavlov, A.A., Kharecha, P., Rumble, D., Kasting, J.F., Freeman, K.H., 2003. New insights into Archean sulfur cycle from mass-independent sulfur isotope records from the Hamersley Basin, Australia. Earth and Planetary Science Letters 213, 15-30.

Ono, S., Wing, B., Johnston, D., Farquhar, J., Rumble, D., 2006. Mass-dependent fractionation of quadruple stable sulfur isotope system as a new tracer of sulfur biogeochemical cycles. Geochimica et Cosmochimica Acta 70, 2238-2252.

Onstott, T., Lin, L.-H., Davidson, M., Mislowack, B., Borcsik, M., Hall, J., Slater, G., Ward, J., Lollar, B.S., Lippmann-Pipke, J., 2006. The origin and age of biogeochemical trends in deep fracture water of the Witwatersrand Basin, South Africa. Geomicrobiology Journal 23, 369-414.

Pavlov, A., Kasting, J., 2002. Mass-independent fractionation of sulfur isotopes in Archean sediments: strong evidence for an anoxic Archean atmosphere. Astrobiology 2, 27-41.

Pfiffner, S.M., Cantu, J.M., Smithgall, A., Peacock, A.D., White, D.C., Moser, D.P., Onstott, T.C., van Heerden, E., 2006. Deep subsurface microbial biomass and community structure in Witwatersrand Basin mines. Geomicrobiology Journal 23, 431-442.

Pingitore, N.E., Meitzner, G., Love, K.M., 1995. Geochimica et Cosmochimica Acta, Vol. 59, No. 12, pp. 2477-2483.

Pisapia, C., Chaussidon, M., Mustin, C., Humbert, B., 2007. O and S isotopic composition of dissolved and attached oxidation products of pyrite by Acidithiobacillus ferrooxidans: comparison with abiotic oxidations. Geochimica et Cosmochimica Acta 71, 2474-2490.

Poser, A., Vogt, C., Knöller, K., Ahlheim, J., Weiss, H., Kleinsteuber, S., Richnow, H.-H., 2014. Stable sulfur and oxygen isotope fractionation of anoxic sulfide oxidation by two diff erent enzymatic pathways. Environ. Sci. Technol. 48, 9094-9102.

Rees, C., 1973. A steady-state model for sulphur isotope fractionation in bacterial reduction processes. Geochimica et Cosmochimica Acta 37, 1141-1162.

Reinhard, C.T., Planavsky, N.J., Lyons, T.W., 2013. Long-term sedimentary recycling of rare sulphur isotope anomalies. Nature 497, 100-103.

Robb, L.J., Meyer, F.M., 1995. The Witwatersrand Basin, South Africa: geological framework and mineralization processes. Ore Geology Reviews 10, 67-94.

Schwarcz, H. P.; Cortecci, G. Chem. Geol. 1974, 13, 285-294.

Seal, R.R., 2006. Sulfur isotope geochemistry of sulfide minerals. Reviews in mineralogy and geochemistry 61, 633-677.

Sherwood Lollar, B., Lacrampe-Couloume, G., Slater, G., Ward, J., Moser, D., Gihring, T., Lin, L.-H., Onstott, T., 2006. Unravelling abiogenic and biogenic sources of methane in the Earth's deep subsurface. Chemical Geology 226, 328-339.

Sherwood Lollar, B., Onstott, T., Lacrampe-Couloume, G., Ballentine, C., 2014. The contribution of the Precambrian continental lithosphere to global H_2 production. Nature 516, 379-382.

Sherwood Lollar, B., Voglesonger, K., Lin, L.-H., Lacrampe-Couloume, G., Telling, J., Abrajano, T., Onstott, T., Pratt, L., 2007. Hydrogeologic controls on episodic H_2 release from Precambrian fractured rocks-Energy for deep subsurface life on Earth and Mars. Astrobiology 7, 971-986.

Silver, B.J., Raymond, R., Sigman, D.M., Prokopeko, M., Lollar, B.S., Lacrampe-Couloume, G., Fogel, M.L., Pratt, L.M., Lefticariu, L., Onstott, T., 2012. The origin of NO_3^- and N_2 in deep subsurface fracture water of South Africa. Chemical Geology 294, 51-62.

Sim, M.S., Bosak, T., Ono, S., 2011. Large sulfur isotope fractionation does not require disproportionation. Science 333, 74-77.

Smith, E., Svanks, K., Shumate, K., 1968. Sulfide to sulfate reaction studies. Pap, Ohio State Univ, 1968. 10 p, 5 fig, 4 tab, 12 ref, FWPCA Research Grant.

Spangenberg, J., Frimmel, H., 2001. Basin-internal derivation of hydrocarbons in the Witwatersrand Basin, South Africa: evidence from bulk and molecular $\delta^{13}C$ data. Chemical Geology 173, 339-355.

Staudt, W.J., Reeder, R.J., Schoonen, M.A., 1994. Surface structural controls on compositional zoning of SO_4^{2-} and SeO_4^{2-} in synthetic calcite single crystals. Geochimica et Cosmochimica Acta, Vol. 58, No. 9, pp. 2087-2098.

Stober, I., Bucher, K., 1999. Origin of salinity of deep groundwater in crystalline rocks. Terra Nova-Oxford 11, 181-185.

Swart, C., James, A., Kleywegt, R., Stoch, E., 2003. The future of the dolomitic springs after mine closure on the Far West Rand, Gauteng, RSA. Environmental geology 44, 751-770.

Takai, K., Moser, D.P., DeFlaun, M., Onstott, T.C., Fredrickson, J.K., 2001. Archaeal diversity in waters from deep South African gold mines. Applied and Environmental Microbiology 67, 5750-5760.

Taylor, B., Wheeler, M.C., 1994. Sulfur- and oxygen-isotope geochemistry of acid mine drainage in the Western United States: Field and experimental studies revisited, ACS Symposium Series[ACS SYMP. SER.]. 1994.

Taylor, B.E., Wheeler, M.C., Nordstrom, D.K., 1984. Stable isotope geochemistry of acid mine drainage: Experimental oxidation of pyrite. Geochimica et Cosmochimica Acta 48, 2669-2678.

Temple, K.L., Delchamps, E.W., 1953. Autotropic bacteria and the formation of acid in bituminous coal mines. Applied Microbiology 1, 255.

Thode, H., Monster, J., Dunford, H., 1961. Sulphur isotope geochemistry. Geochimica et Cosmochimica Acta 25, 159-174.

Thurston, R.S., Mandernack, K.W., Shanks, W.C., 2010. Laboratory chalcopyrite oxidation by Acidithiobacillus ferrooxidans: oxygen and sulfur isotope fractionation. Chemical Geology 269, 252-261.

Qureshi, R. M. The Isotopic Composition of Aqueous Sulfate (A laboratory investigation). Ph.D. thesis, U. of Waterloo, Waterloo, Ont., Canada, 1986.

Toran, L., Harris, R.F., 1989. Interpretation of sulfur and oxygen isotopes in biological and abiological sulfide oxidation. Geochimica et Cosmochimica Acta 53, 2341-2348.

Van der Westhuizen, W., De Bruiyn, H., Meintjes, P., 2006. The Ventersdorp Supergroup. The Geology of South Africa, 187-208.

van Everdingen, R.O., Krouse, H.R., 1985. Isotope composition of sulphates generated by bacterial and abiological oxidation.

Van Niekerk, C., 1962. The age of the Gemspost dyke from the Venterspost gold mine. Transactions of the Geological Society of South Africa 65, 105-111.

Walraven, F., Martini, J., 1995. Zircon Pb-evaporation age determinations for the Oak Tree Formation, Chuniespoort Group, Transvaal Sequence; implications for Transvaal-Griqualand West basin correlations. South African Journal of Geology 98, 58-67.

Ward, J., Slater, G., Moser, D., Lin, L.-H., Lacrampe-Couloume, G., Bonin, A., Davidson, M., Hall, J., Mislowack, B., Bellamy, R., 2004. Microbial hydrocarbon gases in the Witwatersrand Basin, South Africa: implications for the deep biosphere. Geochimica et Cosmochimica Acta 68, 3239-3250.

Watanabe, Y., Farquhar, J., Ohmoto, H., 2009. Anomalous fractionations of sulfur isotopes during thermochemical sulfate reduction. Science 324, 370-373.

Watanabe, Y., Naraoka, H., Wronkiewicz, D.J., Condie, K.C., Ohmoto, H., 1997. Carbon, nitrogen, and sulfur geochemistry of Archean and Proterozoic shales from the Kaapvaal Craton, South Africa. Geochimica et Cosmochimica Acta 61, 3441-3459.

Wilson, A.H., Versfeld, J.A., 1994. The early Archaean Nondweni greenstone belt, southern Kaapvaal Craton, South Africa, part II. Characteristics of the volcanic rocks and constraints on magma genesis. Precambrian Research 67, 277-320.

Wortmann, U.G., Bernasconi, S.M., Böttcher, M.E., 2001. Hypersulfidic deep biosphere indicates extreme sulfur isotope fractionation during single-step microbial sulfate reduction. Geology 29, 647-650.

Wortmann, U.G., Chernyavsky, B., Bernasconi, S.M., Brunner, B., Böttcher, M.E., Swart, P.K., 2007. Oxygen isotope biogeochemistry of pore water sulfate in the deep biosphere: dominance of isotope exchange reactions with ambient water during microbial sulfate reduction (ODP Site 1130). Geochimica et Cosmochimica Acta 71, 4221-4232.

Wronkiewicz, D.J., Condie, K.C., 1990. Geochemistry and mineralogy of sediments from the Ventersdorp and Transvaal Supergroups, South Africa: cratonic evolution during the early Proterozoic. Geochimica et Cosmochimica Acta 54, 343-354.

Wu, N., Farquhar, J., Strauss, H., 2014. $\delta^{34}S$ and $\Delta^{33}S$ records of Paleozoic seawater sulfate based on the analysis of carbonate associated sulfate. Earth and Planetary Science Letters 399, 44-51.

Zeebe, R.E., 2010. A new value for the stable oxygen isotope fractionation between dissolved sulfate ion and water. Geochimica et Cosmochimica Acta 74, 818-828.

Appendix

Table A1. Geochemistry of fracture water from Kloof, Tau Tona, Driefontein gold mines.

Sample Name	KL445FW 190711	KL445FW 280711	TT107FW 110811	TT107FW 240811	TT109FW 190112	TT109FW 090212	TT118FW 080212	DR5IPC 150711	DR5IPC280711	DR9IPC 200112
Rock Formation	Ventersdorp volcanics		Witwatersrand quartzite					Transvaal dolomite		
Depth(mbs)	3276	3276	3048	3048	3136	3136	3413	1046	1046	900
pH	8	n.m.	8.57	8.69	8.87	8.19	6.45	7.39	n.m.	8.8
T (°C)	54.5	n.m.	52.1	50.4	47.5	48.7	51.3	26.8	n.m.	24
Conductivity (mS/cm)	14.43	n.m.	0.53	0.5	0.49	0.47	1.74	0.52	n.m.	0.45
Salinity (ppt)	n.m.	n.m.	0.26	n.m.	n.m.	0.22	0.8	n.m.	n.m.	n.m.
Eh(mV)	-51.5	n.m.	-45.6	-132.8	373.6	-62.3	129.8	n.m.	n.m.	68.7
Cl- (M)	1.97E-01	n.m.	2.79E-03	n.m.	n.m.	3.15E-03	1.29E-02	1.39E-03	n.m.	9.14E-04
Br- (M)	4.38E-04	n.m.	5.63E-06	n.m.	n.m.	6.92E-06	2.98E-05	2.63E-06	n.m.	1.15E-06
SO_4^{2-} (M)	9.85E-05	n.m.	1.04E-04	n.m.	n.m.	1.03E-04	1.17E-03	1.38E-04	n.m.	6.40E-04
$S_2O_3^{2-}$ (M)	b.d.l.	n.m.	3.09E-06	n.m.	n.m.	b.d.l.	b.d.l.	6.39E-06	n.m.	b.d.l.
HS^- (M)	8.64E-06	n.m.	7.48E-08	n.m.	n.m.	1.94E-04	b.d.l	8.11E-07	n.m.	n.a.
NO_3^- (M)	8.12E-06	n.m.	9.52E-07	n.m.	n.m.	1.08E-07	7.16E-07	1.47E-06	n.m.	6.29E-08
NH_4^+ (M)	b.d.l.	n.m.	3.88E-06	n.m.	n.m.	2.22E-06	1.33E-05	1.94E-06	n.m.	1.39E-06
Na^+ (M)	1.24E-01	n.m.	2.51E-03	n.m.	n.m.	3.39E-03	1.45E-02	2.15E-03	n.m.	1.13E-03
K^+ (M)	1.18E-03	n.m.	3.47E-05	n.m.	n.m.	4.20E-05	1.23E-04	5.58E-05	n.m.	4.69E-05
Mg^{2+} (M)	7.68E-05	n.m.	4.14E-05	n.m.	n.m.	3.43E-05	2.06E-07	3.97E-04	n.m.	7.67E-04
Ca^{2+} (M)	2.86E-02	n.m.	2.69E-04	n.m.	n.m.	5.18E-04	2.37E-03	4.99E-04	n.m.	1.15E-03
Fe^{2+} (M)	8.95E-06	n.m.	b.d.l.	n.m.	n.m.	b.d.l.	b.d.l.	<8.95E-07	n.m.	0.00E+00
Fe^{3+} (M)	8.95E-06	n.m.	2.69E-06	n.m.	n.m.	1.07E-05	b.d.l.	<8.95E-07	n.m.	7.16E-06
TDS(mg/L)	10,122	n.m.	204	n.m.	n.m.	296	b.d.l..	188	n.m.	256

Table A2. Geochemistry information of fracture water from Beatrix, Joel and Masimong gold mines.

Sample Name	BE326FW 210111	BE326FW 210111	BE326FW 120711	BE326FW 120712	BE326FW 200912	BE326FW 010813	BE326FW 080813	BE326FW 150813	JO129FW 250412	MM546FW 290612
Rock Formation	Witwatersrand quartzite									
Borehole Number	1	2			1	2				
Depth(mbls)	1340	1339	1339	1339	1340	1339	1339	1339	1300	1900
pH	9.38	8.83	8.24	8.55	7.64	8.2	8.21	8.1	8.96	7.71
T (°C)	31.6	36.9	34.6	38.1	32.7	34.2	35.8	35.3	39.9	40.7
Conductivity (mS/cm)	8.98	9.04	7.47	7.15	n.m.	7.6	7.25	7.8	n.m.	6.75
Salinity (ppt)	n.m.	n.m.	n.m.	0.11	4.64	3.72	3.5	3.78	n.m.	0.3
Eh(mV)	-23	-101	-98	-31.6	n.m.	9.3	53.1	1.5	217	53.5
Cl- (M)	5.64E-02	6.98E-02	6.51E-02	6.15E-02	n.m.	5.61E-02	5.84E-02	5.77E-02	6.60E-02	5.50E-02
Br- (M)	1.38E-04	1.66E-04	1.46E-04	1.10E-04	n.m.	1.49E-04	1.55E-04	1.61E-04	2.99E-04	1.60E-04
SO_4^{2-} (M)	1.42E-04	1.37E-04	3.67E-04	6.23E-04	n.m.	5.31E-04	4.99E-04	4.59E-04	3.67E-04	7.03E-06
$S_2O_3^{2-}$ (M)	b.d.l.	4.91E-05	2.85E-07	b.d.l.	n.m.	b.d.l.	b.d.l.	b.d.l.	b.d.l.	b.d.l.
HS^- (M)	b.d.l.	b.d.l.	1.36E-05	b.d.l.	n.m.	9.64E-05	1.09E-04	9.54E-05	n.a.	1.13E-04
NO_3^- (M)	5.03E-07	3.71E-07	4.16E-05	5.97E-06	n.m.	5.32E-06	5.32E-06	3.71E-06	6.27E-05	9.68E-07
NH_4^+ (M)	7.82E-05	8.32E-05	b.d.l.	4.66E-05	n.m.	b.d.l.	b.d.l.	b.d.l.	b.d.l.	b.d.l.
Na^+ (M)	5.37E-02	7.80E-02	7.9E-02	4.82E-02	n.m.	8.68E-02	6.60E-02	6.99E-02	6.43E-02	4.51E-02
K^+ (M)	6.83E-04	7.29E-04	7.36E-04	8.52E-04	n.m.	4.63E-03	4.65E-03	4.68E-03	5.50E-04	4.02E-04
Mg^{2+} (M)	5.99E-05	5.60E-05	8.19E-05	2.57E-05	n.m.	3.31E-04	3.04E-04	2.94E-04	2.06E-05	9.87E-05
Ca^{2+} (M)	2.38E-03	2.87E-03	2.95E-03	3.88E-03	n.m.	3.37E-03	3.37E-03	3.37E-03	1.74E-03	1.89E-03
Fe^{2+} (M)	b.d.l.	b.d.l.	<8.95E-07	0.00E+00	n.m.	b.d.l.	b.d.l.	b.d.l.	b.d.l.	2.69E-06
Fe^{3+} (M)	b.d.l.	b.d.l.	<8.95E-07	1.79E-06	n.m.	b.d.l.	b.d.l.	b.d.l.	b.d.l.	2.69E-06
TDS(mg/L)	3243	4260	4153	3415	n.m.	4222	3824	3904	3809	2971

Table A3. Element and sulfate concentrations of the Transvaal dolomites in Driefontein gold mine.

SAMPLE	FeO (wt.%)	MnO (wt.%)	MgO (wt.%)	CaO (wt.%)	SrO (wt.%)	Na_2O (wt.%)	SO_3 (wt.%)	CO_2 (wt.%)	TOTAL (wt.%)
Dr5-IPC-03_Traverse1	0.370	0.788	20.801	29.683	b.d.l.	b.d.l.	b.d.l.	46.723	98.365
Dr5-IPC-03_Traverse1	0.649	1.179	19.960	29.628	b.d.l.	b.d.l.	b.d.l.	46.176	97.592
Dr5-IPC-03_Traverse1	0.942	1.087	19.945	30.103	b.d.l.	0.028	b.d.l.	46.675	98.780
Dr5-IPC-03_Traverse1	0.333	0.863	20.738	30.232	b.d.l.	b.d.l.	0.0162	47.102	99.284
Dr5-IPC-03_Traverse1	0.505	0.928	20.327	29.467	b.d.l.	b.d.l.	b.d.l.	46.206	97.432
Dr5-IPC-03_Traverse1	0.503	1.077	20.543	30.181	b.d.l.	b.d.l.	b.d.l.	47.094	99.398
Dr5-IPC-03_Traverse1	1.285	1.145	19.917	29.917	b.d.l.	b.d.l.	b.d.l.	46.723	98.986
Dr5-IPC-03_Traverse1	0.616	1.022	20.430	29.820	b.d.l.	b.d.l.	b.d.l.	46.722	98.609
Dr5-IPC-03_Traverse1	1.556	1.116	19.641	29.244	b.d.l.	b.d.l.	b.d.l.	46.043	97.601
Dr5-IPC-03_Traverse1	1.556	1.010	19.876	29.192	b.d.l.	b.d.l.	b.d.l.	46.192	97.825
Dr5-IPC-03_Traverse1	1.109	1.300	20.228	29.623	b.d.l.	b.d.l.	b.d.l	46.821	99.081
Dr5-IPC-03_Traverse1	1.051	0.989	19.689	29.821	0.024	b.d.l.	0.0153	46.161	97.749
Dr5-IPC-03_Traverse1	1.316	1.193	19.889	29.299	b.d.l.	b.d.l.	b.d.l.	46.258	97.955
Dr5-IPC-03_Traverse1	0.602	0.960	20.450	29.115	b.d.l.	b.d.l.	b.d.l.	46.144	97.272
Dr5-IPC-03_Traverse1	0.589	0.970	20.648	29.401	b.d.l.	b.d.l.	b.d.l.	46.582	98.190
Dr5-IPC-03_Traverse1	1.532	1.107	19.927	29.504	b.d.l.	b.d.l.	b.d.l.	46.538	98.607
Dr5-IPC-03_Traverse1	1.134	1.013	20.255	30.192	b.d.l.	b.d.l.	b.d.l.	47.135	99.729
Dr5-IPC-03_Traverse1	0.849	1.211	19.923	30.241	b.d.l.	b.d.l.	b.d.l.	46.758	98.982
Dr5-IPC-03_Traverse1	0.316	0.845	20.638	30.334	b.d.l.	b.d.l.	b.d.l.	47.059	99.192
Dr5-IPC-03_Traverse1	1.427	1.132	19.635	29.280	b.d.l.	b.d.l.	b.d.l.	45.994	97.467
Dr5-IPC-03_Traverse1	0.940	1.067	20.251	29.691	b.d.l.	b.d.l.	b.d.l.	46.653	98.603
Dr5-IPC-03_Traverse1	0.269	0.943	20.582	30.673	b.d.l.	b.d.l.	b.d.l.	47.295	99.762
Dr5-IPC-03_Traverse1	1.157	1.215	20.324	29.835	b.d.l.	b.d.l.	b.d.l.	47.069	99.600
Dr5-IPC-03_Traverse1	0.921	1.227	19.880	29.963	b.d.l.	b.d.l.	b.d.l.	46.548	98.538

Dr5-IPC-03_Traverse1	0.659	0.881	20.433	29.919	b.d.l.	b.d.l.	0.0159	46.733	98.640
Dr5-IPC-03_Traverse1	1.263	1.307	20.007	29.704	b.d.l.	b.d.l.	b.d.l.	46.743	99.025
Dr5-IPC-03_Traverse1	1.184	1.228	20.032	29.362	b.d.l.	0.033	b.d.l.	46.427	98.265
Dr5-IPC-03_Traverse1	1.607	1.120	20.005	29.621	b.d.l.	b.d.l.	b.d.l.	46.770	99.123
Dr5-IPC-03_Traverse1	0.541	1.270	20.319	29.799	b.d.l.	b.d.l.	b.d.l.	46.692	98.620
Dr5-IPC-03_Traverse1	0.407	1.154	20.536	29.772	b.d.l.	0.023	b.d.l.	46.769	98.660
Dr5-IPC-03_Traverse1	1.347	1.299	19.877	29.662	b.d.l.	b.d.l.	b.d.l.	46.614	98.799
Dr5-IPC-03_Traverse1	1.157	1.163	20.096	29.780	b.d.l.	b.d.l.	b.d.l.	46.745	98.942
Dr5-IPC-03_Traverse1	0.185	0.724	20.773	30.130	b.d.l.	b.d.l.	b.d.l.	46.891	98.703
Dr5-IPC-03_Traverse1	1.150	1.251	20.336	29.365	b.d.l.	b.d.l.	b.d.l.	46.731	98.832
Dr5-IPC-03_Traverse1	1.258	1.216	20.039	29.538	b.d.l.	b.d.l.	b.d.l.	46.588	98.639
Dr5-IPC-03_Traverse1	0.569	1.171	20.463	29.579	b.d.l.	b.d.l.	b.d.l.	46.633	98.415
Dr5-IPC-03_Traverse1	0.729	1.313	20.095	29.962	b.d.l.	b.d.l.	b.d.l.	46.718	98.817
Dr5-IPC-03_Traverse1	1.396	1.328	19.808	29.595	b.d.l.	b.d.l.	b.d.l.	46.534	98.660
Dr5-IPC-03_Traverse1	0.102	0.783	20.745	30.545	b.d.l.	0.030	b.d.l.	47.193	99.398
Dr5-IPC-03_Traverse1	0.321	1.112	20.726	30.010	b.d.l.	b.d.l.	b.d.l.	47.070	99.240
Dr5-IPC-03_Traverse1	1.323	1.185	20.262	29.561	b.d.l.	0.022	0.0230	46.872	99.248
Dr5-IPC-03_Traverse1	0.884	1.312	20.456	29.367	b.d.l.	0.029	b.d.l.	46.759	98.806
Dr5-IPC-03_Traverse1	1.229	1.383	20.264	29.826	b.d.l.	b.d.l.	0.0181	47.135	99.854
Dr5-IPC-03_Traverse1	0.744	0.941	20.661	30.109	b.d.l.	b.d.l.	b.d.l.	47.229	99.683
Dr5-IPC-03_Traverse1	0.584	1.115	20.200	29.664	b.d.l.	0.022	0.0135	46.395	97.993
Dr5-IPC-03_Traverse1	1.368	1.079	19.981	29.692	b.d.l.	b.d.l.	b.d.l.	46.628	98.748
Dr5-IPC-03_Traverse1	0.309	0.997	20.663	30.226	b.d.l.	0.032	b.d.l.	47.114	99.341
Dr5-IPC-03_Traverse1	0.287	0.841	20.922	30.418	b.d.l.	b.d.l.	0.0170	47.406	99.891
Dr5-IPC-03_Traverse1	0.574	0.884	20.502	30.256	b.d.l.	b.d.l.	0.0142	47.024	99.255
Dr5-IPC-03_Traverse1	0.370	1.047	20.095	29.571	b.d.l.	b.d.l.	0.0629	45.991	97.137
Dr5-IPC-03_Traverse1	0.523	1.031	20.526	30.188	b.d.l.	0.026	0.0458	47.057	99.396
Dr5-IPC-03_Traverse1	0.513	1.192	20.347	29.636	b.d.l.	0.027	b.d.l.	46.549	98.265
Dr5-IPC-03_Traverse1	0.826	1.050	20.197	30.270	b.d.l.	b.d.l.	b.d.l.	46.966	99.308

Dr5-IPC-03_Traverse1[b]	1.471	0.716	14.145	21.338	0.410	b.d.l.	b.d.l.	33.711	71.792
Dr5-IPC-03_Traverse1	0.475	1.057	20.497	29.777	b.d.l.	b.d.l	b.d.l	46.697	98.504
Dr5-IPC-03_Traverse1	3.337	0.935	18.313	29.497	b.d.l.	0.023	0.0321	45.768	97.904
Dr5-IPC-03_Traverse1	0.313	0.785	20.933	30.507	b.d.l.	b.d.l.	0.0130	47.470	100.020
Dr5-IPC-03_Traverse1	0.150	1.183	20.249	29.870	b.d.l.	b.d.l.	0.0139	46.370	97.834
Dr5-IPC-03_Traverse1	0.157	0.599	21.017	30.778	b.d.l.	b.d.l.	b.d.l.	47.572	100.123
Dr5-IPC-03_Traverse1	0.658	1.226	20.344	29.959	b.d.l.	b.d.l.	0.0168	46.880	99.084
Dr5-IPC-03_Traverse1	0.639	0.995	20.846	29.973	b.d.l.	b.d.l.	0.0155	47.285	99.754
Dr5-IPC-03_Traverse1	0.648	1.046	20.265	30.018	b.d.l.	b.d.l.	b.d.l.	46.732	98.708
Dr5-IPC-03_Traverse1	0.442	0.707	20.506	30.412	b.d.l.	b.d.l.	b.d.l.	46.967	99.033
Dr5-IPC-03_Traverse1	0.339	1.111	20.522	29.963	b.d.l.	b.d.l.	b.d.l.	46.820	98.754
Dr5-IPC-03_Traverse1	0.757	0.908	20.463	30.210	b.d.l.	b.d.l.	b.d.l.	47.080	99.418
Dr5-IPC-03_Traverse1	0.357	1.126	20.664	29.843	b.d.l.	b.d.l.	b.d.l.	46.902	98.892
Dr5-IPC-03_Traverse1	0.745	1.092	20.406	30.267	b.d.l.	b.d.l.	0.0132	47.161	99.683
Dr5-IPC-03_Traverse1	0.430	0.962	20.556	29.985	b.d.l.	0.023	0.0199	46.843	98.818
Dr5-IPC-03_Traverse1	1.760	1.009	19.607	29.590	b.d.l.	b.d.l.	b.d.l.	46.335	98.300
Dr5-IPC-03_Traverse1	0.474	1.046	20.411	29.747	b.d.l.	0.023	b.d.l.	46.588	98.289
Dr5-IPC-03_Traverse1	0.849	1.029	20.274	29.581	b.d.l.	b.d.l.	b.d.l.	46.511	98.244
Dr5-IPC-03_Traverse1	1.622	1.037	19.870	29.586	b.d.l.	b.d.l.	0.0136	46.545	98.673
Dr5-IPC-03_Traverse1	0.542	0.916	20.702	29.960	b.d.l.	b.d.l.	b.d.l.	47.018	99.137
Dr5-IPC-03_Traverse1	1.216	1.102	19.900	29.599	b.d.l.	0.047	b.d.l.	46.421	98.285
Dr5-IPC-03_Traverse1 [b]	0.225	1.172	19.929	29.469	b.d.l.	0.036	0.0145	45.771	96.617
Dr5-IPC-03_Traverse1	1.839	1.348	19.318	29.500	b.d.l.	b.d.l.	b.d.l.	46.208	98.214
Dr5-IPC-03_Traverse1	1.156	1.217	20.023	29.701	b.d.l.	b.d.l.	b.d.l.	46.636	98.733
Dr5-IPC-03_Traverse1	1.314	1.255	19.691	29.771	b.d.l.	b.d.l.	b.d.l.	46.449	98.481
Dr5-IPC-03_Traverse1	1.352	1.204	19.663	29.458	b.d.l.	b.d.l.	b.d.l.	46.163	97.839
Dr5-IPC-03_Traverse1	0.824	1.109	20.108	29.598	b.d.l.	b.d.l.	b.d.l.	46.378	98.017
Dr5-IPC-03_Traverse1	1.193	1.184	20.319	29.464	b.d.l.	b.d.l.	b.d.l.	46.774	98.933
Dr5-IPC-03_Traverse1	1.276	1.179	20.103	29.767	b.d.l.	b.d.l.	b.d.l.	46.824	99.148

Dr5-IPC-03_Traverse1	1.973	1.173	19.561	29.256	b.d.l	b.d.l	0.0179	46.246	98.226
Dr5-IPC-03_Traverse1	0.508	0.868	20.452	30.098	b.d.l.	b.d.l.	b.d.l.	46.802	98.728
Dr5-IPC-03_Traverse1	1.343	1.130	20.035	29.579	b.d.l.	b.d.l.	b.d.l.	46.615	98.703
Dr5-IPC-03_Traverse1	0.181	0.817	20.624	29.964	b.d.l.	b.d.l.	b.d.l.	46.653	98.238
Dr5-IPC-03_Traverse1	0.058	0.570	21.182	30.171	b.d.l.	b.d.l.	b.d.l.	47.197	99.179
Dr5-IPC-03_Traverse1	0.147	0.740	20.871	31.018	b.d.l.	b.d.l.	0.0159	47.673	100.465
Dr5-IPC-03_Traverse1	0.764	1.121	19.986	29.588	b.d.l.	b.d.l.	b.d.l.	46.207	97.665
Dr5-IPC-03_Traverse1	0.132	0.627	20.651	30.465	b.d.l.	b.d.l.	b.d.l.	46.928	98.803
Dr5-IPC-03_Traverse2	0.289	0.805	20.598	30.188	b.d.l.	b.d.l.	0.0252	46.846	98.751
Dr5-IPC-03_Traverse2 [b]	2.604	1.166	18.026	28.918	b.d.l.	b.d.l.	b.d.l.	44.697	95.410
Dr5-IPC-03_Traverse2	0.791	1.204	20.175	29.531	b.d.l	b.d.l	b.d.l.	46.438	98.139
Dr5-IPC-03_Traverse2 [b]	1.757	0.796	16.123	24.728	0.233	b.d.l.	b.d.l.	38.681	82.317
Dr5-IPC-03_Traverse2	1.783	1.030	19.414	29.444	b.d.l.	b.d.l.	b.d.l.	46.037	97.708
Dr5-IPC-03_Traverse2	2.370	1.126	19.022	29.832	b.d.l.	b.d.l.	b.d.l.	46.332	98.680
Dr5-IPC-03_Traverse2	1.664	0.927	19.805	29.425	b.d.l.	b.d.l.	b.d.l.	46.313	98.134
Dr5-IPC-03_Traverse2	1.683	1.025	19.459	29.325	b.d.l.	b.d.l.	0.0155	45.921	97.429
Dr5-IPC-03_Traverse2	1.602	1.183	19.806	29.230	b.d.l.	b.d.l.	b.d.l.	46.282	98.103
Dr5-IPC-03_Traverse2	0.442	1.014	20.217	30.077	b.d.l.	b.d.l.	0.0199	46.568	98.338
Dr5-IPC-03_Traverse2	1.535	1.035	19.758	29.772	b.d.l.	b.d.l	b.d.l.	46.522	98.623
Dr5-IPC-03_Traverse2	1.405	1.271	19.849	28.968	b.d.l.	b.d.l	b.d.l.	46.056	97.548
Dr5-IPC-03_Traverse2	0.911	1.196	19.900	30.225	b.d.l.	0.021	b.d.l.	46.766	99.021
Dr5-IPC-03_Traverse2	1.372	1.266	19.737	29.445	b.d.l	b.d.l	b.d.l.	46.286	98.107
Dr5-IPC-03_Traverse2	0.675	1.028	20.393	29.933	b.d.l.	0.026	b.d.l.	46.828	98.883
Dr5-IPC-03_Traverse2	1.332	1.296	19.918	29.458	b.d.l.	b.d.l.	b.d.l.	46.488	98.492
Dr5-IPC-03_Traverse2	0.565	1.145	20.226	29.903	b.d.l.	b.d.l	0.0138	46.602	98.454
Dr5-IPC-03_Traverse2	0.478	0.921	20.535	30.164	b.d.l.	b.d.l	b.d.l.	46.959	99.057
Dr5-IPC-03_Traverse2	1.258	0.917	19.923	29.948	b.d.l	b.d.l.	b.d.l.	46.597	98.642
Dr5-IPC-03_Traverse2	1.241	1.145	20.168	29.823	b.d.l.	b.d.l	b.d.l.	46.898	99.275
Dr5-IPC-03_Traverse2	1.452	1.201	19.834	29.336	b.d.l	b.d.l	b.d.l.	46.315	98.137

Dr5-IPC-03_Traverse2	1.594	0.946	19.607	29.585	0.022	b.d.l	b.d.l	46.200	97.953
Dr5-IPC-03_Traverse2	1.175	1.132	19.931	29.539	b.d.l.	b.d.l.	b.d.l.	46.367	98.144
Dr5-IPC-03_Traverse2	0.610	0.987	20.163	30.050	b.d.l.	b.d.l.	b.d.l.	46.585	98.394
Dr5-IPC-03_Traverse2	1.084	1.003	19.938	29.717	b.d.l	b.d.l	b.d.l	46.379	98.120
Dr5-IPC-03_Traverse2	1.194	0.816	20.560	29.556	b.d.l.	b.d.l.	b.d.l.	46.883	99.008
Dr5-IPC-03_Traverse2	0.216	1.150	19.781	30.670	b.d.l.	0.036	b.d.l.	46.540	98.393
Dr5-IPC-03_Traverse2	0.372	0.906	20.741	30.193	b.d.l.	b.d.l.	b.d.l.	47.133	99.345
Dr5-IPC-03_Traverse2	0.175	0.821	20.674	30.225	b.d.l.	b.d.l.	b.d.l.	46.912	98.806
Dr5-IPC-03_Traverse2	0.934	0.926	20.178	30.208	b.d.l	b.d.l	b.d.l	46.886	99.132
Dr5-IPC-03_Traverse2	0.206	0.857	20.589	29.873	b.d.l.	b.d.l.	0.0149	46.576	98.115
Dr5-IPC-03_Traverse2	0.926	1.251	19.926	29.720	b.d.l	0.035	0.0175	46.440	98.315
Dr5-IPC-03_Traverse2	0.443	0.843	20.386	30.655	b.d.l	b.d.l	b.d.l	47.112	99.438
Dr5-IPC-03_Traverse2 [b]	1.380	1.077	19.736	28.957	b.d.l.	b.d.l.	b.d.l.	45.788	96.937
Dr5-IPC-03_Traverse2	1.491	1.220	19.672	29.385	b.d.l	b.d.l	b.d.l	46.212	97.980
Dr5-IPC-03_Traverse2	0.520	0.930	20.462	29.938	b.d.l	b.d.l	0.0304	46.717	98.598
Dr5-IPC-03_Traverse2	0.603	0.999	20.523	29.425	0.025	0.025	b.d.l.	46.502	98.076
Dr5-IPC-03_Traverse2	0.825	1.226	20.141	29.214	b.d.l.	b.d.l.	b.d.l	46.185	97.590
Dr5-IPC-03_Traverse2	0.194	1.173	20.447	29.919	b.d.l	b.d.l	b.d.l.	46.654	98.386
Dr5-IPC-03_Traverse2	1.354	1.309	19.928	29.616	b.d.l.	b.d.l.	b.d.l.	46.644	98.851
Dr5-IPC-03_Traverse2	1.735	1.076	19.698	29.663	b.d.l.	b.d.l.	b.d.l.	46.518	98.690
Dr5-IPC-03_Traverse2	0.477	1.197	20.206	29.896	b.d.l.	b.d.l.	b.d.l.	46.561	98.338
Dr5-IPC-03_Traverse2	0.334	0.758	20.675	30.115	b.d.l.	b.d.l.	0.0292	46.868	98.779
Dr5-IPC-03_Traverse2	0.798	1.115	19.912	30.051	b.d.l	b.d.l	b.d.l.	46.507	98.383
Dr5-IPC-03_Traverse2	0.997	1.125	20.356	29.538	b.d.l.	b.d.l.	0.0354	46.698	98.749
Dr5-IPC-03_Traverse2	1.316	1.222	19.681	29.047	b.d.l	b.d.l	b.d.l.	45.851	97.117
Dr5-IPC-03_Traverse2	0.555	1.242	19.863	30.109	b.d.l	b.d.l	b.d.l.	46.429	98.198
Dr5-IPC-03_Traverse2	0.163	0.878	20.255	30.406	b.d.l.	b.d.l.	0.0446	46.599	98.346
Dr5-IPC-03_Traverse2	0.892	1.100	20.175	29.512	b.d.l	b.d.l	b.d.l.	46.419	98.098
Dr5-IPC-03_Traverse2	1.130	1.307	19.915	29.161	b.d.l	b.d.l	b.d.l.	46.135	97.649

Dr5-IPC-03_Traverse2	1.102	1.127	20.204	29.479	b.d.l.	b.d.l.	b.d.l.	46.570	98.482
Dr5-IPC-03_Traverse2	0.418	1.353	20.064	30.161	b.d.l	b.d.l	b.d.l	46.674	98.670
Dr5-IPC-03_Traverse2	0.284	0.852	20.717	29.698	b.d.l.	b.d.l.	b.d.l.	46.631	98.181
Dr5-IPC-03_Traverse2	1.310	1.317	19.826	29.452	b.d.l	b.d.l	b.d.l	46.381	98.285
Dr5-IPC-03_Traverse2	1.105	1.225	20.330	29.707	b.d.l	b.d.l	b.d.l	46.949	99.316
Dr5-IPC-03_Traverse2	1.320	1.122	19.729	29.745	b.d.l.	b.d.l.	0.0227	46.378	98.317
Dr5-IPC-03_Traverse2 [b]	1.122	0.639	13.456	19.442	0.509	b.d.l	b.d.l	31.251	66.418
Dr5-IPC-03_Traverse2	0.405	0.915	20.385	29.833	b.d.l	b.d.l.	b.d.l.	46.488	98.027
Dr5-IPC-03_Traverse2	0.264	0.884	20.620	30.072	b.d.l.	b.d.l	b.d.l	46.826	98.665
Dr5-IPC-03_Traverse2	0.634	1.203	20.275	29.815	b.d.l	b.d.l	b.d.l	46.672	98.599
Dr5-IPC-03_Traverse2	0.630	1.407	20.372	29.877	b.d.l	b.d.l.	b.d.l.	46.951	99.237
Dr5-IPC-03_Traverse2	1.236	1.186	19.753	29.506	b.d.l.	b.d.l	b.d.l	46.218	97.898
Dr5-IPC-03_Traverse2	0.778	0.868	20.420	29.739	b.d.l	b.d.l	b.d.l.	46.652	98.457
Dr5-IPC-03_Traverse2	1.238	1.231	20.031	29.031	b.d.l.	b.d.l.	b.d.l	46.177	97.708
Dr5-IPC-03_Traverse2	0.128	0.869	20.807	29.939	b.d.l	b.d.l.	b.d.l	46.833	98.575
Dr5-IPC-03_Traverse2	0.842	1.034	20.331	29.515	b.d.l	0.029	b.d.l.	46.542	98.293
Dr5-IPC-03_Traverse2	0.918	1.096	19.677	29.613	b.d.l.	0.021	b.d.l.	45.984	97.309
Dr5-IPC-03_Traverse2	1.234	1.129	19.936	29.527	b.d.l	b.d.l.	0.0128	46.391	98.229
Dr5-IPC-03_Traverse2	2.115	0.977	19.601	29.775	b.d.l.	b.d.l.	b.d.l.	46.671	99.138
Dr5-IPC-03_Traverse2	0.419	0.950	20.485	29.992	b.d.l	0.025	0.0141	46.761	98.646
Dr5-IPC-03_Traverse2	1.174	1.152	19.704	29.680	b.d.l	b.d.l	b.d.l	46.242	97.952
Dr5-IPC-03_Traverse2	0.615	0.973	20.622	29.746	b.d.l.	b.d.l.	b.d.l.	46.843	98.799
Dr5-IPC-03_Traverse2	1.019	0.989	20.021	29.784	b.d.l	b.d.l	b.d.l	46.474	98.287
Dr5-IPC-03_Traverse2	0.962	1.023	20.150	29.942	b.d.l	b.d.l	b.d.l	46.726	98.804
Dr5-IPC-03_Traverse2	0.427	1.074	20.165	30.391	b.d.l.	b.d.l.	b.d.l.	46.797	98.854
Dr5-IPC-03_Traverse2	0.590	0.956	20.191	30.130	0.020	b.d.l.	0.1385	46.580	98.606
Dr5-IPC-03_Traverse2 [b]	0.374	1.026	20.147	29.363	0.019	0.024	0.0433	45.910	96.907
Dr5-IPC-03_Traverse2	1.629	1.217	19.286	29.414	b.d.l.	0.021	0.0171	45.902	97.487
Dr5-IPC-03_Traverse2	0.437	1.148	20.402	29.474	b.d.l.	b.d.l.	b.d.l.	46.389	97.851

Dr5-IPC-03_Traverse2 [b]	1.256	1.047	19.640	29.034	b.d.l.	b.d.l.	b.d.l.	45.650	96.627
Dr5-IPC-03_Traverse2	0.501	1.052	20.758	29.582	b.d.l	b.d.l	b.d.l	46.841	98.734
Dr5-IPC-03_Traverse2	0.206	0.801	20.554	30.476	b.d.l.	b.d.l.	b.d.l.	46.984	99.021
Dr5-IPC-03_Traverse2 [b]	0.159	0.810	19.482	30.461	b.d.l	b.d.l	b.d.l	45.778	96.690
Dr5-IPC-03_Traverse2	0.421	0.882	20.548	29.106	b.d.l.	b.d.l.	b.d.l.	46.084	97.041
Dr5-IPC-03_Traverse2 [b]	1.018	1.046	19.640	28.729	b.d.l	b.d.l	0.0256	45.250	95.708
Dr5-IPC-03_Traverse2	1.563	1.323	19.659	29.275	b.d.l	b.d.l	0.0478	46.193	98.060
Dr5-IPC-03_Traverse2	0.338	0.984	20.887	29.821	b.d.l.	b.d.l.	0.0221	47.017	99.070
Dr5-IPC-03_Traverse2	1.275	1.193	19.744	29.327	b.d.l	b.d.l.	0.0143	46.089	97.643
Dr5-IPC-03_Traverse2	1.322	1.121	19.822	29.685	b.d.l.	0.064	b.d.l	46.492	98.507
Dr5-IPC-03_Traverse2	0.116	0.777	20.219	30.437	b.d.l	b.d.l	b.d.l.	46.517	98.066
Dr5-IPC-03_Traverse2	0.341	1.150	20.545	30.406	b.d.l.	b.d.l.	b.d.l	47.218	99.660
Dr5-IPC-03_Traverse2	0.432	0.794	20.383	30.163	b.d.l.	b.d.l	b.d.l.	46.686	98.457
Dr5-IPC-03_Traverse2	0.190	1.094	20.518	29.464	b.d.l.	b.d.l.	b.d.l	46.323	97.588
Dr5-IPC-03_Traverse2 [b]	1.470	1.395	19.485	28.737	0.036	0.047	b.d.l	45.642	96.810
Dr5-IPC-03_Traverse2	1.580	1.375	19.646	28.968	b.d.l	b.d.l	b.d.l.	46.007	97.576
Dr5-IPC-03_Traverse2	0.758	1.308	20.094	29.494	b.d.l.	b.d.l.	b.d.l	46.364	98.019
Dr5-IPC-03_Traverse2	1.840	1.005	19.331	29.382	b.d.l	b.d.l	b.d.l	45.917	97.474
Dr5-IPC-03_Traverse2	2.420	1.062	19.363	29.485	b.d.l.	b.d.l.	b.d.l.	46.423	98.752
Dr5-IPC-03_Traverse2	0.355	0.965	20.203	29.939	b.d.l	0.038	b.d.l.	46.399	97.897
Dr5-IPC-03_Traverse2	0.527	0.956	20.569	29.192	b.d.l	b.d.l	0.0134	46.278	97.535
Dr5-IPC-03_Traverse2 [b]	1.756	1.117	19.433	28.480	b.d.l.	b.d.l.	b.d.l	45.339	96.124
Dr5-IPC-03_Traverse2 [b]	0.687	1.059	19.800	28.958	b.d.l.	b.d.l	b.d.l	45.424	95.928
Dr5-IPC-03_Traverse2	1.249	0.973	20.234	30.050	b.d.l	b.d.l.	b.d.l.	47.046	99.553
Dr5-IPC-03_Traverse2 [b]	0.809	1.359	19.456	29.208	b.d.l.	b.d.l	b.d.l	45.506	96.339
Dr5-IPC-03_Traverse2	3.117	1.004	18.663	29.618	b.d.l	b.d.l	b.d.l	46.155	98.557
Dr5-IPC-03_Traverse2	0.163	1.060	20.253	30.085	b.d.l.	b.d.l.	b.d.l.	46.482	98.042
Dr5-IPC-03_Traverse2	0.502	1.308	20.368	29.710	b.d.l	b.d.l	0.0277	46.661	98.576
Dr5-IPC-03_Traverse2	0.772	1.552	19.994	29.303	b.d.l	b.d.l	b.d.l.	46.265	97.885

Dr5-IPC-03_Traverse2	0.874	1.292	20.265	29.391	b.d.l.	b.d.l.	0.0202	46.520	98.362
Dr5-IPC-03_Traverse2 [b]	0.568	1.165	19.935	29.189	b.d.l	0.030	b.d.l.	45.767	96.655
Dr5-IPC-03_Traverse2	1.582	1.120	19.610	29.443	b.d.l.	b.d.l.	b.d.l	46.182	97.936
Dr5-IPC-03_Traverse2	0.613	1.231	20.179	29.613	b.d.l	b.d.l	0.0182	46.403	98.057
Dr5-IPC-03_Traverse2	2.861	0.944	19.189	29.332	b.d.l.	b.d.l.	0.0200	46.326	98.709
Dr5-IPC-03_Traverse2 [b]	1.598	1.459	19.144	28.996	b.d.l	b.d.l	b.d.l.	45.543	96.740
Dr5-IPC-03_Traverse2	2.357	1.096	19.290	28.809	b.d.l	b.d.l	0.0212	45.785	97.358
Dr5-IPC-03_Traverse2	1.704	0.825	19.753	29.573	b.d.l.	b.d.l.	b.d.l.	46.333	98.188
Dr5-IPC-03_Traverse2 [b]	0.505	0.359	11.148	11.558	0.403	0.056	0.0159	21.978	46.023
Dr5-IPC-03_Traverse2 [b]	2.004	1.051	18.829	28.485	0.028	b.d.l	b.d.l.	44.807	95.205
Dr5-IPC-03_Traverse2	1.499	1.067	19.833	29.290	b.d.l	b.d.l.	b.d.l	46.223	97.913
Dr5-IPC-03_Traverse2	3.317	1.024	18.541	29.095	b.d.l.	b.d.l	0.0133	45.739	97.730
Dr5-IPC-03_Traverse2	2.291	1.140	19.233	29.658	b.d.l	b.d.l.	b.d.l.	46.387	98.708
Dr5-IPC-03_Traverse2	1.120	1.147	20.258	29.400	b.d.l.	b.d.l.	b.d.l	46.591	98.515
Dr5-IPC-03_Traverse2	0.170	0.931	20.247	30.362	b.d.l	0.028	0.0578	46.605	98.400
Dr5-IPC-03_Traverse2	0.098	0.730	20.364	30.238	b.d.l	b.d.l	b.d.l.	46.480	97.910
Dr5-IPC-03_Traverse2	1.130	1.097	20.205	29.507	b.d.l.	b.d.l.	b.d.l	46.592	98.530
Dr5-IPC-03_Traverse2	0.112	0.768	20.752	30.193	b.d.l	b.d.l	b.d.l.	46.900	98.726
Dr5-IPC-03_Traverse2	0.683	1.441	19.908	29.607	b.d.l.	b.d.l.	b.d.l	46.285	97.923
Dr5-IPC-03_Traverse2	1.209	1.018	20.262	29.239	b.d.l	b.d.l	b.d.l.	46.444	98.173
Dr5-IPC-03_Traverse2	0.145	1.183	20.449	30.443	b.d.l.	b.d.l	b.d.l	47.043	99.263
Dr5-IPC-03_Traverse2	1.132	0.631	19.848	30.054	b.d.l	b.d.l.	b.d.l.	46.343	98.007
Dr5-IPC-03_Traverse2	0.136	0.811	20.229	30.192	b.d.l	b.d.l.	b.d.l	46.369	97.737
Dr5-IPC-03_Traverse2	0.140	0.764	20.616	29.968	b.d.l.	b.d.l	0.0141	46.582	98.084
Dr5-IPC-03_Traverse2	1.272	1.168	20.078	29.059	b.d.l.	b.d.l.	b.d.l.	46.233	97.810
Dr5-IPC-03_Traverse2	0.290	1.005	20.572	30.232	b.d.l	b.d.l	b.d.l	46.991	99.090
Dr5-IPC-03_Traverse2	1.568	1.165	19.568	29.657	b.d.l.	b.d.l.	b.d.l.	46.325	98.283
Dr5-IPC-03_Traverse2	0.912	1.185	20.081	29.497	b.d.l	b.d.l	b.d.l	46.370	98.044
Dr5-IPC-03_Traverse2	0.140	0.954	20.766	30.163	b.d.l.	0.057	b.d.l.	47.065	99.146

Dr5-IPC-03_Traverse2	1.530	1.028	19.792	29.505	b.d.l		b.d.l	46.342	98.196
Dr5-IPC-03_Traverse2	0.677	1.309	20.210	30.080	b.d.l	b.d.l.	0.0165	46.892	99.184
Dr5-IPC-03_Traverse2	0.146	0.842	20.860	29.930	b.d.l.	b.d.l.	b.d.l.	46.877	98.654
Dr5-IPC-03_Traverse2	1.017	1.115	20.436	29.139	b.d.l	0.030	b.d.l.	46.520	98.257
Dr5-IPC-03_Traverse2	1.595	1.177	19.222	29.708	b.d.l.	b.d.l.	0.0190	46.001	97.722
Dr5-IPC-03_Traverse2	0.707	1.263	20.108	29.820	b.d.l	b.d.l	b.d.l.	46.576	98.474
Dr5-IPC-03_Traverse2	0.776	1.385	19.867	29.719	b.d.l	b.d.l	b.d.l	46.352	98.099
Dr5-IPC-03_Traverse2*	0.285	0.840	20.201	29.544	b.d.l.	b.d.l.	b.d.l	45.940	96.809
Dr5-IPC-03_Traverse2	0.626	1.584	19.745	30.451	b.d.l	b.d.l	b.d.l.	46.824	99.230
Dr5-IPC-03_Traverse2	0.570	0.794	20.103	30.673	b.d.l.	b.d.l.	b.d.l	46.864	99.004
Dr5-IPC-03_Traverse2	1.606	1.551	19.728	29.234	b.d.l	0.028	b.d.l.	46.450	98.597
Dr5-IPC-03_Traverse2	2.987	1.090	18.097	29.627	b.d.l.	b.d.l.	0.0211	45.506	97.328
Dr5-IPC-03_Traverse2	1.015	1.217	19.995	29.049	b.d.l.	b.d.l.	b.d.l.	46.008	97.284
Dr5-IPC-03_Traverse2 [b]	1.158	1.016	20.072	28.817	b.d.l.	b.d.l.	b.d.l.	45.887	96.985
Dr5-IPC-03_Traverse2	1.362	1.107	19.792	29.929	b.d.l.	0.037	0.0159	46.637	98.879
Dr5-IPC-03_Traverse2	0.922	1.530	20.008	29.662	b.d.l	b.d.l	b.d.l.	46.640	98.761
Dr5-IPC-03_Traverse2	0.545	1.364	20.287	29.535	b.d.l.	b.d.l.	b.d.l	46.511	98.241
Dr5-IPC-03_Traverse2	0.830	1.051	20.035	29.435	b.d.l	b.d.l	b.d.l	46.138	97.490
Dr5-IPC-03_Traverse2	4.010	0.791	18.525	29.044	b.d.l.	b.d.l.	b.d.l.	45.969	98.338
Dr5-IPC-03_Traverse2	0.827	1.089	20.227	29.230	b.d.l	b.d.l	b.d.l	46.209	97.583
Dr5-IPC-03_Traverse2	0.354	0.798	20.622	30.477	b.d.l	b.d.l	0.0160	47.140	99.407
Dr5-IPC-03_Traverse2	0.785	1.325	20.247	29.527	b.d.l.	b.d.l.	b.d.l.	46.584	98.467
Dr5-IPC-03_Traverse2 [b]	1.130	0.829	18.927	27.070	0.066	b.d.l	b.d.l	43.146	91.169
Dr5-IPC-03_Traverse2	1.537	1.476	19.816	29.378	b.d.l	b.d.l.	b.d.l	46.552	98.760
Dr5-IPC-03_Traverse2	1.961	1.096	19.474	29.439	b.d.l.	b.d.l	b.d.l.	46.249	98.218
Dr5-IPC-03_Traverse2	0.873	0.927	19.816	30.357	b.d.l	b.d.l.	b.d.l	46.572	98.546
Dr5-IPC-03_Traverse2	0.561	1.319	20.217	30.166	b.d.l.	b.d.l.	b.d.l	46.912	99.175
Dr5-IPC-03_Traverse2	0.586	0.971	20.587	29.140	b.d.l	b.d.l.	b.d.l	46.310	97.594
Dr5-IPC-03_Traverse2	0.964	1.411	20.195	29.428	b.d.l	b.d.l.	b.d.l.	46.612	98.609

Dr5-IPC-03_Traverse2 [b]	1.437	1.394	19.416	29.002	b.d.l.	b.d.l.	b.d.l	45.707	96.956
Dr5-IPC-03_Traverse2	1.611	1.080	19.487	29.683	b.d.l	b.d.l.	b.d.l	46.231	98.092
Dr5-IPC-03_Traverse2	1.286	1.353	20.008	29.500	b.d.l.	b.d.l.	b.d.l.	46.626	98.774
Dr5-IPC-03_Traverse2	1.004	1.579	20.141	28.770	b.d.l	0.029	b.d.l	46.186	97.708
Dr5-IPC-03_Traverse2	1.435	1.416	20.006	29.577	b.d.l.	b.d.l	b.d.l.	46.815	99.249
Dr5-IPC-03_Traverse2	1.384	1.475	20.004	29.312	b.d.l	b.d.l.	b.d.l	46.610	98.785
Dr5-IPC-03_Traverse2	1.002	1.303	20.147	29.749	b.d.l	b.d.l	b.d.l	46.768	98.969
Dr5-IPC-03_Traverse2	1.042	1.402	20.024	29.705	b.d.l.	b.d.l.	b.d.l.	46.685	98.858
Dr5-IPC-03_Traverse2	1.639	1.197	19.632	29.212	b.d.l	b.d.l	b.d.l	46.109	97.790
Dr5-IPC-03_Traverse2	2.124	1.329	19.197	29.110	b.d.l.	b.d.l	b.d.l.	45.932	97.690
Dr5-IPC-03_Traverse2	0.648	1.079	20.180	29.322	b.d.l	b.d.l.	b.d.l	46.113	97.342
Dr5-IPC-03_Traverse2	1.470	1.418	19.710	28.708	b.d.l.	b.d.l	b.d.l.	45.833	97.139
Dr5-IPC-03_Traverse2	1.281	1.299	19.969	29.467	b.d.l.	b.d.l.	b.d.l.	46.521	98.538
Dr5-IPC-03_Traverse2	0.447	0.963	20.197	30.493	b.d.l.	b.d.l	b.d.l.	46.856	98.955
Dr5-IPC-04_Traverse1 [b]	0.882	0.829	0.082	29.930	b.d.l.	b.d.l.	b.d.l.	24.632	56.354
Dr5-IPC-04_Traverse1	0.549	0.914	20.719	30.379	b.d.l	b.d.l.	0.0243	47.355	99.940
Dr5-IPC-04_Traverse1	0.726	0.817	20.493	30.120	b.d.l.	b.d.l.	b.d.l.	46.967	99.123
Dr5-IPC-04_Traverse1	0.574	0.809	20.519	29.841	b.d.l.	b.d.l.	b.d.l.	46.678	98.421
Dr5-IPC-04_Traverse1	0.342	0.985	20.148	30.024	b.d.l.	b.d.l	0.0170	46.374	97.889
Dr5-IPC-04_Traverse1	0.592	0.925	20.127	29.735	b.d.l.	b.d.l.	0.0219	46.238	97.639
Dr5-IPC-04_Traverse1	0.290	0.937	20.337	30.149	b.d.l.	b.d.l.	0.0268	46.611	98.349
Dr5-IPC-04_Traverse1 [b]	0.547	0.766	20.259	29.331	b.d.l.	b.d.l.	b.d.l.	45.950	96.853
Dr5-IPC-04_Traverse1	0.354	1.035	20.194	30.060	b.d.l.	b.d.l.	0.0308	46.484	98.157
Dr5-IPC-04_Traverse1	0.705	0.871	19.821	29.730	0.021	b.d.l	0.0326	45.938	97.119
Dr5-IPC-04_Traverse1	0.431	0.886	19.936	29.958	b.d.l.	b.d.l.	b.d.l.	46.094	97.305
Dr5-IPC-04_Traverse1	0.350	1.066	19.818	29.989	b.d.l.	b.d.l.	b.d.l	46.051	97.274
Dr5-IPC-04_Traverse1	0.481	0.900	20.764	29.596	b.d.l.	b.d.l.	b.d.l.	46.752	98.492
Dr5-IPC-04_Traverse1 [b]	0.625	0.788	20.041	29.573	b.d.l.	b.d.l.	b.d.l.	45.963	96.989
Dr5-IPC-04_Traverse1	0.533	0.928	20.433	29.871	b.d.l.	b.d.l.	b.d.l.	46.656	98.420

Dr5-IPC-04_Traverse1	0.273	0.846	20.664	30.013	b.d.l.	0.044	0.0164	46.833	98.690
Dr5-IPC-04_Traverse1 [b]	0.510	0.976	20.130	29.081	b.d.l	b.d.l	0.0254	45.708	96.431
Dr5-IPC-04_Traverse1	0.814	0.976	20.025	29.689	b.d.l.	b.d.l.	b.d.l.	46.271	97.775
Dr5-IPC-04_Traverse1	0.546	0.868	20.855	29.916	b.d.l	0.038	b.d.l	47.150	99.373
Dr5-IPC-04_Traverse1 [b]	1.055	0.807	19.949	29.241	b.d.l.	b.d.l	b.d.l.	45.878	96.929
Dr5-IPC-04_Traverse1	0.564	0.802	20.568	29.969	b.d.l	b.d.l.	0.0173	46.811	98.731
Dr5-IPC-04_Traverse1 [b]	0.897	0.894	19.848	28.983	b.d.l	0.037	0.0181	45.538	96.215
Dr5-IPC-04_Traverse1 [b]	0.250	0.837	19.970	29.816	b.d.l.	b.d.l.	0.0259	45.864	96.763
Dr5-IPC-04_Traverse1	0.730	0.907	20.224	29.653	b.d.l	b.d.l	0.0178	46.355	97.887
Dr5-IPC-04_Traverse1	0.257	0.877	20.479	30.540	b.d.l.	b.d.l.	0.0293	47.014	99.195
Dr5-IPC-04_Traverse1 [b]	0.645	0.741	18.076	29.688	b.d.l	b.d.l	b.d.l.	43.891	93.040
Dr5-IPC-04_Traverse1	0.347	0.988	20.199	29.813	b.d.l.	b.d.l.	b.d.l	46.278	97.625
Dr5-IPC-04_Traverse1	0.256	0.937	20.470	30.312	b.d.l.	0.038	b.d.l.	46.906	98.919
Dr5-IPC-04_Traverse1	0.656	0.861	20.216	30.369	b.d.l.	b.d.l	0.0367	46.823	98.961
Dr5-IPC-04_Traverse1	0.368	0.856	20.477	30.011	b.d.l	b.d.l.	0.0224	46.656	98.389
Dr5-IPC-04_Traverse1	0.413	0.887	20.552	29.820	b.d.l.	0.055	b.d.l	46.687	98.415
Dr5-IPC-04_Traverse1 [b]	0.389	0.418	12.992	17.836	0.263	0.161	b.d.l.	28.907	60.966
Dr5-IPC-04_Traverse1	0.380	0.880	20.219	29.944	b.d.l	0.037	b.d.l	46.383	97.844
Dr5-IPC-04_Traverse1	0.176	0.862	20.084	30.356	b.d.l.	b.d.l.	0.0162	46.388	97.883
Dr5-IPC-04_Traverse1 [b]	0.630	0.857	19.888	29.406	b.d.l	b.d.l	0.0337	45.693	96.508
Dr5-IPC-04_Traverse1	0.478	0.817	20.491	29.954	b.d.l.	b.d.l.	b.d.l	46.683	98.423
Dr5-IPC-04_Traverse1	0.498	0.906	20.235	29.798	b.d.l	b.d.l.	0.0189	46.338	97.793
Dr5-IPC-04_Traverse1	0.329	0.859	20.745	29.586	b.d.l	b.d.l	0.0191	46.595	98.132
Dr5-IPC-04_Traverse1	0.431	0.906	20.642	29.831	b.d.l.	b.d.l.	b.d.l	46.776	98.585
Dr5-IPC-04_Traverse1	0.393	0.939	20.207	29.681	b.d.l	b.d.l	0.0236	46.168	97.411
Dr5-IPC-04_Traverse1	0.392	0.902	20.536	29.739	b.d.l.	b.d.l.	b.d.l	46.562	98.131
Dr5-IPC-04_Traverse1	0.449	0.945	20.552	29.956	b.d.l	0.031	b.d.l.	46.834	98.767
Dr5-IPC-04_Traverse1	0.351	0.977	20.518	29.935	b.d.l.	b.d.l	0.0178	46.708	98.506
Dr5-IPC-04_Traverse1	0.405	0.832	20.475	29.980	b.d.l.	0.046	b.d.l	46.683	98.421

Dr5-IPC-04_Traverse1	0.408	0.841	20.481	29.826	b.d.l.	b.d.l	0.0180	46.533	98.107
Dr5-IPC-04_Traverse1	1.242	0.887	19.531	30.354	b.d.l	b.d.l	0.0341	46.441	98.489
Dr5-IPC-04_Traverse1	0.520	0.891	20.288	29.863	b.d.l.	b.d.l.	b.d.l	46.461	98.022
Dr5-IPC-04_Traverse1	0.408	0.946	19.992	30.337	b.d.l	b.d.l	0.0226	46.463	98.169
Dr5-IPC-04_Traverse1	0.502	0.892	20.357	29.905	b.d.l.	b.d.l.	b.d.l	46.558	98.214
Dr5-IPC-04_Traverse1	0.442	0.850	20.461	30.027	b.d.l	b.d.l	0.0196	46.694	98.494
Dr5-IPC-04_Traverse1	0.261	0.976	20.124	29.923	b.d.l	b.d.l	b.d.l	46.223	97.507
Dr5-IPC-04_Traverse1	0.270	0.882	20.052	30.411	b.d.l.	0.033	b.d.l	46.498	98.145
Dr5-IPC-04_Traverse1	0.373	0.976	20.078	30.289	b.d.l	b.d.l	b.d.l	46.528	98.244
Dr5-IPC-04_Traverse1	0.481	0.788	20.281	29.504	b.d.l.	b.d.l	0.0140	46.076	97.144
Dr5-IPC-04_Traverse1 [b]	0.338	0.829	19.950	29.849	b.d.l	0.042	b.d.l	45.961	96.969
Dr5-IPC-04_Traverse1	0.557	1.020	19.482	30.167	b.d.l.	b.d.l	0.0153	45.914	97.156
Dr5-IPC-04_Traverse1	0.454	0.898	20.535	30.173	b.d.l.	0.044	b.d.l	46.969	99.073
Dr5-IPC-04_Traverse1	0.321	0.883	20.210	29.937	b.d.l.	b.d.l	0.0175	46.297	97.665
Dr5-IPC-04_Traverse1	0.642	0.842	20.543	30.087	b.d.l	b.d.l.	b.d.l.	46.959	99.073
Dr5-IPC-04_Traverse1	0.501	0.918	20.376	29.510	b.d.l	b.d.l	b.d.l	46.285	97.589
Dr5-IPC-04_Traverse1	0.458	0.833	20.262	29.562	b.d.l	b.d.l.	b.d.l	46.122	97.238
Dr5-IPC-04_Traverse1	0.160	0.615	20.328	30.891	b.d.l	b.d.l	b.d.l.	46.919	98.912
Dr5-IPC-04_Traverse1 [b]	0.401	0.830	19.545	28.558	0.036	b.d.l	b.d.l	44.530	93.900
Dr5-IPC-04_Traverse1	0.780	0.833	20.372	29.893	b.d.l	b.d.l	b.d.l	46.699	98.577
Dr5-IPC-04_Traverse1	0.511	0.817	20.104	29.627	b.d.l.	b.d.l	b.d.l	46.023	97.082
Dr5-IPC-04_Traverse1	0.496	0.768	20.423	30.042	b.d.l	b.d.l	b.d.l	46.658	98.388
Dr5-IPC-04_Traverse1 [b]	0.321	1.015	19.871	29.702	b.d.l.	0.033	0.0320	45.839	96.812
Dr5-IPC-04_Traverse1	0.339	0.803	19.798	30.645	b.d.l	b.d.l.	0.0359	46.354	97.975
Dr5-IPC-04_Traverse1	0.369	0.860	20.529	30.016	b.d.l	b.d.l	b.d.l	46.733	98.507
Dr5-IPC-04_Traverse1	0.371	0.897	20.499	30.161	b.d.l.	b.d.l	b.d.l	46.838	98.766
Dr5-IPC-04_Traverse1	0.385	0.780	20.314	29.953	b.d.l	b.d.l	0.0372	46.388	97.858
Dr5-IPC-04_Traverse1	0.500	0.885	20.455	30.183	b.d.l	b.d.l	0.0141	46.871	98.909
Dr5-IPC-04_Traverse1	0.224	0.905	20.302	30.567	b.d.l	0.032	b.d.l	46.879	98.909

Dr5-IPC-04_Traverse1 [b]	0.598	0.798	19.875	29.437	0.021	b.d.l	0.0194	45.664	96.411
Dr5-IPC-04_Traverse1 [b]	0.755	0.724	18.830	27.398	0.051	0.062	0.0172	43.031	90.868
Dr5-IPC-04_Traverse1	0.402	0.857	20.540	29.916	b.d.l	b.d.l	b.d.l.	46.684	98.399
Dr5-IPC-04_Traverse1	0.714	0.859	20.055	29.490	b.d.l.	b.d.l.	0.3262	45.833	97.277
Dr5-IPC-04_Traverse1	0.390	0.827	20.098	29.752	b.d.l	b.d.l	b.d.l.	46.047	97.115
Dr5-IPC-04_Traverse1	0.217	0.955	20.155	30.178	b.d.l.	b.d.l.	0.0282	46.402	97.935
Dr5-IPC-04_Traverse1	0.361	0.893	20.335	30.083	b.d.l	b.d.l	b.d.l.	46.589	98.262
Dr5-IPC-04_Traverse1 [b]	0.223	0.852	19.875	30.054	b.d.l	b.d.l	0.0399	45.931	96.975
Dr5-IPC-04_Traverse1	0.326	0.789	20.289	29.803	b.d.l.	b.d.l.	0.0221	46.221	97.451
Dr5-IPC-04_Traverse1	0.393	0.941	20.441	30.200	b.d.l	b.d.l	b.d.l	46.845	98.820
Dr5-IPC-04_Traverse1	0.537	0.796	20.625	29.420	b.d.l.	b.d.l.	b.d.l.	46.434	97.813
Dr5-IPC-04_Traverse1	0.412	0.629	20.350	30.673	b.d.l	b.d.l	b.d.l	46.935	98.999
Dr5-IPC-04_Traverse1	0.420	0.871	20.391	29.736	b.d.l.	b.d.l.	b.d.l.	46.401	97.820
Dr5-IPC-04_Traverse1	0.457	0.819	20.488	29.468	b.d.l.	b.d.l.	0.2384	46.154	97.624
Dr5-IPC-04_Traverse1	0.254	0.868	20.256	30.003	b.d.l.	b.d.l.	0.0148	46.350	97.745
Dr5-IPC-04_Traverse1	0.403	0.898	20.209	29.614	b.d.l.	0.060	b.d.l.	46.154	97.338
Dr5-IPC-04_Traverse1	0.423	0.890	20.314	29.984	b.d.l.	b.d.l.	b.d.l.	46.524	98.135

[b] bad point, not analyzed in the text.

b.d.l.= below detection limit.

n.m. = not measured.